Design, synthesis and biological evaluation of novel tricyclics as dual cholinesterase (ChE) and amyloid aggregation inhibitors with antioxidant properties

by

Gary Tin

A thesis

presented to the University of Waterloo

in fulfillment of the

thesis requirement for the degree of

Master of Science

in

Pharmacy

Waterloo, Ontario, Canada, 2014

Author's declaration

I hereby declare that I am the sole author of this thesis. This is a true copy of the thesis, including any final revision as accepted by my examiners.

I understand that my thesis may be made electronically available to the public.

Abstract

Alzheimer's disease (AD) is a complex neurodegenerative disease affecting the cholinergic region of the brain. Its prevalence is steadily increasing and it is becoming one of the highest costing diseases to modern society. Current drug therapies only provide symptomatic relief and are not a viable option for long-term treatment. Thus, there is a need for more effective disease-modifying therapeutics. Since the discovery of AD, research in the field has led to a number of proposed theories behind the causes of AD including the (i) cholinergic hypothesis (ii) amyloid beta hypothesis and (iii) oxidative stress hypothesis. The major class of drug therapies are cholinesterase inhibitors; however, this "one drug, one target" approach has proved to be ineffective during the later stages of disease progression. Here we examined two novel classes of tricyclics; phenothiazines (**5**, **6**, **7a-l**) and phenoselenazines (**13**, **14**, **15a-l**) to target the cholinesterases (ChE), amyloid aggregation, and oxidative stress pathways of AD. This new design approach is aimed at discovering potential disease-modifying therapeutics with multi-targeting abilities. Chapter 1 encompasses background information pertaining to the role of each hypothesis in AD including the cholinesterase, amyloid and oxidative stress hypothesis. Chapter 2 provides a summary of the design and hypothesis behind the project. Chapter 3 describes the chemistry conducted including the chemical protocols, reaction schemes and mechanisms in synthesizing the target molecules. Chapter 4 reviews the biological evaluation and the SAR analysis of the synthesized compounds. Furthermore, it describes the principles behind the biological assays conducted including cholinesterase inhibition, amyloid aggregation inhibition, antioxidant properties and cell viability in neuroblastoma cell lines. Chapter 5 consists of the molecular modeling results and their application to help rationalize the results in both the cholinesterase and amyloid aggregation SAR data. Chapter 6 reviews all the data acquired and

provides ideas for future directions. Finally chapter 7 provides the full experimental details for synthetic chemistry as well as the analytical data for synthesized compounds and protocols for biological evaluations. The research project conducted identified novel tricyclics as dual cholinesterase inhibitors with multi-target abilities in anti-amyloid aggregation inhibition and antioxidant properties. The most potent AChE inhibitor was **15d (**(4-methoxyphenyl)-10*H*-phenoselenazin-10-ylmethanone; AChE IC_{50} = 4.63 μM), whereas the most potent BuChE inhibitor was **13** (10*H*-phenoselenazine; BuChE IC_{50} = 3.00 μM). Overall the best dual cholinesterase derivative was identified as compound **15j** (2-chloro-10*H*-phenoselenazin-10-yl(4-methoxyphenyl)methanone; AChE IC_{50} = 5.79 μM, BuChE IC_{50} = 4.91 μM). Both PTZ and PSZ derivatives exhibited good antioxidant properties with weak anti-aggregation activity. In conclusion, our studies provide a new class of tricyclics in the design and development of small molecules to target multiple pathways of AD.

Publications

1. Tarek Mohammed, Wesseem Osman, **Gary Tin**, Praveen P.N. Rao. Selective inhibition of human acetylcholinesterase by xanthine derivatives: In vitro inhibition and molecular modeling investigations. *Bioorg. Med. Chem. Lett.* **23**, 4336-4341 (2013).

Conference Presentations:

2. **Gary Tin**, Tarek Mohamed, Praveen Nekkar Rao, Design, Synthesis and Biological Evaluation of Novel Phenothiazines: Dual Cholinesterase (ChE), Amyloid Aggregation Inhibitors with Antioxidant Properties. Canadian Society for Chemistry: Canadian Chemistry Conference and Exhibition (2014).

Acknowledgements

I would like to extend my thanks to the University of Waterloo's School of Pharmacy for supporting the presented work and also to the graduate studies office for their funding of the project and conference expenses.

I also want to thank MITAC's Canada and Cyclica Inc. for allowing me the opportunity to participate in their internship program, which helped me gain exposure to the industry and add to my overall graduate experience.

I would also like to acknowledge Tarek Mohammed and Wessem Osman for their expertise during the project as mentors. I would like to extend my thanks to Nyasha Gondora and Dr. Michael Beazely for providing MTT cell viability assay data. Finally, I would like to acknowledge Katherine Tran for her dedication and hardwork with the project during her time as a lab volunteer in our research group.

Dedication

I would like to dedicate the efforts presented here to my parents, Amos Tin and Quinnie Mok, my aunt, Emily Tin, and my grandma, Wong Wei Ching who have given me their full support throughout my graduate career. I would also like to thanks all my friends and colleagues who helped me on my journey, especially Natalie Wong for her unwavering support. Lastly, I would like to dedicate my work to Dr. Praveen Nekkar for not only giving me this great opportunity, but for helping me obtain work experience through a MITACs internship, and also for supporting me throughout my masters project. Finally, I would also like to extend my appreciation to my committee members, Dr. Michael Beazely and Dr. Gary Dmitrienko for their advice and support over the last 2 years.

Table of contents

List of Figures

Chapter 1

Chapter 2

Chapter 3

List of Tables

Chapter 4

List of schemes

Chapter 3

List of abbreviations

Aβ – Beta amyloid

ACh – Acetylcholine

AChE –Acetylcholinesterase

AChEIs – Acetylcholinesterase inhibitors

AD - Alzheimer's disease

APP – Amyloid precursor protein

Asp – Aspartate

BuChE – Butyrylcholinesterase

ChAT – Cholineacetyltransferase

ChE - Cholinesterase

CNS - Central nervous system

DCM – Dichloromethane

DPA – Diphenylamine

DPPH - 2,2-Diphenyl-1-picrylhydrazyl

EtOAc – Ethylacetate

FDA – Food and Drug Administration

Glu - Glutamate

His – Histidine

HPLC – High performance liquid chromatography

$MgSO_4$ – Magnesium sulfate

mL – Millilitre

mmol – Millimole

MP – Melting point

MS – Mass spectrometry

NFT - Neurofibrillary tangles

NMR – Nuclear magnetic resonance

PAS - Peripheral anionic site

PSZ – Phenoselenazine

PTZ – Phenothiazine

PUFA – Poly unsaturated fatty acid

RBF – Round bottom flask

RM – Reaction mixture

ROS – Reactive oxygen species

SAR – structure activity relationship

Ser – Serine

SD – Standard deviation

ThT – Thioflavin T

TLC – Thin layer chromatography

Trp – Tryptophan

Tyr – Tyrosine

UPW – Ultra pure water

Chapter 1: Introduction

1.1 Background on Alzheimer's Disease

Alzheimer's disease (AD) is a complex neurodegenerative disorder that affects areas of the brain dealing with memory, cognition and function. Over 30 million people worldwide suffer from AD, and that number is expected to increase significantly in the near future.[1] The current drug therapies on the market are palliative and without further intervention, the widespread burden of the disease will only increase with time.[2] There is not yet a cure for AD, thus there remains a necessity to develop drugs that contain disease-modifying properties that may alter the course and slow disease progression.

AD is the most common type of dementia[3]; where dementia is classified as any individual who suffers from either mild or major neurocognitive dysfunction that affects their ability to perform tasks in daily life settings. Dementia is the outcome of damaged neurons, which leads to impaired cognitive function. There are many types of dementia, each with their own unique characteristics and disease hallmarks. In the case of AD, which accounts for over 60% dementia cases, one of the earliest symptoms is the decline in one's memory. Hallmarks of the disease include pathological extracellular plaques and neurofibrillary tangles.[4] More pronounced symptoms that appear later on in the disease include: confusion, sporadic behavior, aggression, disorientation etc. In severe cases the sufferer is unable to perform daily tasks by themselves such as walking, speaking and swallowing, and requires full commitment from caregivers to attend to them. Altogether AD ultimately leads to death.[1]

The prevalence of those inflicted with AD is becoming a staggering problem in developed societies. While most of the other major diseases have seen marked decrease in numbers, AD is the only major disease that has been on the rise. In 2010 there was an estimated 36 million people with dementia and the number is expected to double every 20 years, which is a concern worldwide.[5]

The biggest concern that AD places, besides the disease itself inflicted on the primary patient, is the secondary and tertiary effects it has on caregivers and the economy respectively. On average individuals diagnosed with AD have a life expectancy of around 6 years after the onset of various clinical symptoms.[2] This number will vary based on a number of factors including age, genetics, quality and access to care, etc. AD is especially devastating due to its prolonged length of progression; whereby primary caregivers – most usually family members – are placed with the task of attending to the needs of the patient.[1] Home care is generally preferred as the healthcare costs of hospitalized institutions are enormous. There have been multiple studies on the social and psychological burdens that AD places on caregivers, adding to the overall implications of the disease. Due to the erratic behavioural changes implicated by a typical AD patient, the amount of stress placed on the primary caregiver is immense, especially during the later stages of the disease when symptoms are most severe. Primary caregivers are placed at high risk of developing a multitude of physical and mental disorders from the demanding work of dealing with AD patients.[5]

The other complex aspect of AD is the immense cost – both direct and indirect – it places on the economy. While AD may not be prevalent in third world countries, it ranks among the highest costing diseases in developed societies.[5] In terms of direct cost, an estimated 150 billion dollars will be spent in 2014 in the US on medicare towards AD health care, long-term care and hospice.[1] With the disease prevalence rising at an alarming rate, the impact and burden on the economy will be unbearable. The long-term hospital care required to house patients remains one of the biggest issues moving forward for health care. Aside from hospital care, there is also the cost associated with specialized in-home social workers, since in the case of AD, round-the-clock supervision is vital for high quality care. The indirect costs of AD also accumulate from both the lost productivity of the patient and the caregiver. Especially in the case of in-home care, primary caregivers in the US alone provided an estimated 17.7 billion informal care (unpaid hours) in 2013.[5] These figures, classified as "unpaid caregivers", make up the bulk of the indirect costs lost due to AD.

Various risk factors play important roles in AD pathophysiology. The biggest risk factor is age. Approximately 95% of the patients living with AD are 65 or older, while the other 5% diagnosed with early on-set AD, is due to genetics.[1] About one third of the population aged 85 or older have AD, showing that age is a major driver in AD development. Another important risk factor is the genetic risk which can promote the early on-set familial AD (FAD). Mutations in specific genes cause the early on-set and progression in individuals compared to the regular sporadic AD (SAD).[6] Although FAD only accounts for approximately 1% of all AD cases, the findings from the studies have generated a breadth of knowledge that has been crucial in our understanding of the disease.[7] Autosomal dominant mutations in the genes encoding for either APP, presenilin 1 (PSEN1) or PSEN2 cause the FAD by increasing the mis-processing of APP. The major genetic risk factor is the apolioprotein E (APOE).[8] Humans contain three alleles of APOE; APOE2, APOE3 and APOE4. Carrying the APOE4 could potentially initiate disease progression at a much earlier age than SAD does. The APOE proteins play a role in AD in mediating the clearance of beta amyloid. The protein APOE2 is considered to be neuroprotective, where as APOE3 is considered to be neutral, and APOE4 is considered to be a risk factor as it is least efficient at clearing Aβ. While a large percentage of the population carries the APOE3 allele, the

25% of the population that carries the APOE4 allele bear a much higher risk of developing AD. Approximately 60% of all AD patients carry at least one copy of the APOE4 gene.[1]

With the increasing global population, lifespan and baby-boomers, AD will be of great concern in the very near future. The societal and economic cost of AD will be prohibitively expensive. These factors support the development of novel disease modifying therapeutics to slow or even halt disease progression.

1.2 Cholinergic Hypothesis

The first and oldest hypothesis of AD, states that AD originates due to a deficiency of the cholinergic neurons. The main neurotransmitter implicated in AD disease pathology, acetylcholine (ACh), has been studied extensively for its role in cognitive function.[9] It is known to play an important role in the brain dealing with memory, learning and cognition. The therapeutic rationale behind developing drugs that tackle this issue arose after the discovery of altered ACh levels in AD brains. Results from these studies showed a marked decrease in the synthesis of ACh located in the pre-synaptic region of the brain, nucleus basalis of Meynert.[10] These findings led to the view that the deterioration of memory and cognition is caused by this deficiency of ACh available for cholinergic transmission.[11] The proposed pharmacological mechanism became the subject of focus, dedicating research into the discovery of acetylcholinesterase inhibitors (AChEIs) as one possible form of treatment.[12] This is the most widely accepted hypotheses relating to AD and remains the main target for current AD therapies.

The cholinesterase (ChE) enzymes, acetylcholinesterase (AChE) and butyrylcholinesterase (BuChE) belong to a family of α/β hydrolases that mediate the breakdown of ACh. Both enzymes share a 60% sequence homology, but AChE is the primary enzyme implicated in AD since it is located in neural synapses.[13] Its primary role in normal physiology is to terminate synaptic transmission of ACh, breaking it down into acetate and choline. (**Figure 1.1**) Both enzymes' active site contains the typical catalytic triad consisting of serine, histidine and glutamate (instead of aspartate).[14] A general mechanism of the acetylcholine catalysis is shown below.

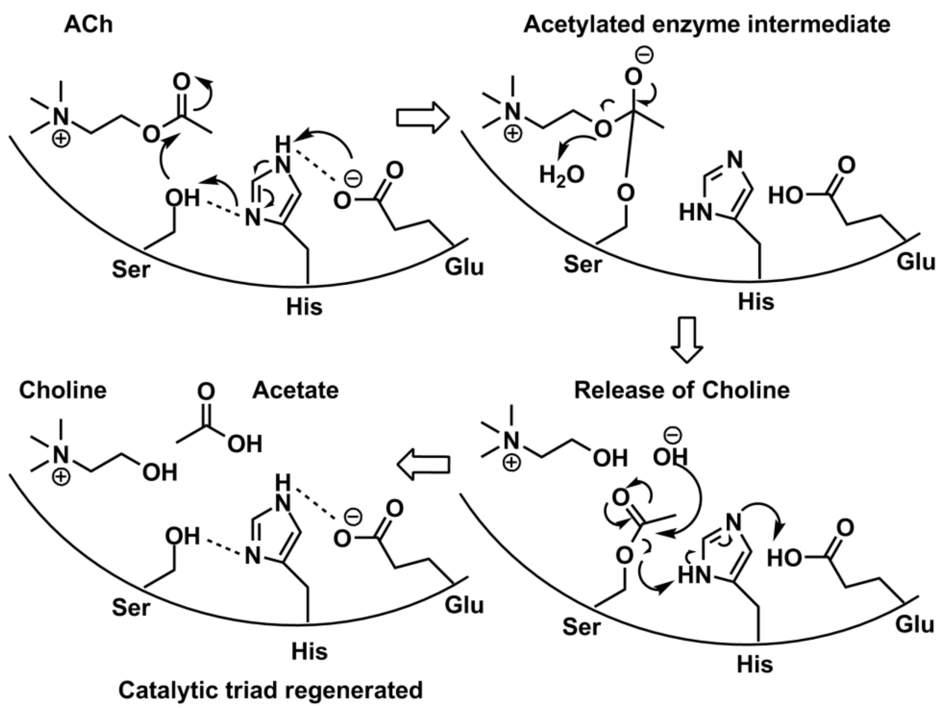

Figure 1.1: Mechanism of AChE hydrolysis by cholinesterases

AChE is recognized as the primary enzyme responsible for the breakdown of ACh. It is located throughout the body at neuromuscular junctions and also in the cholinergic brain synapses. The AChE of interest pertaining to AD is the membrane-bound version found in the CNS that mediate the termination of neural transmission.[15] Its crystal structure has been studied extensively and it is unique in that the active site is located deep within the enzyme in a 20 Å gorge.[16] Numerous residues at the opening of the active site resemble a bottleneck-like shape guiding its natural substrate, ACh downwards. Precise components of the enzyme help increase its specificity, including the key stabilizing Trp86 residue of the hydrophobic pocket; Phe295 and Phe297, forming the acyl pocket that stabilizes the acetyl end of ACh. (**Figure 1.2**) Another interesting region in AChE besides the active site is the peripheral anionic site (PAS) located at the opening comprised of Trp286.[17] Not only does this anionic site serve to help guide substrates into the active site, it has been implicated that it plays a key role in the AChE-mediated Aβ aggregation. The presence of various hydrophobic residues acts as a seeding point for Aβ peptides to amass, causing the formation of a highly toxic AChE-Aβ complex that promotes further aggregation of neurotoxic aggregates.[18]

While AChE is the primary enzyme, BuChE is recognized as the "secondary" cholinesterase in the body. [19] Produced by the liver, this enzyme is mainly present in the plasma. Its main biological function was thought to serve as a backup towards AChE, until it was found to help hydrolyze a number of different substrates including the recreational alkaloid, cocaine.[20] Its clinical significance is now recognized as a potential safeguard to neurotoxic anti-cholinesterase agents by helping the breakdown of these compounds before they are able to reach neuronal junctions.[21] Structurally, BuChE is similar to AChE in that it still has its active site gorge 20 Å deep within the enzyme. The catalytic triad also remains similar with the serine, hisitine and glutamate. The same Trp82 is present as the key stabilizing residue for catalytic activity. (**Figure 1.2**) Major structural differences include the replacement of many of the aromatic residues at the opening with smaller residues, making the entrance to the active site much less restrictive. The acyl pocket is also replaced with smaller residues of Leu286 and Val288 instead of two Phe's, allowing for a lower overall specificity of substrates. Since the opening and active site is replaced with smaller residues, this results in a much larger active site volume, approximately 200 Å^3 larger than AChE.[22]

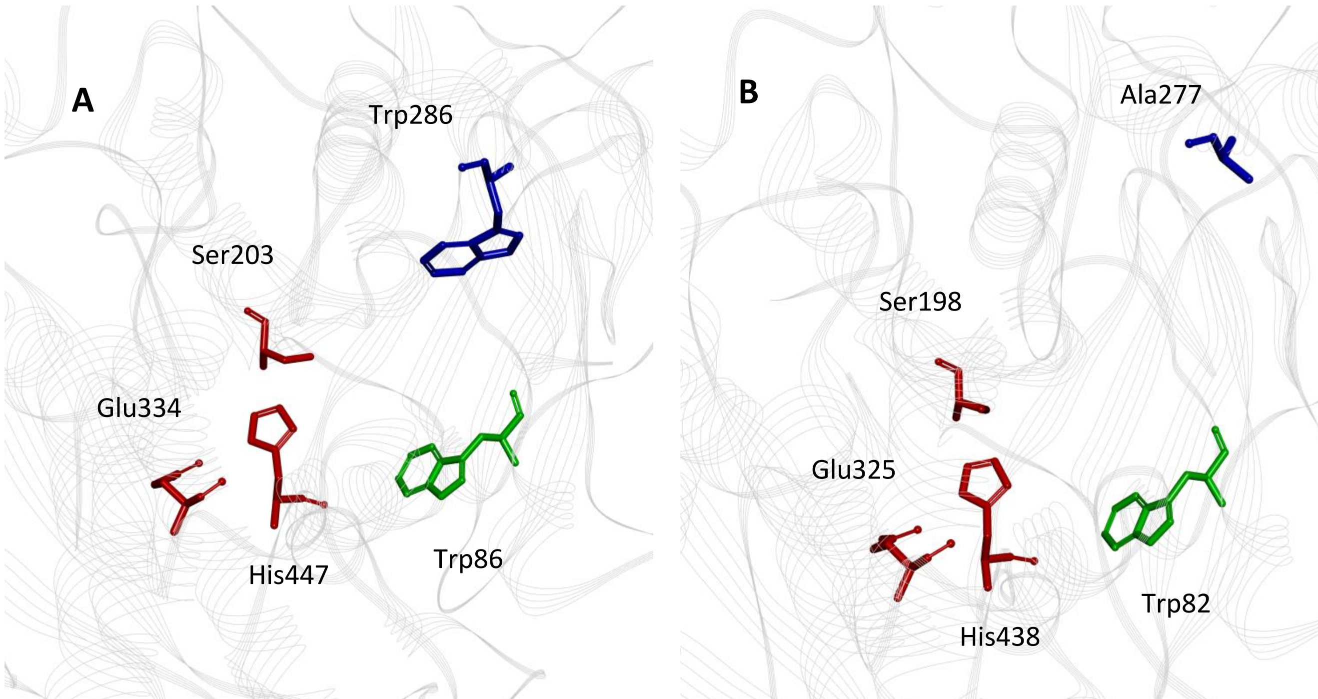

Figure 1.2: Active site details of mammalian AChE (A) and BuChE (B)

The AChEIs were introduced as pharmacotherapy option in AD, as they were able to prevent the hydrolysis of ACh and promote cholingeric transmission to enhance cognition.[23] Current drug therapies with AChEIs offer limited benefit since they do not modify the disease progression, but rather, only slow the onset of symptoms by modulating cholinergic transmission. In advanced stages of AD, when the neurons succumb to the various toxic factors and begin to deteriorate, the use of AChEIs would no longer be viable.[24] There have been multiple studies that show galantamine's (**Figure 1.3**) ability to act as a multi-targeted AChEI.[25] While it is a less potent AChE inhibitior compared to that of donepezil and rivastigmine (**Figure 1.3**), its main attractiveness as a drug appears to be due to the fact that it also acts as an allosteric modulator of nicotinic acetylcholine receptors (nAChR).[26] The interaction with nAChRs have been shown to help modulate cognitive symptoms and neurodenegerative processes.[27] In addition, AChEI's have been shown to induce the release of other neurotransmitters by acting on the nAChRs. In more recent studies, galantamine has also demonstrated to possess the ability to inhibit self-induced aggregation of Aβ-fibrils and potentially help mediate its cytotoxicity.[28] This shows the promising potential of a new generation of compounds that inherit a multi-targeted approach by possessing disease-modifying capabilities.

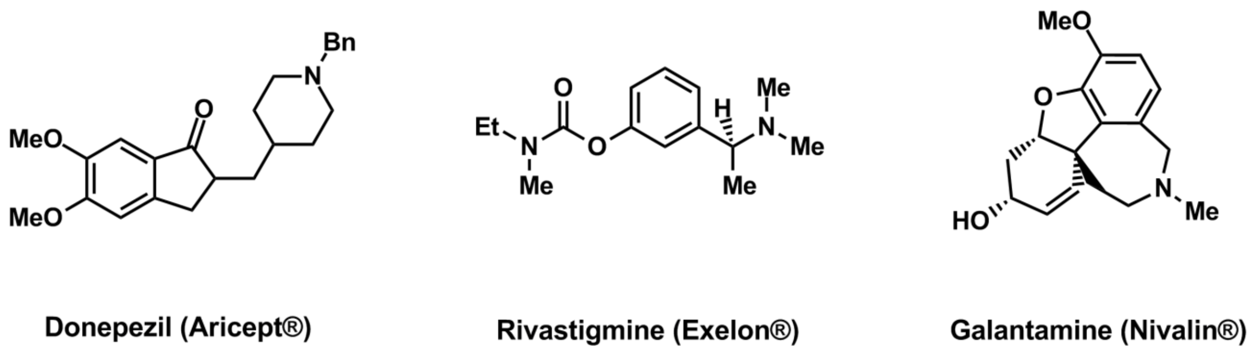

Figure 1.3: Chemical structures of currently marketed cholinesterase inhibitors

1.3 Amyloid Hypothesis

The amyloid hypothesis arose when deposits of extracellular amyloid senile plaques were identified in AD brain samples post-mortem.[29] It was found that these mis-folded protein aggregates were a result of a multitude of cascading events; mis-processing of the amyloid precursor protein (APP) through genetic mutations, shift of APP towards the amyloidogenic pathway (**Figure 1.4**), inherent clearance mechanisms of amyloid beta (Aβ) peptides down-regulated, and elevated levels of aggregates by coordination with various sources.[30] The presence of amyloid plaques in healthy brains, albeit in lower levels, from post-mortem analysis makes it unclear whether the on-set of AD is a direct result of the toxic amyloid aggregates.[31] But studies show that Aβ is implicated as a major hallmark of the disease. Levels of Aβ in AD brains are elevated compared to healthy controls supports this arguement.[32] The Aβ hypothesis was further supported by the discovery and elucidation of 3 genetic mutations on APP, PSEN1 or PSEN2 that cause FAD, and the risk factor of individuals carrying the APOE4 gene.[33] A number of research efforts have been set out to deal with the amyloid hypothesis and various methods have been suggested to maintain normal levels of Aβ required for functioning brains. Currently there are 3 main views for pharmacotherapy; Blocking the enzymes that processes APP into smaller Aβ fragments, blocking the formation and aggregation of Aβ peptides to more toxic oligomeric structures, and supplementing clearance mechanisms of the formed Aβ aggregates to reduce the amyloid load.[34] The oligomers formed are the most toxic form of Aβ aggregates. Oligomers are found to provide Aβ aggregates as a seeding point, are large enough to be able to disrupt cell membranes and neuronal communication through the hindering of synapses, and induce intracellular calcium deregulation causing apoptosis through excitoxicity.[35] There is a generalized view that there exists a certain threshold for which Aβ levels must reach in order for major disease progression to occur, and once that level is reached, the disease itself becomes Aβ independent.[36] The formed oligomers begin the cascade of forming plaques and re-seeding themselves, thus treatment options for the Aβ hypothesis must be introduced before this threshold is reached. It is unclear how early on this threshold is implicated and further clinical studies needs to be done. In the ideal situation Aβ therapeutics would be given to cohorts of individuals with and without AD to examine the complex relationship of the disease process to fully elucidate the mechanism of the progression. However, lengthy studies of this magnitude require a staggering amount of time and resources. Without enough conclusive evidence the long-term administration of drugs in healthy individuals become substantially difficult due to ethical concerns.[37]

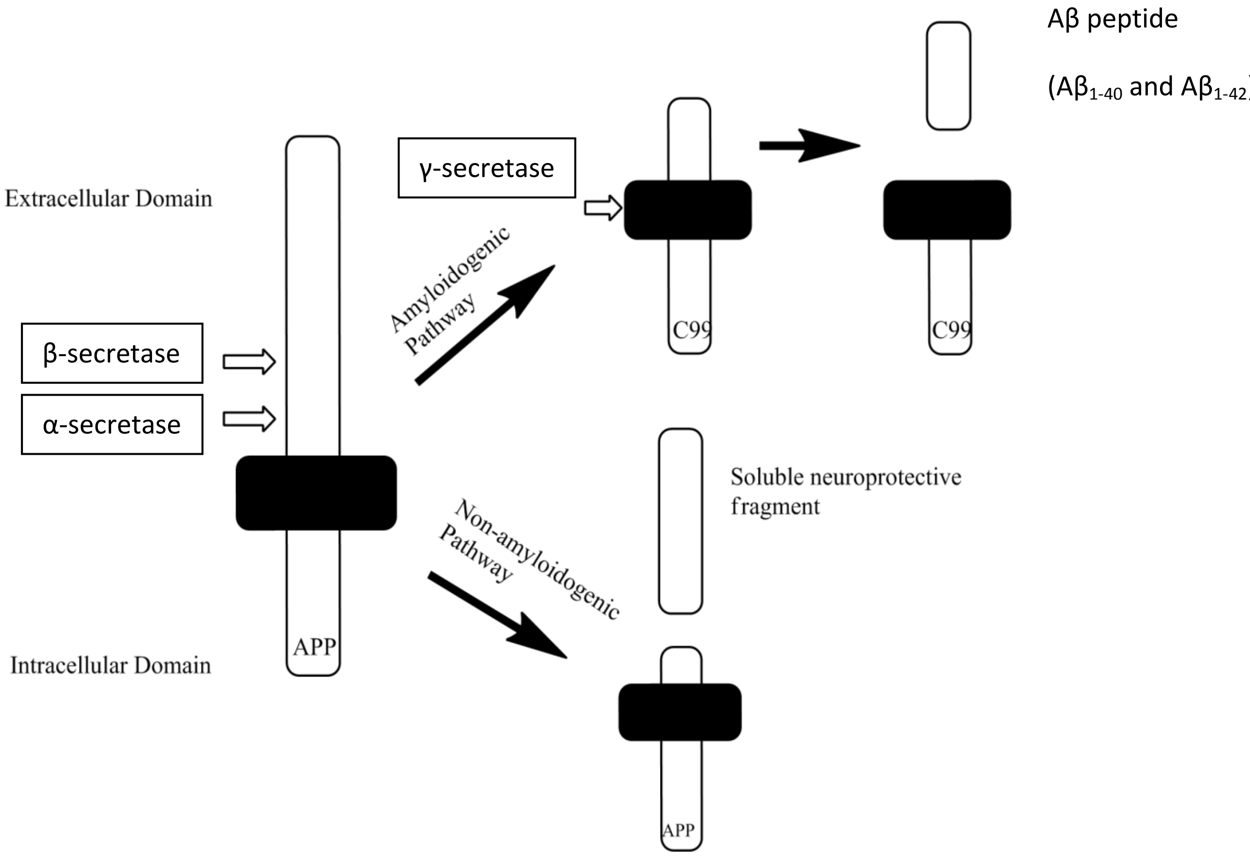

Figure 1.4: The amyloid cascade (amyloidogenic and non-amyloidogenic pathways)

1.3.1 Anti-amyloid strategies

Amyloid precursor protein is an integral membrane protein which had an unknown role or function up to its discovery. The explosion of interest regarding the amyloid hypothesis has lead researchers to delve into this protein to further understand its biological implications. Besides its notorious role for being processed into the smaller Aβ fragments, APP's normal role has been found to help with neuronal plasticity and regulate synapse formation.[38] The issue lies in the post-translational processing that APP goes through. There are two pathways; the non-amyloidogenic and amyloidogenic (**Figure 1.4**), regulated by α-secretase and successive actions of β and γ-secretases respectively.[39] In understanding the dynamic balance between the two APP processing pathways, it is established that α-secretase cleaves APP through the non-amyloidogenic pathway and produces an extracellular fragment that is neuroprotective. Researchers have looked at this approach of promoting the balance of APP processing towards the non-amyloidogenic pathway as a possible treatment option.[40] The amyloidogenic pathway comprises of successive cleavage of β and γ-secretase. Whereby the initial β-secretase cleavage releases an extracellular portion, and a membrane bound fragment called C99. Cleavage of the C99 by γ-secretase releases the key Aβ peptide.[41] γ-secretase has varied cleavage sites, thus it produces Aβ peptide in varied lengths from 39-42 amino acids. The most common form is a soluble $A\beta_{1-40}$ fragment, but it is the insoluble $A\beta_{1-42}$ form that implicates the most problems in AD (Figure 1.4).[42] The $A\beta_{1-42}$ form is longer, thus more hydrophobic in nature and is able to aggregate quickly via a number of different mechanisms.[43] The formation of aggregates has been studied extensively; starting from the dimerization of two $A\beta_{1-42}$ peptides, to eventual formation of smaller oligomeric peptides (approximately 3 – 10 $A\beta_{1-42}$ peptides).[44] Oligomers come together in a cross β-sheet conformation generating Aβ-protofilaments, and two protofilaments cross together in an intertwining fashion forming the Aβ fibril. Ultimately, when enough of these structures come together they form dense insoluble plaques.[45] A number of different factors affect the formation of these plaques in AD-diseased brains. In normal functioning individuals, Aβ is processed and inherent clearing mechanisms help reduce the amyloid load. In diseased brains, either the clearance mechanisms are hindered or the mis-processing of APP is heightened and the buildup of deposited Aβ allows for faster aggregation.[46] Once there is an excess of Aβ peptides a number of factors contribute to the aggregation including: i) The biophysical properties of Aβ peptides; ii) The PAS of AChE and iii) metal ions mediated aggregation.[47, 48, 49]

Aβ peptides have a conserved hydrophobic region that has been identified as the main seeding point of self-induced aggregation. The section of residues 15-20 of the Aβ peptide consists of KLVFFA.[50] Drug therapies targeting the self-induced aggregation of single Aβ peptides use this section as the starting point for developing aggregation inhibitors. Oligomers are able to form highly structured aggregates through cross β-sheet conformations, thus compounds that are able to disrupt this specific structure also inhibits aggregation.[51] Galantamine is an example of such inhibitor.[52] A key link between the cholinergic and amlyoid hypothesis is the AChE-induced aggregation of Aβ. The PAS of AChE acts as seeding point of Aβ due to its high concentration of aromatic residues.[53] Metal ions have also been shown to mediate the formation of Aβ species.[54] Three histidine residues, His6, His13 and His14 are conserved across all forms of Aβ and act as chelators of metal ions, coordinating around them. Copper, iron and zinc have been found to interact with Aβ species generating reactive oxygen species (ROS) that cause oxidative damage.[55]

Various phamacotherapies have been researched as possible forms of treatments towards the amyloid hypothesis. The idea of inhibiting either β or γ-secretase to limit the formation of Aβ species came about as the primary approach to dealing with the amyloid hypothesis. Studies done on mice expressing human APP mutations have shown major reduction of Aβ levels that lead to improved cognitive function when a β-secretase inhibitor was introduced.[56] However, the recent failure of β-secretase inhibitors at phase III clinical trials has been a setback to this particular route of therapy.[57] They failed to show any clinical effectiveness over placebo. Perhaps further studies involving the concept of the Aβ threshold levels need to be established before re-visiting the use of β-secretase inhibitors.[58] γ-secretase also acts as an attractive target, and semagacestat (**Figure 1.5**), a promising drug that reached phase III clinical trials also failed to show enough clinical efficacy.[59] Although work has been done on developing inhibitors, human testing has largely remained on hold due to the fact that inhibiting γ-secretase may interfere with notch signaling.[60] In this regard, an alternative method of γ-secretase modulation was reviewed. However, the failure of tarenflurbil (**Figure 1.5**) in phase III clinical trials again proved that dealing with the secretases is a complex mechanism that requires further investigation.[61] Aggregation inhibition has been another method used to block the formation of Aβ peptides into more toxic oligomers.[62] A need for a safer method has been found by either inhibiting the self-induced or AChE-induced Aβ aggregates using small molecules. They have been developed to be able to coordinate with various Aβ species to prevent the formation of higher order toxic oligomers.[63] Tramiprosate (**Figure 1.5**) was introduced as an agent to inhibit plaque formation by binding to smaller Aβ species, therefore not allowing them to reach higher order aggregates. However, its failure to show any clinical significance in phase III stages has led researchers into a re-evaluation of Aβ therapeutics.[64] The last method found was to aid in the reduction of already-formed Aβ plaques.[65] In order to help reduce toxicity neuronal damage, various methods were applied including the use of Aβ –specific antibodies as a means to supplement the body's clearance mechanisms.[66] One such example is bapinezumab, a humanized monoclonal antibody using active immunization that recognizes Aβ peptides and helps in the clearance mechanisms. Its development was eventually stopped due to a small number of patients developing vasogenic edema.[67] Even though these methods have been reviewed extensively, the overall view of the situation on Aβ is nearing a paradigm shift in focusing treatment options mainly on the prevention of Aβ deposition including the clearance of existing plaques.[68]

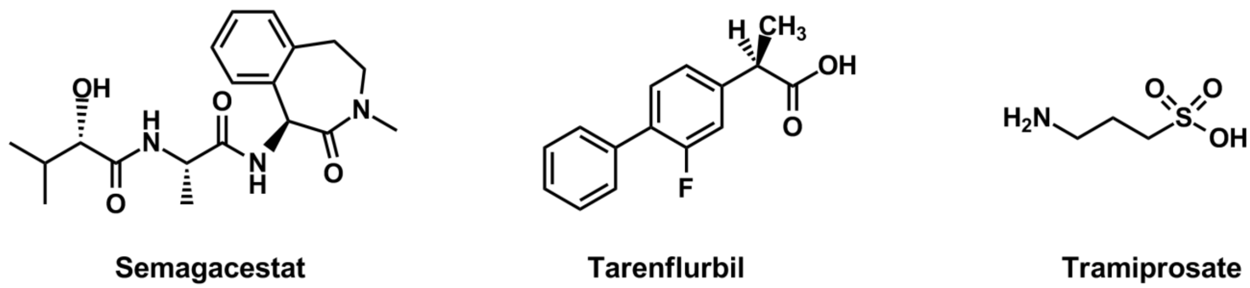

Figure 1.5: Chemical structures of semagacestat, tarenflubril and tramiprosate

1.4 Oxidative Stress Hypothesis

The oxidative stress hypothesis plays an important part in AD pathogenesis. Oxidative damage is regarded as an early event in AD, preceeding the deposition of Aβ and plaques.[69] Several studies have shown that increasing oxidative stress directly or indirectly increases intracellular Aβ levels.[70] In turn, this increase in levels of Aβ creates a negative feedback cycle that generates more reactive oxygen species (ROS). In terms of AD, oxidative stress biomarkers are elevated beyond normal levels in the brain indicating that there may be connections with disease progression. The AD brain is under significant amounts of oxidative stress in the forms of lipid peroxidation, protein oxidation, DNA oxidation, and mitochondrial dysfunction.[71] Coupled with the brain's natural high requirement for oxygen, high levels of poly unsaturated fatty acids (PUFAs) that are easily susceptible to oxidation, and its repressed anti-oxidant defenses it creates an environment for oxidative stress to thrive and cause multiple pathways of damage.[72] A number of clinical trials using anti-oxidative agents such as vitamin E and curcumin (**Figure 1.6**) have been underway to test the clinical efficacy of administering anti-oxidants as a potential therapeutic treatment.[73] In vitro experiments involving the use of vitamin E ameliorate oxidative damage, therefore it is believed to be a possible therapeutic option.[74] Another source to mediate oxidative stress is chelation of metal ions. In AD, many metal ions have been shown to take part in disease pathology. The Aβ oligomers are notorious for their ability to coordinate with copper and iron, and mediating redox reactions generating ROS.[75] The production of Aβ has also been directly involved in promoting a number of oxidative stress pathways including: protein oxidation, lipid peroxidation and generation of ROS, indicating key connections between the oxidative stress hypothesis and amyloid hypothesis.[76] Chelation therapy has also been developed with drugs like clioquinol (**Figure 1.6**) and its 2nd generation analog PBT2, for their potential to coordinate metal ions to reduce toxicity.[77] In an attempt to cover multiple targets of disease-modification, newer drug designs now strive to incorporate anti-oxidant moieties in their design in hopes to provide a solution for the oxidative stress hypothesis.

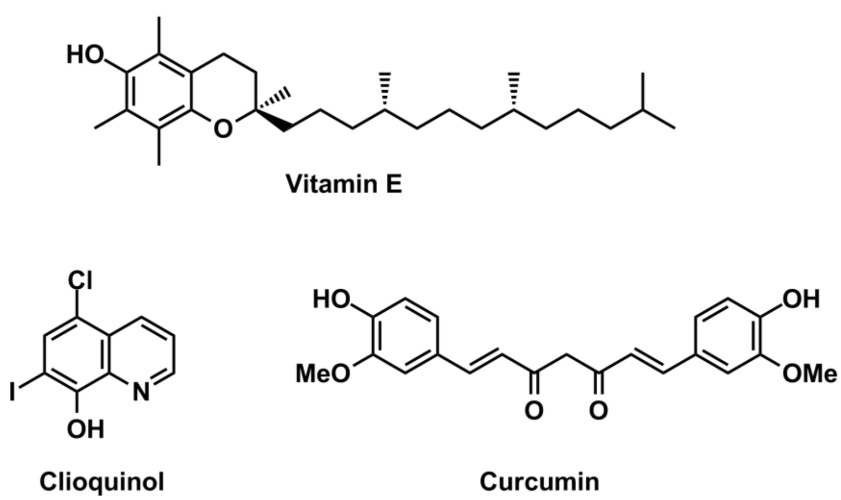

Figure 1.6: Chemical structures of vitamin E, curcumin and clioquinol

Lipid peroxidation in AD is characterized by the degeneration of lipids in cell membranes.[78] This damage is accelerated by the multiple processes that may contribute to the overall cascade; decreased biosynthesis, increased degradation and increased lipid peroxidation. One biomarker of oxidative stress is the thiobarbituric acid reactive structures (TBARS) as a measure of lipid peroxidation.[79] In a study with AD and age-matched controls, levels of TBARS in the AD group showed evelated levels in the hippocampus.[80] Lipid PUFAs are abundant in the brain in the forms of arachodonic, dosahexenoic, oleic, and stearic acids. A study has shown that all levels of these PUFAs are significantly decreased in AD brains versus age-matched controls, matching the predicted result that increased levels of lipid peroxidation should decrease the levels of PUFAs.[81] Another biomarker is 4-hydroxyalkenals (4-HNE) which is a direct product of PUFA peroxidation, specifically, arachadonic and dosahexenoic acids. Levels of 4-HNE are elevated in the ventricular cerebrospinal fluid (CSF) of AD patients, which is in direct contact with the brain, indicating that it is a potential biomarker for oxidative stress in AD brains.[82] The 4-HNE is responsible for a number of neurotoxic mechanisms; inhibition of DNA, RNA and protein synthesis, degradation of enzymes and disrupting calcium homeostasis. Cultured hippocampal neurons exposed to Aβ showed significant increase in levels of 4-HNE.[78] Another study specifically used $A\beta_{1-42}$ and showed neuronal cultures had increases in levels of 4-HNE, and that treatment with vitamin E was an effective treatment in scavenging ROS and stopping the oxidative damage.[74] Additionally, stereotaxic injection of 4-HNE in rat forebrain selectively inhibited cholineacetyltransferase (ChAT), that can decrease ACh biosynthesis as indicated in the cholinergic hypothesis, which provides another connection between the oxidative stress and cholinergic hypothesis.[83]

Protein oxidation is implicated in age-related neurodegenerative diseases. Vulnerable amino acid side chains and the protein backbone are subjects of potential oxidation, and thus the most often used biomarker is the protein carbonyl. The oxidative modification of proteins can lead to altered functionality, contributing to the overall damage done by oxidative stress. [84] In AD, protein oxidation has been confirmed. Studies have shown that $A\beta_{1-40}$, $A\beta_{1-42}$, $A\beta_{25-35}$ all directly induce protein oxidation and formation of ROS as levels of protein carbonyls was increased compared to controls.[85] Again, these effects are largely inhibited by the introduction of anti-oxidants. Data suggests that in the AD brain protein oxidation is specific towards certain proteins; β-actin and creatine kinase BB (CK). This implies that the mechanism of protein oxidation in AD is a selective process.[86] The β-actin is responsible for cell motility and structure and plays an integral role in cytoskeletal protein assembly, known to be altered in AD most likely due to ROS-mediated protein oxidation. The oxidation of CK modifies ATP production in the brain, which is required in a number of physiological functions such as controlling ion-pumps, and the synthesis of antioxidant proteins. The effects of CK oxidation was inhibited by the introduction of vitamin E.[87]

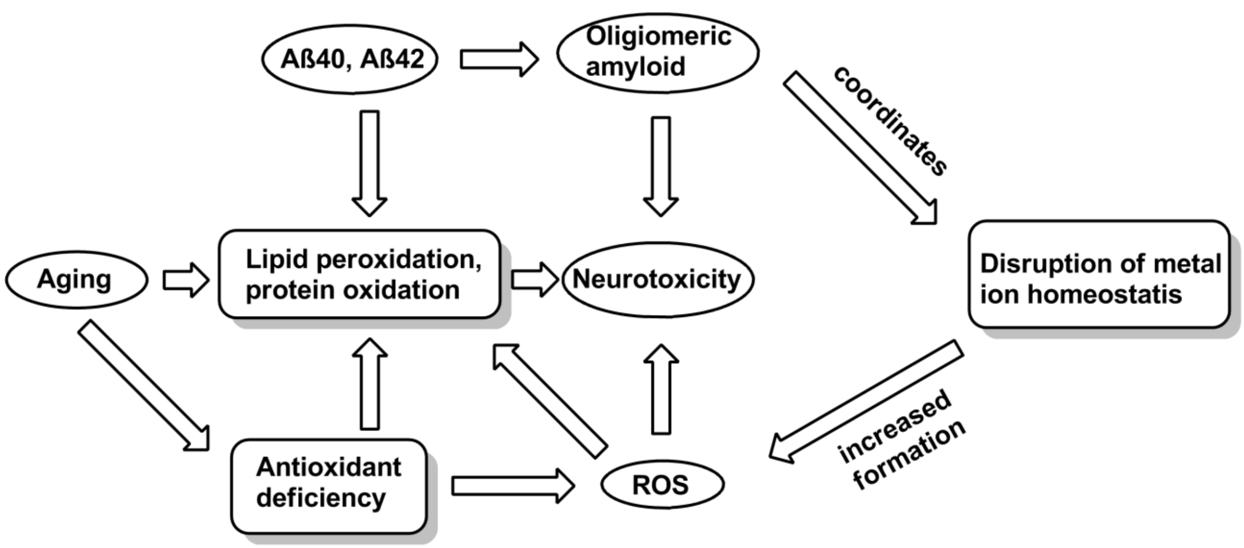

Figure 1.7: Summary of oxidative stress in AD pathophysiology

As mentioned above in both studies involving lipid and protein oxidation, the damaging effects are reduced when an antioxidant such as vitamin E is introduced. The effect of introducing an antioxidant is to help stop the further regeneration of ROS to prevent oxidative damage. The added advantage of using vitamins and natural compounds as a source of antioxidants is that they are well-characterized and tolerated, thus enrolling the use of vitamin E and C, and curcumin in long-term clinical studies has already been underway to validate their therapeutic effects on AD.[73, 74] Introducing compounds that have the potential to coordinate metal ions may be a valuable counteractive measure as well. Redox active compounds, copper and iron are known to proliferate the generation of ROS in AD.[75] In addition, Aβ aggregation is known to promote the formation of free radicals. Studies have implicated the role of Aβ in causing hydrogen peroxide accumulation in cultured hippocampal neurons and its role in inducing lipid peroxidation.[88] The direct influence of Aβ species on the brain's metal homeostasis has a number of implications. Copper, iron and zinc all play a role in mediating Aβ formation through coordination at various histidine residues.[76] The defective regulation of metal homeostasis caused by Aβ leads to production of ROS. The study of metal chelators such as PBT2 is one possibility, in hopes to provide disease-modifying relief to the oxidative stress hypothesis, it has shown promise in phase II clinical trials.[77] Though further studies are needed to elucidate the complex and multi-faceted nature of oxidative damage in the AD brain, multiple studies are underway in providing antioxidative relief, suggesting that oxidative stress is a viable target to develop anti-AD treatments. **Figure 1.7** provides a summary of the role of ROS in promoting amyloid toxicity and oxidative stress in AD pathophysiology.

1.5 Conclusion

There exist many other potential pathways for therapeutic effects for AD, including tau aggregation, modulators, MAO-B inhibitors and NMDA antagonists in an attempt to detect other disease-modifying therapeutics. The hyperphosphorylation of tau protein has been overlooked in recent years due to pathogenic studies finding that Aβ deposition precedes the downstream effects of tau.[89] Nevertheless, it still remains a prospective target for researchers to pursue. LMTX, a prodrug of Rember (**Figure 1.8**), is a tau aggregation inhibitor that has been enrolled in 2 phase III clinical trials. From the results shown in phase II, the use of LMTX has looked promising.[90] Tau protein modulators have been pursued as well, where protein kinase inhibitors are introduced to potentially block the hyperphosphorylation of tau. The tau protein is involved in microtubule stabilization, but hyperphosphorylated tau dissociates from microtubules, thus an alternate approach is to design for microtubule-stabilizing remedies.[91] The MAO-B inhibitors are another pathway to help mediate oxidative stress. The MAO-B is an enzyme that catalyzes the metabolism of neuroactive amines, and produces ROS in normal physiological conditions.[92] Levels of MAO-B are found to be elevated in neurodegenerative diseases such as AD, thus introducing inhibitors may help in slowing ROS damage.[93] Lastly the use of NMDA antagonists, namely memantine (**Figure 1.8**), helps alleviate the excitotoxicity caused by overactivation of glutaminegic receptors.[94] Memantine is the only FDA-approved drug in its class and has been found to provide clinically significant improvements when used in conjunction with a cholinesterase inhibitor.[95]

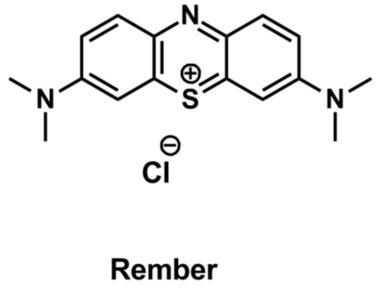

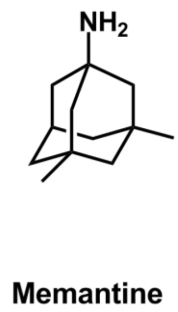

Figure 1.8: Chemical structures of Rember and memantine

Current drug therapies on the market follow the traditional: one drug, one target approach, in the form of different drugs targeting different hypotheses of AD. The lack of long-term efficacy of these therapeutics has led to a paradigm shift of the outlook towards AD treatment. The focus has been shifted to discovering and characterizing potential disease-modifying approaches that may slow or even halt the onset of AD. Therefore, there is a mandate for a newer generation of compounds with multi-target abilities endowed with these disease-modifying properties that tackle multiple pathways of AD as long term treatment options.

Chapter 2: Hypothesis and Design Rationale

2.1 Proposal

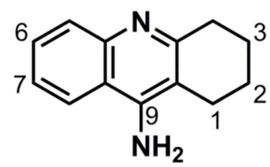

Figure 2.1: Chemical structure of tacrine

The fused tricyclic compound tacrine (**Figure 2.1**) was the first cholinesterase inhibitor developed in the pharmacotherapy of AD. Previous work in Dr. Nekkar Rao's lab has shown that C-9 substituted tacrine derivatives exhibit potent cholinesterase inhibition.[96] Based on these observations, our objective was to consider other tricyclic systems to design small molecules with ability to target the cholinergic, amyloid and oxidative stress pathways of AD pathophysiology as disease-modifying agents. In this regard, we considered both phenothiazine and phenoselenazine based tricyclics (**Figure 2.2**). The fused tricyclic rings are anticipated to interact with the cholinesterase catalytic site whereas functionalization of *N*-10 with suitable pharmacophores could provide anti-amyloid aggregation properties unlike tacrine. In addition, it is known that both phenothiazines and phenoselenazines can act as antioxidants.[97]

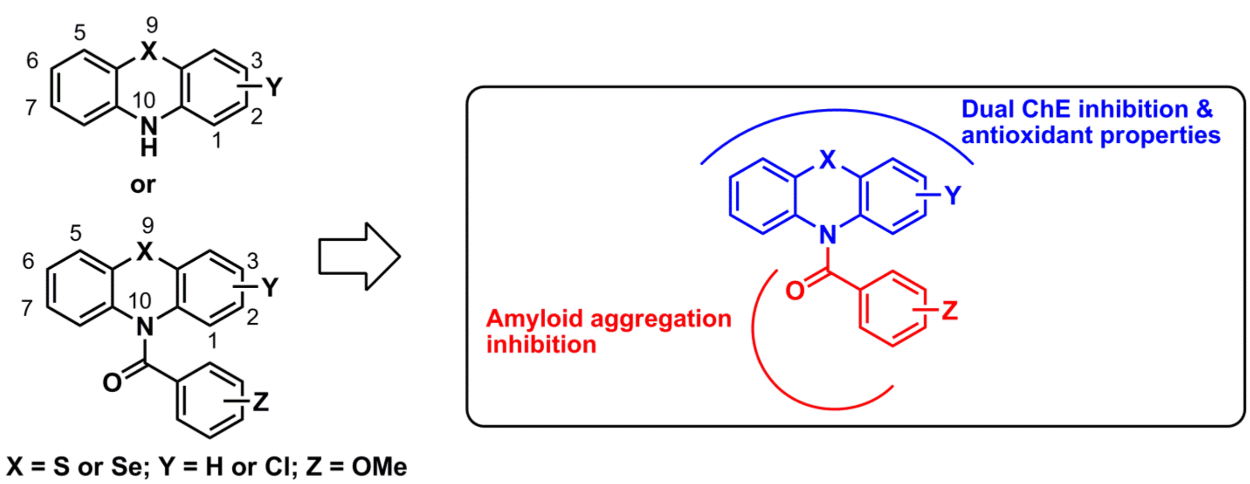

Figure 2.2: Proposed phenothiazines and phenoselenazines

2.2 Phenothiazines (PTZ)

PTZs represent an important class of bioactive molecules. Currently they are used to treat various types of psychotic disorders.[98] For example both chlorpromazine and fluphenazine are used in the clinical therapy as antipsychotic agents and exhibit dopamine receptor binding (D_2-antagonists) (**Figure 2.3**).[99] In a recent study Darvesh and coworkers have shown that *N*-10-carbonyl PTZs exhibit cholinesterase inhibition.[100] In addition, PTZs are known to act as antioxidants due to their ability to accept unpaired electrons from ROS and form resonance stabilized PTZ radicals that are less reactive .[101] The presence of a tricyclic ring system, chemically functionalizable *N*-10 and inherent antioxidant properties, support the design of PTZs as potential multi-targeting agents to treat AD.

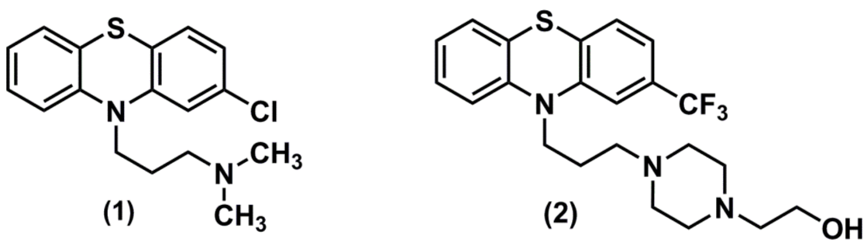

Figure 2.3: Chemical structures of chlorpromazine (**1**) and fluphenazine (**2**)

2.3 Phenoselenazines (PSZ)

PSZs are the selenium containing analogs of PTZs. Not much information is available on the biological properties of PSZs. Some early investigations on PSZs suggest that they exhibit similar antihistaminic and antipsychotic activity compared to their sulfur containing PTZ analogs.[102] A recent patent describes the application of phenoselenazinium compounds as anti-infective and anticancer agents.[103] Furthermore, PSZs are known to exhibit antioxidant properties although the exact mechanisms are not clear. It plausible that similar to PTZs, they can form a resonance stabilized PSZ radical. In addition, the presence of selenium itself could provide antioxidant properties. These characteristics support the development of PSZ as potential disease-modifying agents to treat AD.

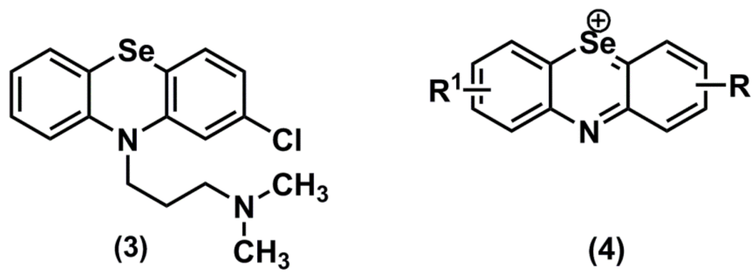

Figure 2.4: Chemical structures of some bioactive phenoselenazines (**3**) and (**4**)

2.3.1 Selenium

The trace element selenium (Se) is an essential micronutrient in the diet and is present in the amino acids selenocysteine and selenomethionine shown in **Figure 2.5**.[104, 105] Furthermore, the hydroperoxide scavenging antioxidant enzyme GPx is a selenoprotein where the active site amino acid selenocysteine is known to scavenge ROS and prevent oxidative damage.[64] Among the eight known GPx enzymes, GPx1 and GPx4 are known to provide neuroprotection in animal models of Parkinson's and AD.[106, 107] In addition, a recent study in AD patients indicated lower Se levels in the plasma, erythrocytes and nails compared to the control group suggesting that Se deficiency is a risk factor for AD.[108] Accordingly, efforts are on to develop selenium-containing small molecules as GPx mimics to prevent neurodegeneration. In this regard, ebselen [2-phenyl-1,2-benzisoselenazol-3(2H)-one, **Figure 2.5**] is a nontoxic organoselenium compound known to act as a GPx mimic and exhibits a number of pharmacological properties including antioxidant, anti-inflammatory, antiatherosclerotic, anticancer and neuroprotective activities.[109-114] Similar to glutathione, ebselen reacts with thiols to yield various organoselenium compounds. A key characteristic of ebselen is that each intermediate exhibits antioxidant activity, and that it is regenerated in a redox cycle making it an efficient compound in boosting the antioxidant defense system. These studies indicate that selenium-based small molecules represent a promising class of agents to potentially treat AD.

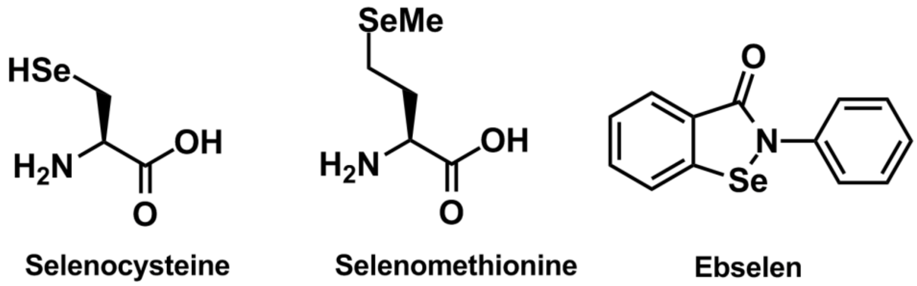

Figure 2.5: Examples of selenium-containing biomolecules and compounds

2.4 Conclusion

Fused tricyclic ring systems based on either a PTZ or a PSZ have the potential to serve as suitable ring templates to design novel small molecules to target multiple factors associated with AD pathophysiology including the cholinergic dysfunction, amyloid cascade and oxidative stress pathway. In this regard, the proposal aims to design novel PTZ and PSZ derivatives. The effect of steric and electronic properties on their biological properties are evaluated by varying substituents at the C-2 and *N*-10 position to acquire structure activity relationship (SAR) data. It is anticipated that the results will be provide useful insight into the design and development of novel tricyclics as disease-modifying agents with potential application to treat AD.

Chapter 3: Synthetic Chemistry

3.1 Introduction

This chapter describes the synthetic strategies used to prepare PTZ and PSZ derivatives. Commercially available starting materials, unsubstituted phenothiazine and 2-chlorophenothiazine were coupled to various acyl chlorides under mild conditions to obtain *N*-acyl-PTZ derivatives whereas PSZ derivatives were prepared by coupling synthesized diphenylamines with selenium and selenium dioxide to obtain the PSZ template which was acylated to obtain *N*-acyl-PSZ derivatives.

3.2 Proposal

3.2.1 Synthesis of PTZ Derivatives

The PTZ with either hydrogen or chlorine substituent at C-2 and various *N*-10 substituents (benzoyl, phenylacetyl, hydrocinnamoyl, 3-methoxybenzoyl, 4-methoxybenzoyl and 3,4-dimethoxybenzoyl) were synthesized.[115] **Figure 3.1** provides the chemical structures of PTZ derivatives synthesized.

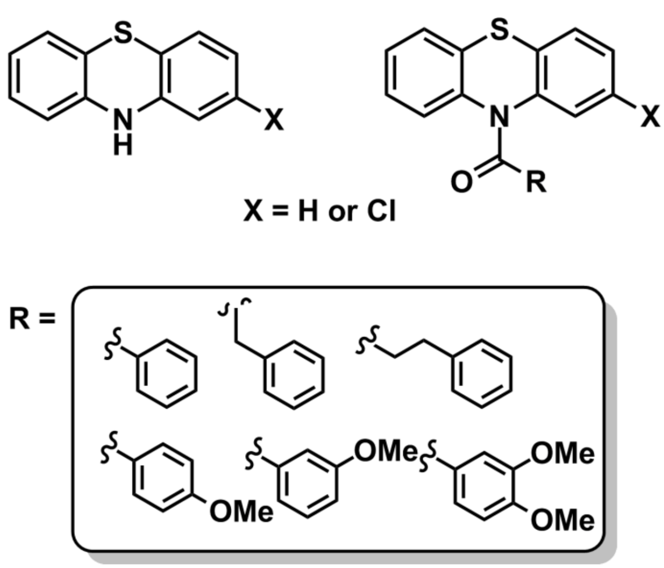

Figure 3.1: PTZ compound library synthesized

3.2.2 Synthesis of PSZ Derivatives

Selenium analogs of PTZ, namely, PSZ (**15a-l**) were also synthesized with either hydrogen or chlorine substituent at C-2 and various *N*-10 substituents (benzoyl, phenylacetyl, hydrocinnamoyl, 3-methoxybenzoyl, 4-methoxybenzoyl and 3,4-dimethoxybenzoyl).[115] **Figure 3.2** provides the chemical structures of PSZ derivatives synthesized.

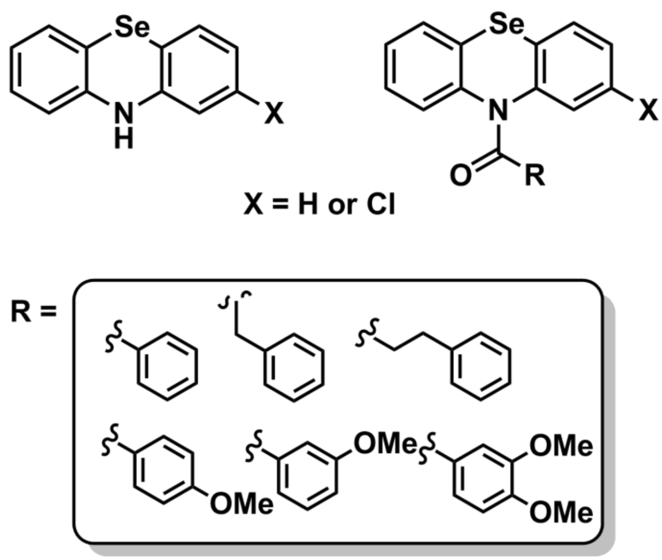

Figure 3.2: PSZ compound library synthesized

3.3 Results

3.3.1. PTZ Derivatives

The *N*-acyl PTZ derivatives **7a-l** were prepared by coupling either unsubstituted phenothiazine (**5**) or 2-chlorophenothiazine (**6**) with appropriate acyl chlorides (benzoyl, phenylacetyl, hydrocinnamoyl, 3-methoxybenzoyl, 4-methoxybenzoyl and 3,4-dimethoxybenzoyl chlorides) in anhydrous toluene by refluxing overnight (**Scheme 3.1**). The PTZs were purified by flash chromatography and were characterized by ^{1}H NMR and mass spectrometry. The yields ranged from 70-95%.

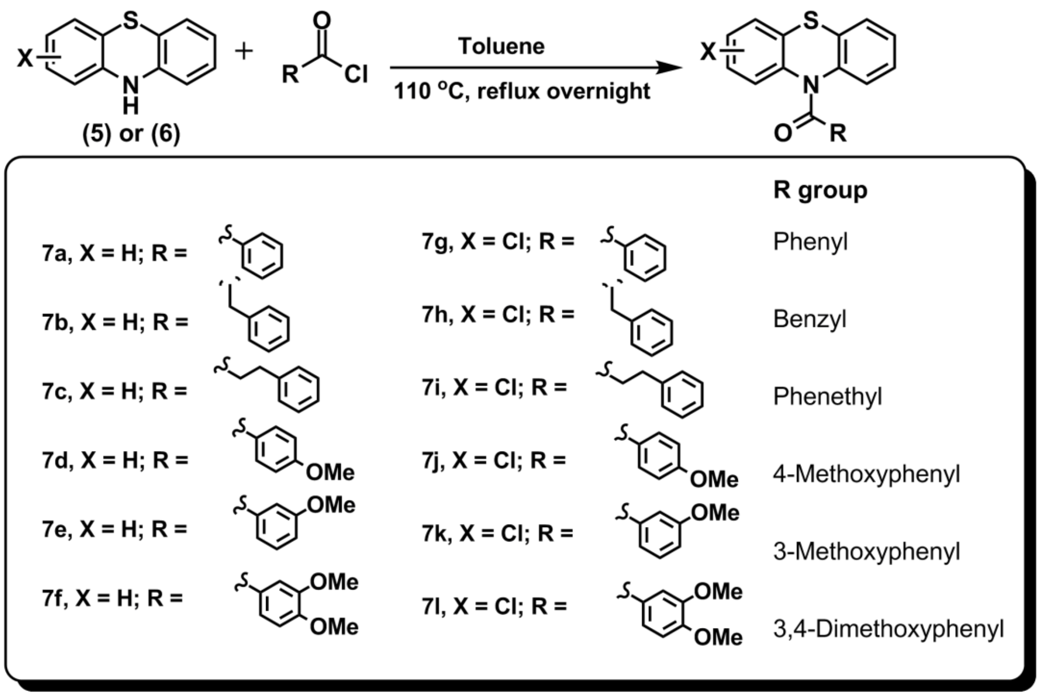

Scheme 3.1: Synthesis of PTZ derivatives **7a-l**

3.3.2 PSZ Derivatives

3.3.2.1 Diphenylamine (DPA) synthesis

Aniline (**8**) or 3-chloroaniline (**9**), were coupled with phenylboronic acid to obtain either DPA (**11**) or 3-chloro DPA (**12**) respectively using a copper catalyst (**Schemes 3.2 – 3.4**),[116-118] or by a 2-step metal-free synthesis (**Schemes 3.5 – 3.6**).[119, 120] The metal-free synthesis required the preparation of an α-iodinated cyclohex-2-ene (**10**). The DPA's were obtained by aqueous work-ups and purified by flash chromatography and characterized by ^{1}H NMR and mass spectrometry. The yields ranged from 10 - 60%.

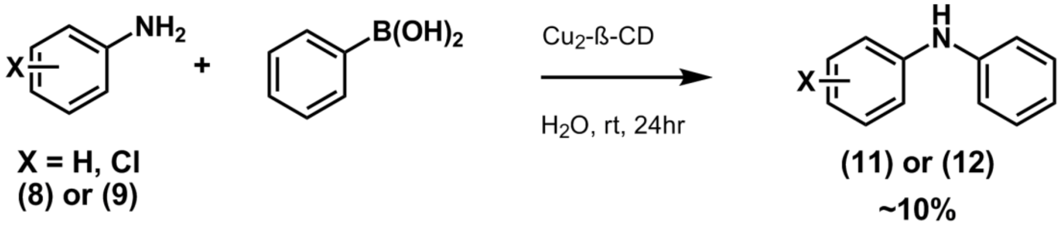

Scheme 3.2: Copper-mediated synthesis of DPA (**11**), 3-Cl DPA (**12**) – method 1[116]

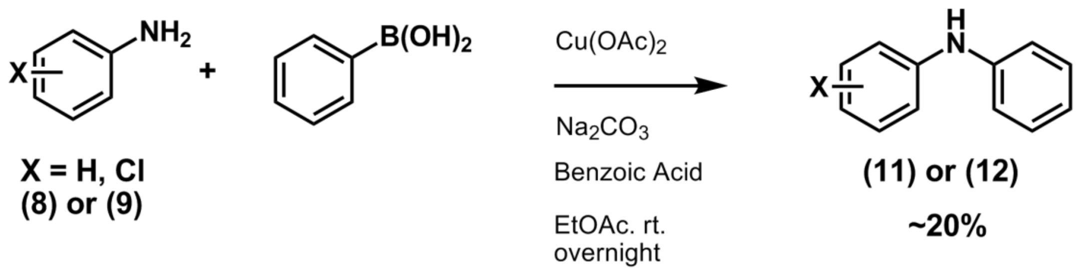

Scheme 3.3: Copper-mediated synthesis of DPA (**11**), 3-Cl DPA (**12**) – method 2[117]

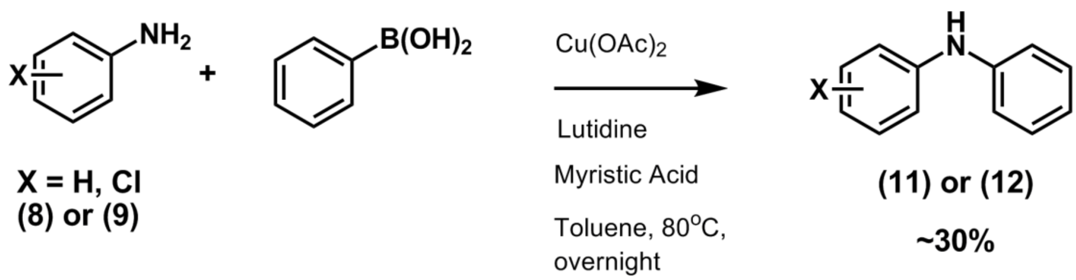

Scheme 3.4: Copper-mediated synthesis of DPA (**11**), 3-Cl DPA (**12**) – method 3[118]

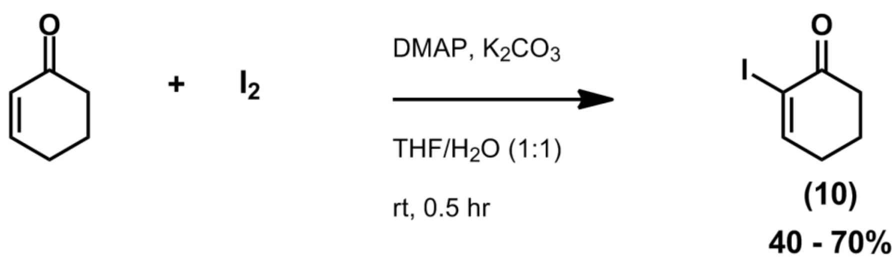

Scheme 3.5: Metal-free synthesis of DPA (**11**), 3-Cl DPA (**12**) – step 1, formation of an α-iodinated cyclohex-2-ene (**10**)[119]

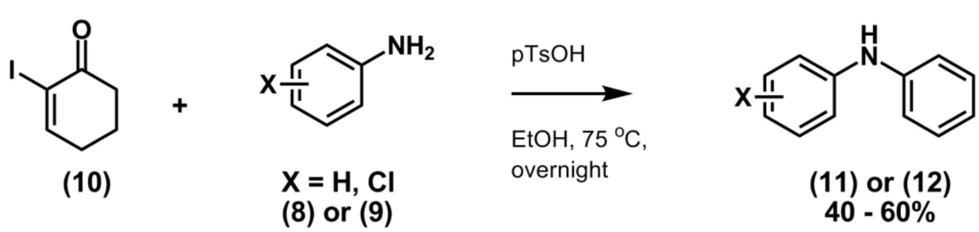

Scheme 3.6: Metal-free synthesis of DPA (**11**), 3-Cl DPA (**12**) – step 2[120]

3.3.2.2 Phenoselenazine (PSZ) synthesis

Phenoselenazine (**13**) and 2-chlorophenoselenazine (**14**) was synthesized from DPA (**11**) or 3-Cl DPA (**12**) either from coupling with selenium monochloride[121] or with selenium and selenium dioxide[122] (**Scheme 3.7** and **3.8** respectively). The respective phenoselenazines were purified by flash chromatography and characterized by ^{1}H NMR and mass spectrometry. The yields ranged from 15 – 25%.

Scheme 3.7: Phenoselenazine (**13, 14**) synthesis (method 1)[121]

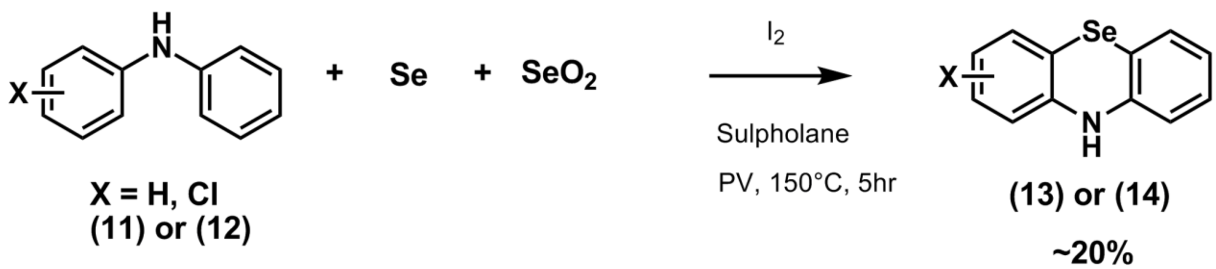

Scheme 3.8: Phenoselenazine (**13, 14**) synthesis (method 2)[122]

3.3.2.3 Synthesis of N-acyl-PSZ derivatives

The *N*-acyl PSZ derivatives **15a-l** were prepared by coupling either unsubstituted phenothiazine (**13**) or 2-chlorophenothiazine (**14**) with appropriate acyl chlorides (benzoyl, phenylacetyl, hydrocinnamoyl, 3-methoxybenzoyl, 4-methoxybenzoyl and 3,4-dimethoxybenzoyl chlorides) in anhydrous toluene by refluxing overnight (**Scheme 3.9**). The PTZs were purified by flash chromatography and were characterized by ^{1}H NMR and mass spectrometry. The yields ranged from 30-95%.

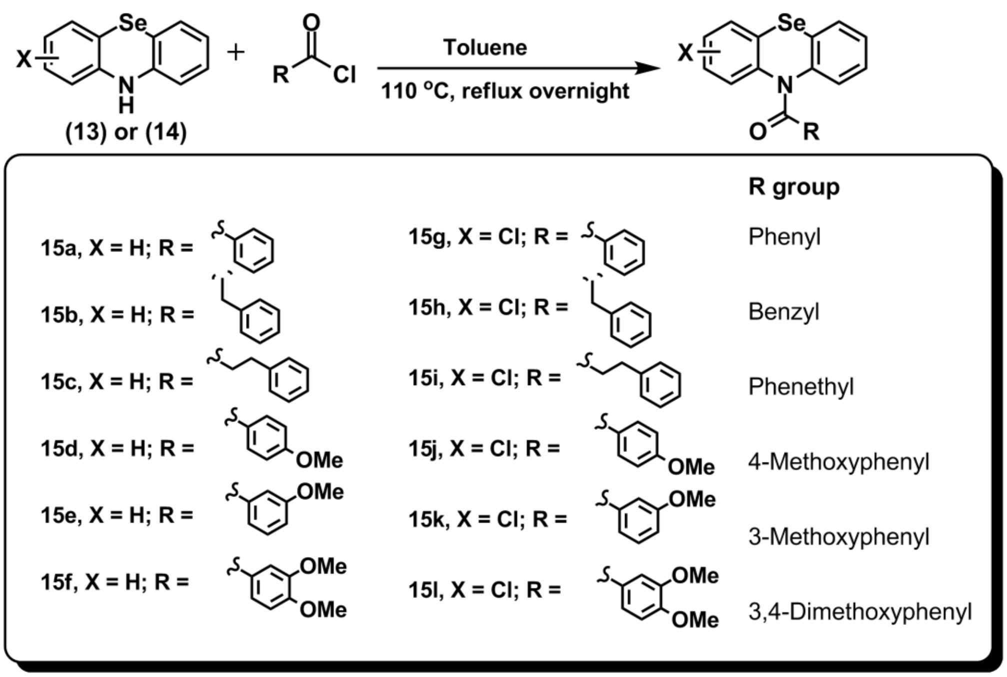

Scheme 3.9: Synthesis of PSZ derivatives **15a-l**

3.4 Mechanisms and Protocols

3.4.1 PTZ Derivatives

N-acyl PTZ derivatives **7a-l** were prepared by coupling either unsubstituted phenothiazine (**5**) or 2-chlorophenothiazine (**6**) with appropriate acyl chlorides (benzoyl, phenylacetyl, hydrocinnamoyl, 3-methoxybenzoyl, 4-methoxybenzoyl and 3,4-dimethoxybenzoyl chlorides) in anhydrous toluene by refluxing overnight (**Scheme 3.1**). The mechanism consisted of a nucleophilic attack by the N-10 secondary amine of the PTZ leading to displacement of the chloride ion.

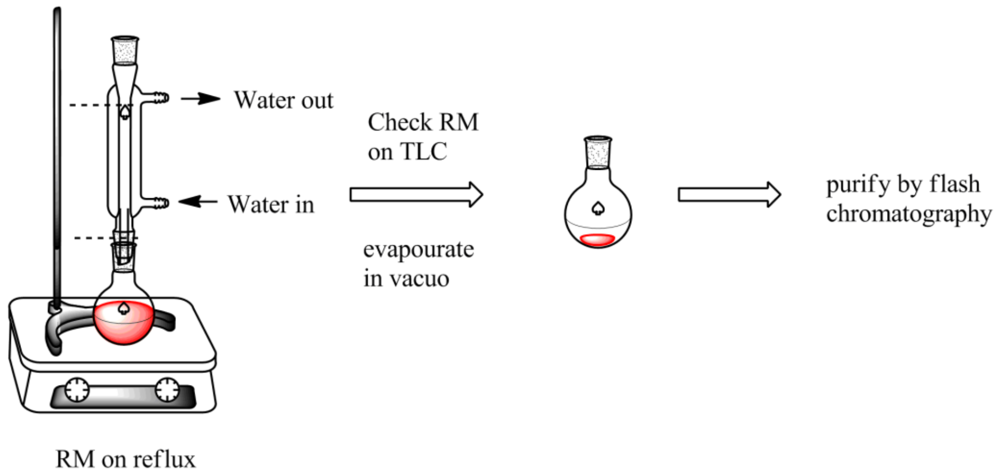

Figure 3.3: General setup for the synthesis of PTZ derivatives **7a-l**

3.4.2 PSZ Derivatives

3.4.2.1 Diphenylamine synthesis

To either aniline (**8**) or 3-chloroaniline (**9**), phenylboronic acid was added, forming either diphenylamine (**11**) or 3-chloro diphenylamine (**12**) respectively. Various reaction conditions were tried. The first method involved a copper(II)-β-cyclodextrin complex added together with phenylboronic acid and aniline in water at room temperature (**Scheme 3.2**). The aqueous layer was then extracted with DCM and a subsequent column was run to purify the product. The use of the copper-(II)-β-cyclodextrin produces a metallic complex that acts as the reaction vessel, and the traditional oxidative addition, transmetallation and reductive elimination cycle is predicted to drive the reaction forward (**Figure 3.4**).

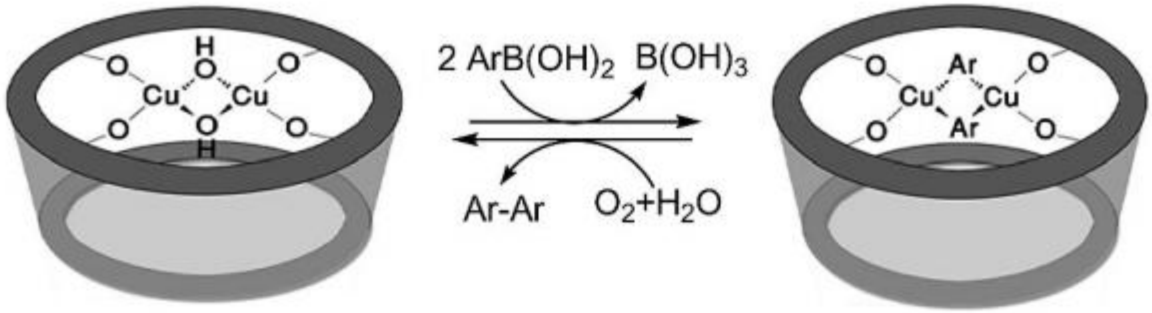

Figure 3.4: A proposed mechanism of action for Scheme 3.2[116]

The second and third method involved using copper acetate as the catalyst (**Scheme 3.3** and **3.4**). In **Scheme 3.3**, the reactants were added together with sodium carbonate and benzoic acid in EtOAc at rt. In **Scheme 3.4**, the reactants were added together with lutidine and myristic acid and refluxed at 80°C overnight. Upon completion both reaction mixtures were washed with 10% HCl and extacted with DCM, then purified by flash chromatography. Unlike the bulky cyclodextrin complex see in **Figure 3.4**, these two methods follow the traditional catalytic cycle seen. Initially, phenylboronic acid is coordinated to copper through transmetallation to form intermediate A. Coordination with aniline forms intermediate B, which then undergoes oxidation with dioxygen forming intermediate C. Through reductive elimination of C, the desired diphenylamine (**11** or **12**) is released, and copper is reduced at stage D. The last step regenerates the copper by oxidation with water forming complex E (**Figure 3.5**).

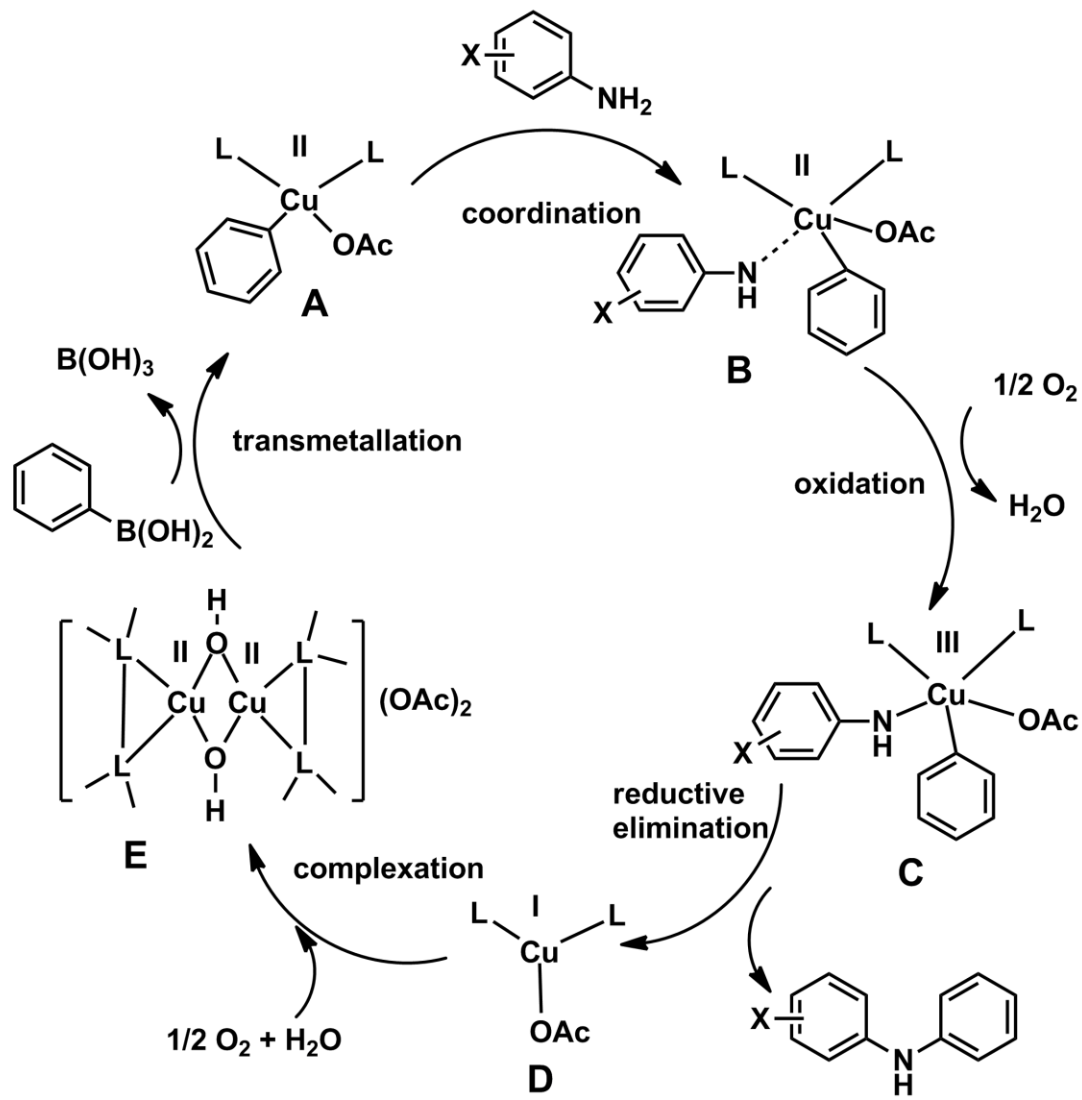

Figure 3.5: A proposed general mechanism of the copper-catalyzed DPA synthesis (Chan-Lam coupling)

Another method used a metal-free approach towards the synthesis of diphenylamines (**11** or **12**) seen in **Schemes 3.5** and **3.6**. Preparation of the α-iodinated 2-cyclohex-2-enone (**10**) involved the addition of cyclohex-2-enone with iodine, using DMAP as a catalyst and potassium carbonate as a quenching agent in a 1:1 mixture of THF:H_2O. The reaction mixture was diluted with EtOAc and washed with sodium thiosulfate and 10% HCl. The product was then purified by flash chromatography. The DMAP activates cyclohex-2-enone by attacking via a Michael addition, forming a zwitterionic intermediate, hence the use of water to help in the stability of the intermediate. Through a subsequent nucleophilic attack to iodine, the α-iodinated intermediate is formed. The iodide ion liberates hydrogen iodide (HI) and regenerates DMAP (**Figure 3.6**).

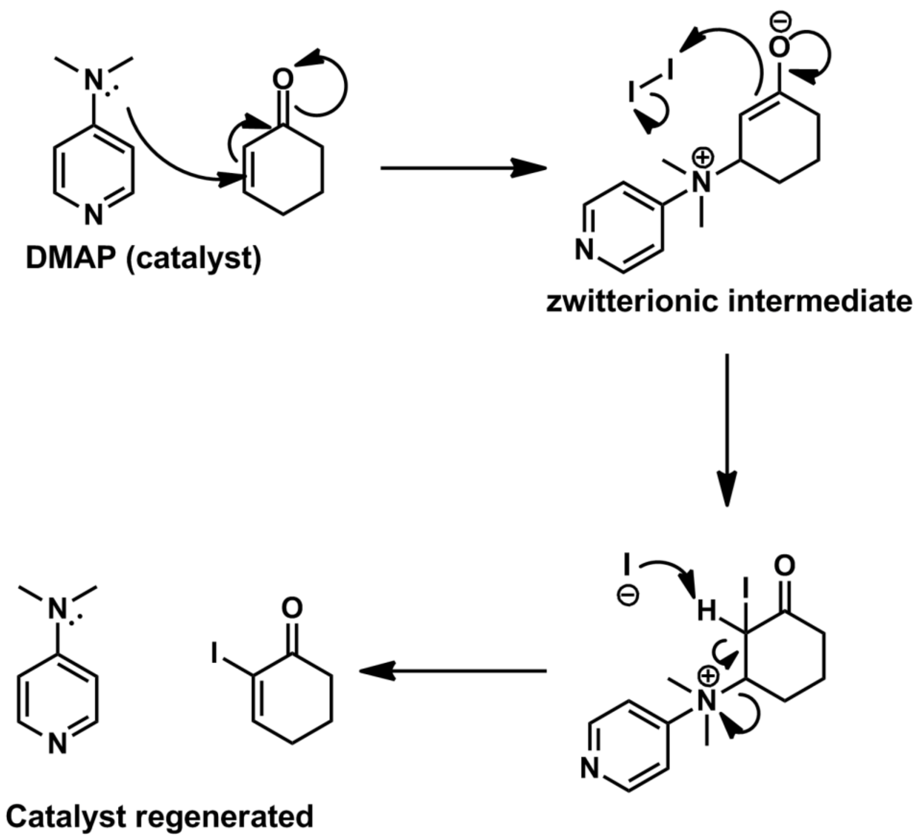

Figure 3.6: Proposed mechanism of action for Scheme 3.5, synthesis of α-iodinated 2-cyclohex-2-enone (**10**)

The second step in the metal-free approach was the coupling of the α-iodonated 2-cyclohex-2-enone (**10**) with either aniline (**8**) or 3-chloroaniline (**9**). The two starting materials were added together in EtOH with a stochiometric amount of p-TsOH (20 mol %) and refluxed overnight. The reaction mixture was then diluted with EtOAc and washed with 20% sodium bicarbonate and brine. The product was purified by flash chromatography. In an acidic environment the primary amine attacks the eletrophilic carbonyl, through subsequent protonation/de-protonation steps water is eliminated and the nitrogen replaces the oxygen forming the imine/enamine tautomerization pair. While in the enamine form, a hydride shift occurs, allowing the iodine to be eliminated in the form of HI, thus forming the final product (**Figure 3.7**).

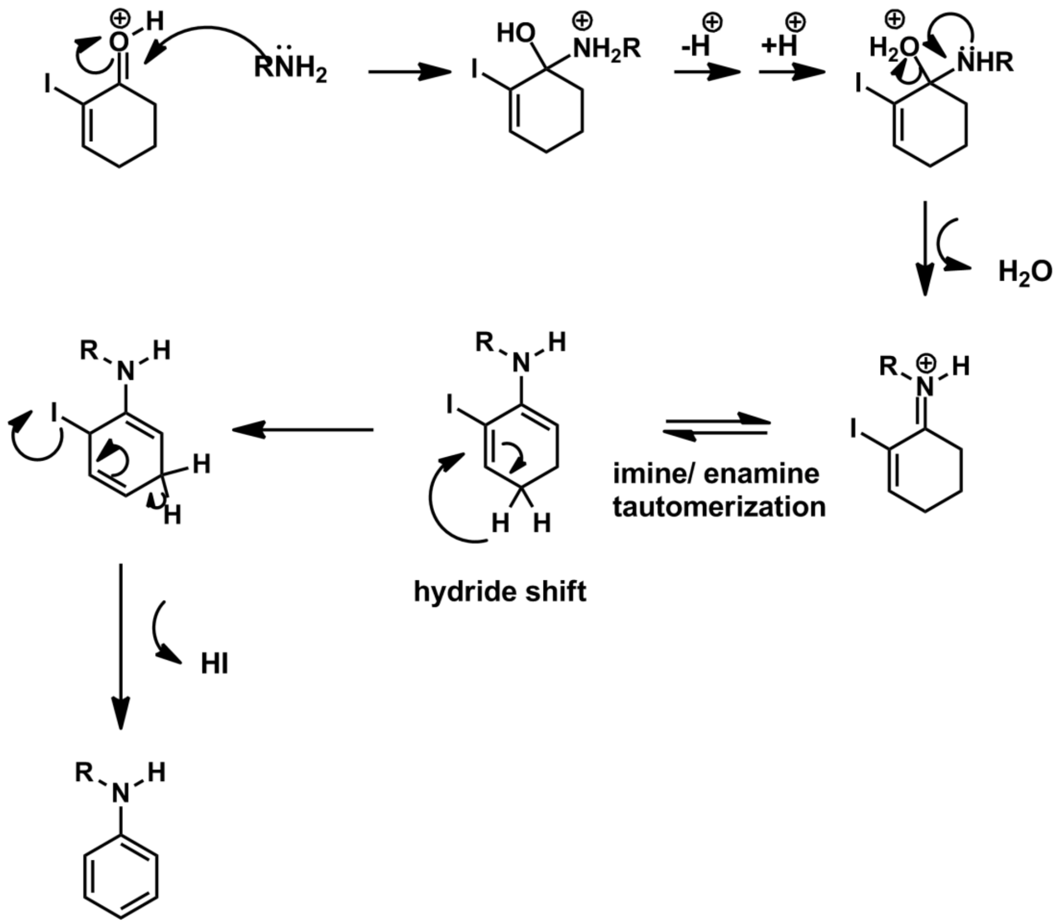

Figure 3.7: Proposed mechanism of scheme 3.6, the second step of the metal-free approach

The general sequence of steps used in the preparation of DPA (**11** and **12**) is given in **Figure 3.8**.

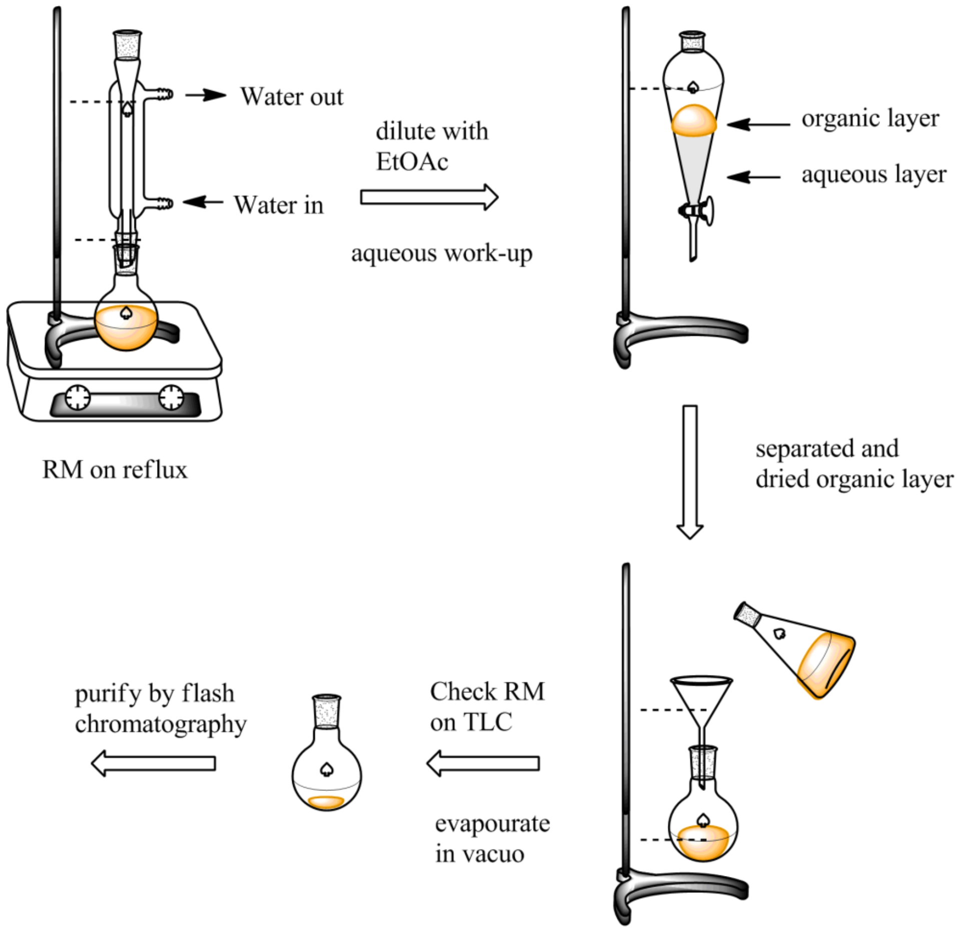

Figure 3.8: General setup for the synthesis of DPA (**11**) or 3-chloro DPA (**12**)

3.4.2.2 Phenoselenazine (PSZ) synthesis

Phenoselenazine (**13**) and 2-chlorophenoselenazine (**14**) was synthesized from DPA (**11**) or 3-Cl DPA (**12**) either from coupling with selenium monochloride (**Scheme 3.7**) or with selenium and selenium dioxide (**Scheme 3.8**). In **Scheme 3.7**, the source of selenium was selenium monochloride which was added with either DPA (**11**) or 3-Cl DPA (**12**) in DCM, refluxing for 6 hrs. In **Scheme 3.8** the source of selenium was selenium metal (limiting reagent). It is consumed and converted to hydrogen selenide. In an attempt to maximize yield, selenium dioxide was added to help regenerate selenium metal in-situ in the presence of hydrogen selenide (**Figure 3.9**).

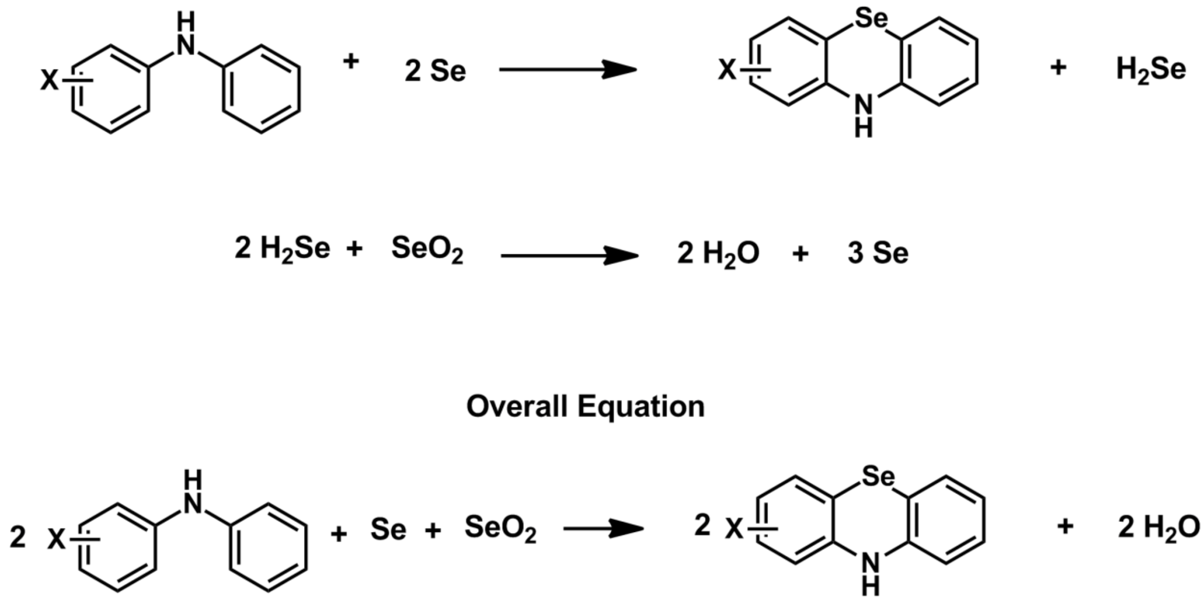

Figure 3.9: In-situ regeneration of selenium for **Scheme 3.8**

Selenium metal, thus was added with selenium dioxide and iodine in sulpholane and placed in a PV in an oil bath at 150 °C for 5 hrs. Both reaction mixtures were cooled and filtered in DCM plugs of celite and purified by flash chromatography. The proposed reaction mechanism is similar for both schemes, in **Scheme 3.7**, selenium is already coordinated with chloride, and **Scheme 3.8** has the catalytic iodine coordinating with selenium. The selenium then acts as the electrophile, and through a sequential nucleophilic aromatic substitution, the core PSZ structure is closed off (**Figure 3.10**). **Figure 3.11** highlights the general setup for these two schemes.

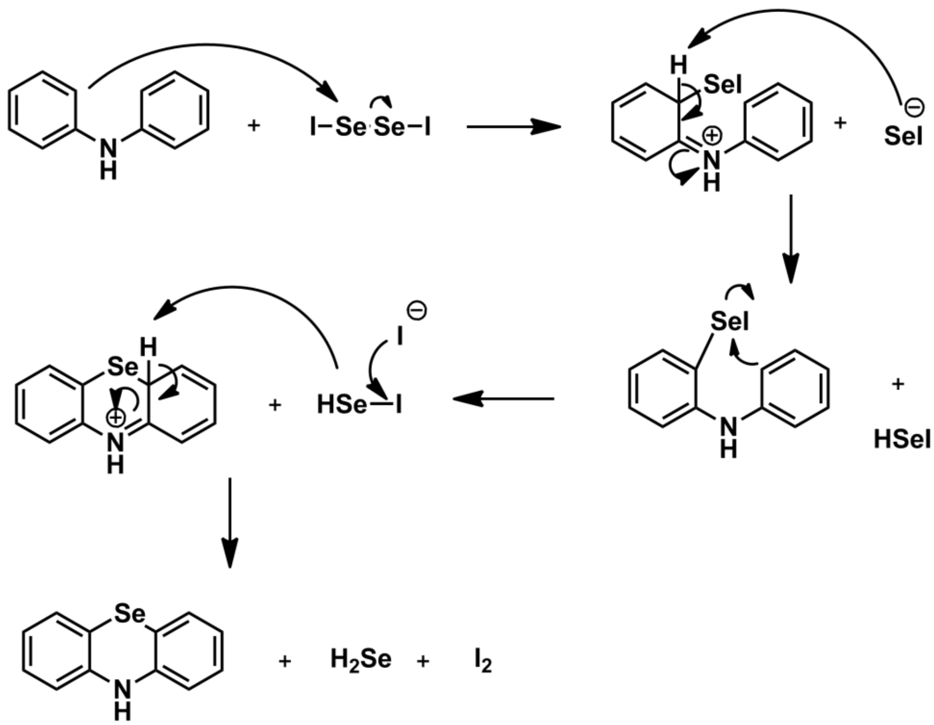

Figure 3.10: Proposed mechanism for the synthesis of phenoselenazine (**13**) and 2-chlorophenoselenazine (**14**)

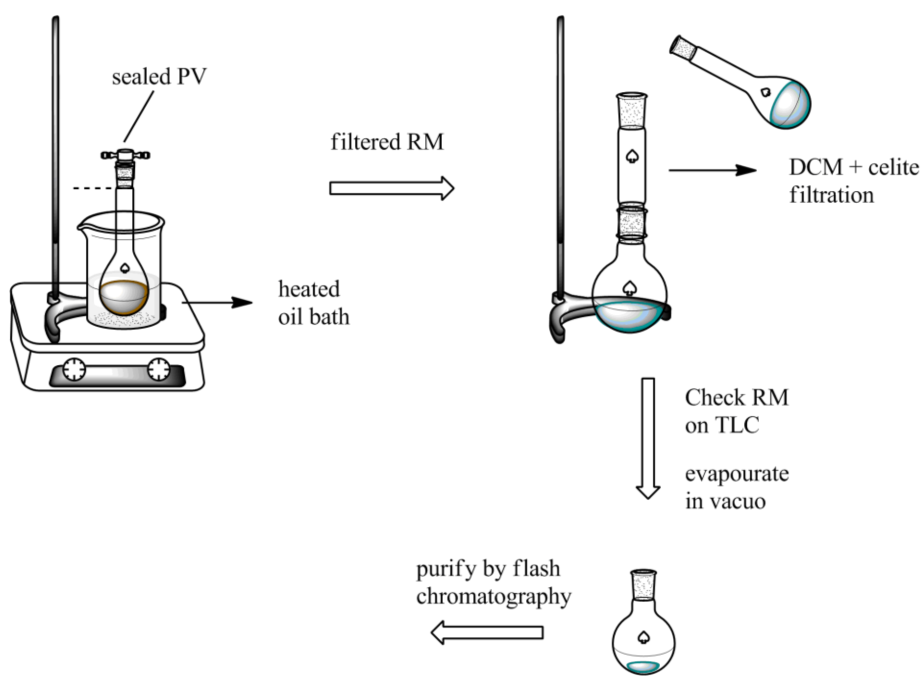

Figure 3.11: General setup for synthesis of phenoselenazine (**13**) and 2-chlorophenoselenazine (**14**)

3.4.2.3 Synthesis of N-acyl-PSZ derivatives

Similar to that of the PTZ series (**7a-l**), the *N*-acyl PSZ derivatives **15a-l** were prepared by coupling either unsubstituted phenoselenazine (**13**) and 2-chlorophenoselenazine (**14**) with appropriate acyl chlorides (benzoyl, phenylacetyl, hydrocinnamoyl, 3-methoxybenzoyl, 4-methoxybenzoyl and 3,4-dimethoxybenzoyl chlorides) in anhydrous toluene by refluxing overnight (**Scheme 3.9**). The PSZs were purified by flash chromatography. The mechanism consisted of a nucleophilic attack by the secondary amine of the PSZ leading to the displacement of the chloride ion to form N-acyl PSZ derivaties.

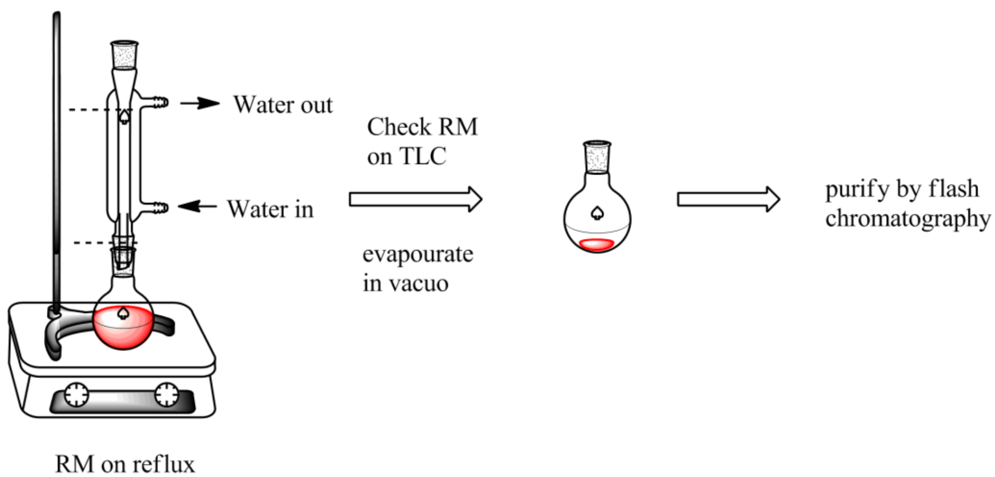

Figure 3.12: General setup for the synthesis of PSZ derivatives **15a-l**

3.5 Conclusion

The synthesis of PTZ derivatives (**7a-l**) were straightforward as starting precursors were readily available. The synthesis of PSZ was achieved in 3 steps (i) synthesis of DPA (**11**) or 3-Cl DPA (**12**) (ii) synthesis of phenoselenazine (**13**) and 2-chlorophenoselenazine (**14**) and (iii) N10 coupling to obtain PSZ derivatives **15a-l**. A total of 26 compounds were synthesized and characterized as potential anti-AD agents.

Chapter 4: Biological Evaluation

4.1 Introduction

The biological activities of synthesized PTZ derivatives **7a-l** and PSZ derivatives **15a-l** were evaluated using a number of assay protocols including human cholinesterase inhibition (using both AChE and BuChE), anti-amyloid aggregation assay using $A\beta_{1-42}$ peptide, antioxidant assay and cell viability/toxicity assay at various compound concentrations. This chapter describes the assay principles, structure activity relationship (SAR) data acquired and discusses the ability of PTZ and PSZ derivatives to target multiple factors associated with AD pathophysiology.

4.2 Human Cholinesterase Inhibition Studies

4.2.1 Assay Principle

The cholinesterase (ChE) screening assay is based on Ellman's method, a standard method in testing the inhibition of both acetylcholinesterase (AChE) and butyrylcholinesterase (BuChE).[123] The colorimetric assay utilizes thio-ester analogs of acetylcholine (ACh) and butyrylcholine (BuCh) as the substrate, which when hydrolyzed to their free-thiol form reacts with 5,5'-dithiobis-(2-nitrobenzoic acid) (DTNB) to form a yellow chromophore at 405-412 nm (**Figure 4.1**). From the compound screening, ChE inhibition profiles were obtained through the monitoring of the chromophore formed by UV spectroscopy. Known ChE inhibitors, tacrine, donepezil and galantamine were used as reference agents for comparison.

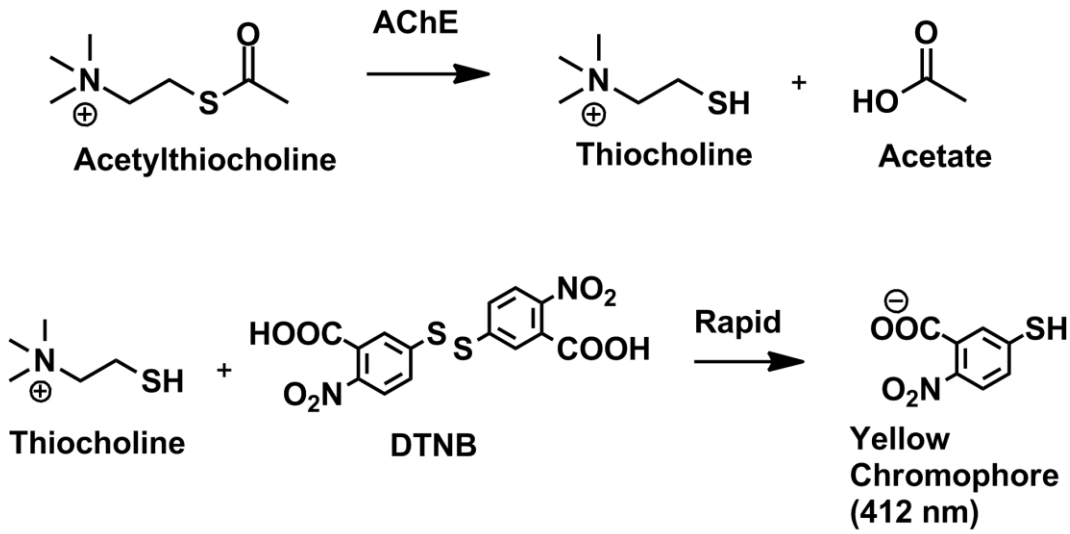

Figure 4.1: Cholinesterase assay principle

4.3 Results and Discussion

4.3.1 PTZ Derivatives SAR

The unsubstituted PTZ's (**5** and **6**) and its derivatives **7a-l**, were evaluated for their ability to inhibit both human AChE and BuChE enzymes. Their activity was compared to known cholinesterase inhibitors tacrine, donepezil and galantamine (**Table 4.1**). The unsubstituted PTZ derivative **5** exhibited an IC_{50} value of 7.37 μM towards human AChE and was less potent compared to reference agents tacrine (AChE IC_{50} = 0.16 μM), donepezil (AChE IC_{50} = 0.04 μM) and galantamine (AChE IC_{50} = 2.60 μM). Addition of an *N*-benzoyl substituent in compound **7a** retained AChE inhibition (IC_{50} = 8.10 μM) and the compound was less potent compared to **5**. The effect of aromatic acyl groups with one (benzyl) and two carbon spacer (phenethyl) on AChE inhibition were explored (compounds **7b** and **7c**). These modification provided AChE inhibition and both compounds **7b** (AChE IC_{50} = 7.40 μM) and **7c** (AChE IC_{50} = 7.15 μM) exhibited similar activity as compared to **5** (AChE IC_{50} = 7.37 μM) although they were less potent compared reference agents. Our previous work has shown that the presence of a 3,4-

dimethoxyphenyl substituent provided good cholinesterase inhibition.[96] Accordingly the effect of methoxyphenyl substituents was explored by evaluating compounds **7d**-**f** (**Table 4.1**). Interestingly, these compounds exhibited AChE inhibition ranging from 5.80 to 6.20 µM (IC_{50}s) and were more potent compared to compounds **5** and **7a**-**c**. The 3,4-dimethoxybenzoyl compound (**7f**) was identified as the most potent AChE inhibitor (IC_{50} = 5.80 µM). Furthermore, the addition of C-2 chlorine to the PTZ scaffold was investigated. It appears that C-2 chlorine substituent was not a major factor in AChE inhibition and C-2 chloro-PTZ derivatives **7g**-**l** exhibited IC_{50} values in the range of 4.67 to 10.0 µM (**Table 4.1**). Similar to the compounds from the nonchlorinated PTZ series (**5** and **7a**-**c**), the presence of methoxybenzoyl substituents enhanced AChE inhibition (**7j**-**l**) with compound **7k** (3-methoxybenzoyl) identified as the most potent compound (AChE IC_{50} = 4.67 µM) among the C-2 chloro-PTZ derivatives.

The SAR studies of PTZs on BuChE inhibition indicates that they were generally weak inhibitors and were less potent compared to their inhibitory potency towards AChE (**Table 4.1**). Among the nonchlorinated PTZs including **5** and **7a**-**f**, compound **5** exhibited superior inhibitory potency (BuChE IC_{50} = 5.80 µM) relative to AChE (IC_{50} = 7.37 µM) and was the most potent. It was approximately 11-fold more potent relative the reference agent galantamine (BuChE IC_{50} = 66.50 µM) and was less potent compared to both tacrine (BuChE IC_{50} = 0.04 µM) and donepezil (BuChE IC_{50} = 3.60 µM). Among the 2-Cl-PTZ derivatives **7g**-**l**, compound **7h** with a phenylacetyl substituent was identified as the most potent BuChE inhibitor (BuChE IC_{50} = 3.60 µM). In general, the presence of a 2-Cl substituent led to enhanced BuChE inhibition potency for *N*-acyl PTZ derivatives **7g**-**l** relative to the corresponding nonchlorinated *N*-acyl PTZ derivatives **7a**-**f**. Interestingly, the presence of either a ethylphenyl (**7i**) or 4-methoxybenzoyl (**7k**) *N*-acyl substituents provided similar BuChE inhibition (IC_{50} values of 5.0 and 5.30 µM respectively) whereas both 3-methoxyphenyl (**7j**) and 3,4-dimethoxyphenyl (**7l**) derivatives exhibited weak inhibition (IC_{50} values of 30.80 and 32.66 µM respectively). **Figure 4.2** highlights the effects of the chlorine on BuChE inhibition, with the general trend that adding C-2 chlorine led to enhanced BuChE potency.

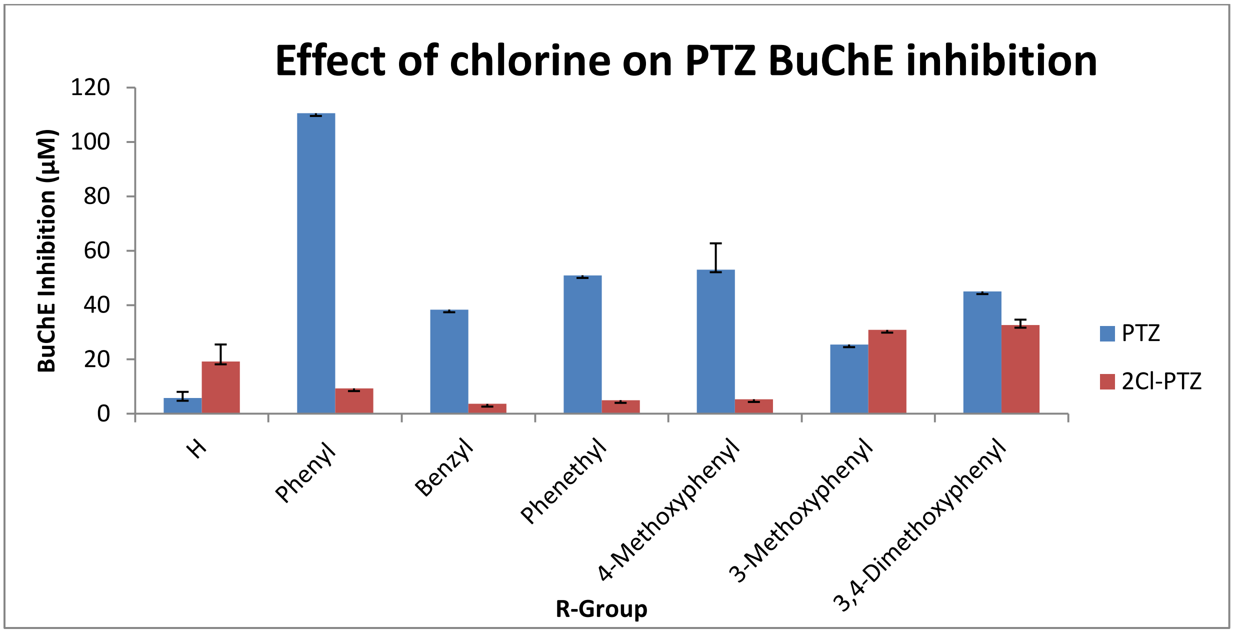

Figure 4.2: Graphical summary of chlorine's effect on BuChE inhibition of PTZ series. Results are expressed as average ± SD (n = 3) of two independent experiments. Error bars represent standard deviation

The cholinesterase SAR study for PTZ compound library, demonstrates that they exhibit dual inhibition of both AChE and BuChE enzymes. Their AChE inhibition ranged from 4.67-10.0 µM (IC_{50}s) whereas their BuChE inhibition ranged from 3.60-110.50 µM. Compounds exhibited nonselective inhibition of both the enzymes and generally exhibited superior AChE inhibition potency. These studies show that PTZ derivatives serve as useful ring scaffolds to design dual cholinesterase inhibitors.

Table 4.1: Cholinesterase inhibition data, Selectivity Index and ClogP values of PTZ series

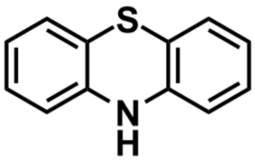

(5)

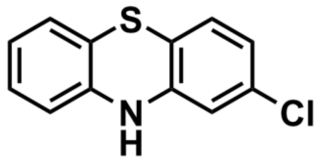

(6)

X = H, Cl
(7a-f), (7g-l)

Compd	R	IC_{50} (μM)[a] AChE	BuChE	Selectivity Index (SI)[b]	ClogP[c]
5	-	7.37	5.80	1.27	3.56
7a	Phenyl	8.07	110.52	0.07	5.23
7b	Benzyl	7.41	38.35	0.19	3.87
7c	Phenethyl	7.14	51.00	0.14	4.20
7d	4-Methoxyphenyl	6.31	53.06	0.12	5.45
7e	3-Methoxyphenyl	6.23	25.50	0.24	5.45
7f	3,4-Dimethoxyphenyl	5.81	45.02	0.13	4.59
6	-	7.39	19.19	0.39	4.59
7g	Phenyl	9.97	9.34	0.52	6.00
7h	Benzyl	7.51	3.64	2.06	4.64
7i	Phenethyl	7.92	5.02	1.58	4.97
7j	4-Methoxyphenyl	5.89	5.35	1.10	6.22
7k	3-Methoxyphenyl	4.67	30.84	0.15	6.22
7l	3,4-Dimethoxyphenyl	6.41	32.65	0.20	5.90

Tacrine	-	0.16	0.04	4.00	2.27
Donepezil	-	0.04	3.60	0.01	4.60
Galantamine	-	2.59	66.50	0.04	1.02

[a]IC_{50} values are average of two to three independent experiments (n = 3) with deviation <10% of mean value. [b]SI = *h*BuChE/*h*AChE IC_{50}. [c]ClogP was determined using ChemDraw Ultra version 11.0 Cambridge Software Company.

4.3.2 PSZ Derivatives SAR

The unsubstituted PSZ's (**13** and **14**) and its derivatives **15a-l**, were evaluated for their ability to inhibit both human AChE and BuChE enzymes. Their activity was compared to known cholinesterase inhibitors tacrine, donepezil, galantamine and ebselen (**Table 4.2**). The unsubstituted PSZ derivative **13** exhibited an IC_{50} value of 5.63 µM towards human AChE and was less potent compared to reference agents tacrine (AChE IC_{50} = 0.16 µM), donepezil (AChE IC_{50} = 0.04 µM) and galantamine (AChE IC_{50} = 2.60 µM). However, it showed greater potency than the organoselenium compound ebselen (AChE IC_{50} = 6.24 µM). Addition of an *N*-benzoyl substituent in compound **15a** retained AChE inhibition (IC_{50} = 5.43 µM) and the compound was more potent compared to **13**. Again, the effect of aromatic acyl groups with one (benzyl) and two carbon spacer (phenethyl) on AChE inhibition were explored (compounds **15b** and **15c**). These modification provided AChE inhibition and both compounds **15b** (AChE IC_{50} = 6.41 µM) and **15c** (AChE IC_{50} = 6.76 µM) exhibited less potency as compared to **13** (AChE IC_{50} = 5.63 µM). The effect of methoxyphenyl substituents was explored by evaluating compounds **15d-f** (Table 4.2). Interestingly, these compounds exhibited AChE inhibition ranging from 4.62 to 6.25 µM

(IC_{50}) and were more potent compared to compounds **13** and **15a-c** with the exception of **15k** (AChE IC_{50} = 6.25 µM). The 4-dimethoxyphenyl compound (**15d**) was identified as the most potent AChE inhibitor (IC_{50} = 4.63 µM). Furthermore, the addition of C-2 chlorine to the PSZ scaffold was investigated. Similar to the PTZ series, the C-2 chlorine substituent was not a major factor in AChE inhibition and C-2 chloro-PSZ derivatives **15g-l** exhibited IC_{50} values in the range of 5.79 to 6.58 µM (**Table 4.2**). Similar to the compounds from the nonchlorinated PSZ series (**13** and **15a-c**), the presence of methoxyphenyl substituents enhanced AChE inhibition (**15j-l**) with compound **15j** (4-methoxyphenyl) identified as the most potent compound (AChE IC_{50} = 5.79 µM) among the C-2 chloro-PTZ derivatives.

The SAR studies of PSZs on BuChE inhibition indicates that they were generally weak inhibitors and were less potent compared to their inhibitory potency towards AChE (**Table 4.2**). Among the nonchlorinated PSZs including **13** and **15a-f**, compound **13** exhibited superior inhibitory potency (BuChE IC_{50} = 3.00 µM) relative to AChE (IC_{50} = 5.63 µM) and was the most potent. It was approximately 22-fold more potent relative the reference agent galantamine (BuChE IC_{50} = 66.50 µM), more potent than donepezil (BuChE IC_{50} = 3.6 µM) and ebselen (BuChE IC_{50} = 4.65 µM) and was less potent compared to both tacrine (BuChE IC_{50} = 0.04 µM). Among the 2-Cl-PTZ derivatives **15g-l**, compound **15g** with a benzoyl substituent was identified as the most potent BuChE inhibitor (BuChE IC_{50} = 3.88 µM). In general, the presence of a 2-Cl substituent led to enhanced BuChE inhibition potency for *N*-acyl PSZ derivatives **15g-l** relative to the corresponding nonchlorinated *N*-acyl PSZ derivatives **15a-f**, with the exception of the 3-methoxyphenyl compound (**15k**) which gave a 2-fold decrease in potency (BuChE IC_{50} = 19.30 µM). Interestingly, the presence of either a 4-methoxybenzoyl (**15j**) or and 3,4-dimethoxybenzoyl (**15l**) *N*-acyl substituents provided similar BuChE inhibition (IC_{50} values of

4.91 and 5.75 µM respectively) whereas both 3-methoxyphenyl (**15k**) and phenethyl (**15i**) derivatives exhibited weak inhibition (IC_{50} values of 40.00 and 19.30 µM respectively). **Figure 4.3** highlights the effects of the chlorine on BuChE inhibition, with the general trend that adding the chlorine led to enhanced BuChE potency similar to the PTZ series.

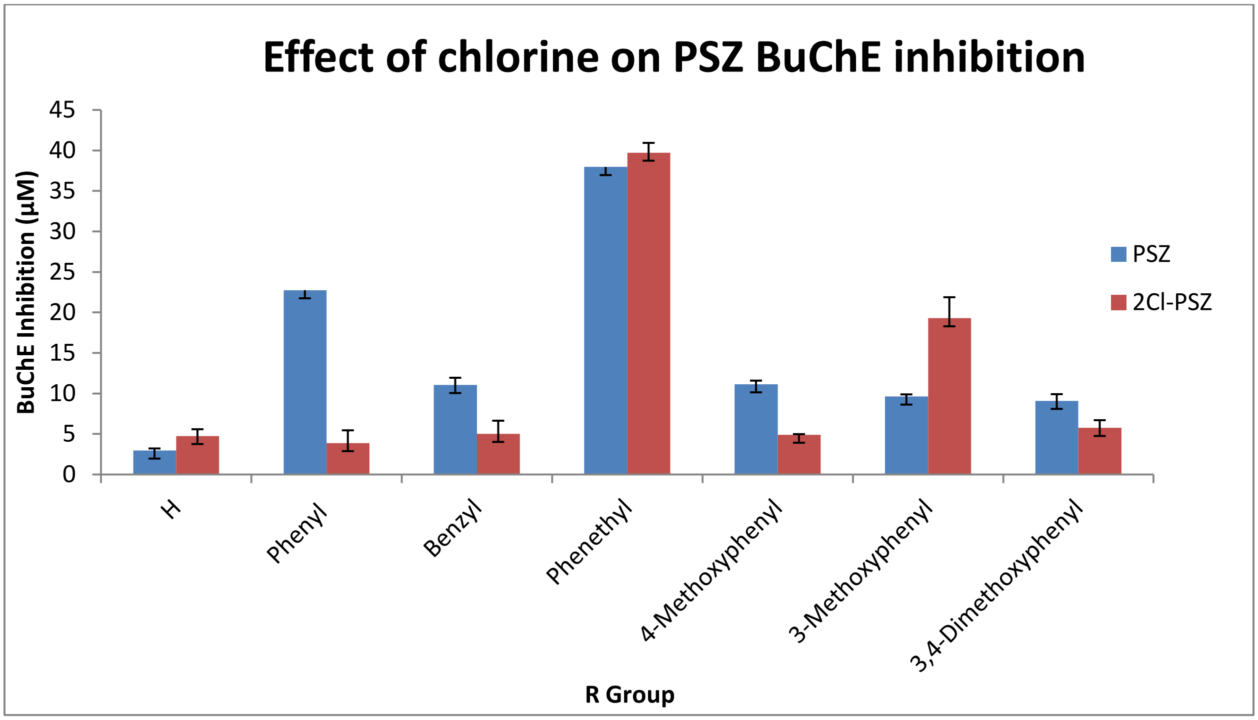

Figure 4.3: Graphical summary of chlorine's effect on BuChE inhibition of PSZ series. Results are expressed as average ± SD (n = 3) of two independent experiments. Error bars represent standard deviation

The cholinesterase SAR study for PSZ compound library, demonstrates that they exhibit dual inhibition of both AChE and BuChE enzymes. Their AChE inhibition ranged from 4.63-6.76 µM (IC_{50}s) whereas their BuChE inhibition ranged from 3.88-39.73 µM. Similar to that of the PTZ series, the PSZ series exhibited nonselective inhibition of both the enzymes and generally exhibited superior AChE inhibition potency. These studies show that PSZ derivatives serve as useful ring scaffolds to design dual cholinesterase inhibitors.

Table 4.2: Cholinesterase inhibition data, Selectivity Index and ClogP values of PSZ series

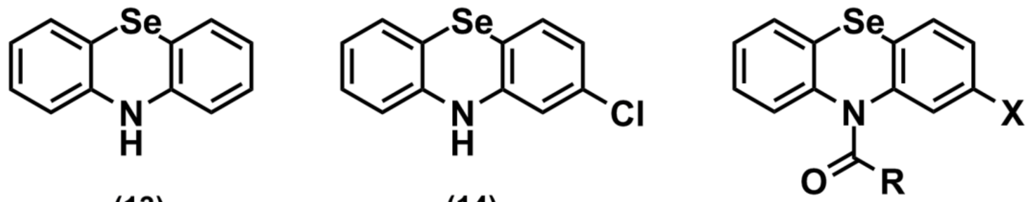

(13) (14) X = H, Cl (15a-f), (15g-l)

Compd	R	IC_{50} (µM)[a] AChE	IC_{50} (µM)[a] BuChE	Selectivity Index (SI)[b]	ClogP[c]
13	-	5.63	3.00	1.90	4.36
15a	Phenyl	5.43	22.75	0.24	6.03
15b	Benzyl	6.41	11.05	0.58	4.67
15c	Phenethyl	6.76	38.00	0.18	5.00
15d	4-Methoxyphenyl	4.63	11.14	0.42	6.25
15e	3-Methoxyphenyl	6.25	9.63	0.65	6.25
15f	3,4-Dimethoxyphenyl	5.10	9.09	0.56	5.93
14	-	6.34	4.75	1.33	5.37
15g	Phenyl	6.04	3.88	1.56	6.74
15h	Benzyl	6.58	5.02	1.31	5.38
15i	Phenethyl	6.29	40.00	0.16	5.72
15j	4-Methoxyphenyl	5.79	4.91	1.18	6.96
15k	3-Methoxyphenyl	5.92	19.30	0.03	6.96
15l	3,4-Dimethoxyphenyl	6.18	5.75	1.07	6.64

Tacrine	-	0.16	0.04	4.00	2.27
Donepezil	-	0.04	3.60	0.01	4.60
Galantamine	-	2.59	66.47	0.04	1.02
Ebselen	-	6.24	4.65	1.34	3.70

[a]IC_{50} values are average of two to three independent experiments (n = 3) with deviation <10% of mean value. [b]SI = *h*BuChE/*h*AChE IC_{50}. [c]ClogP was determined using ChemDraw Ultra version 11.0 Cambridge Software Company.

4.4 Conclusion

Both the PTZ and PSZ scaffolds serve as viable core templates as dual cholinesterase inhibitors. Among the PTZ derivatives, compound **7k** was indentified as the most potent AChE inhibitor (AChE IC_{50} = 4.67 μM); compound ; compound **7j** as the best dual ChE inhibitor (AChE IC_{50} = 5.89 μM, BuChE IC_{50} = 5.35 μM); and compound **7h** as the best BuChE inhibitor (BuChE IC_{50} = 3.64 μM). This indicates that N-acylation enhances ChE inhibition compared to the unsubstituted PTZ's **5** and **6**. Among the PSZ derivatives, compound **15d** was identified as the most potent AChE inhibitor (AChE IC_{50} = 4.63 μM); compound **15g** as the best dual ChE inhibitor (AChE IC_{50} = 5.79 μM, BuChE IC_{50} = 4.91 μM); and compound **13** as the best BuChE inhibitor (BuChE IC_{50} = 3.88 μM). This indicates that N-acylation enhances ChE inhibition compared to the unsubstituted PSZ's **13** and **14**. The electronic effect of adding a chlorine at the 2-position of the PTZ and PSZ scaffold helped increase its potency towards BuChE greatly without loss of AChE activity. The best compounds are highlighted below in **Figures 4.4** and **4.5**.

(7k) - AChEI
AChE IC_{50} = 4.67 μM
BuChE IC_{50} = 30.84 μM

(7j) - Dual ChEI
AChE IC_{50} = 5.89 μM
BuChE IC_{50} = 5.35 μM

(7h) - BuChEI
AChE IC_{50} = 7.51 μM
BuChE IC_{50} = 3.64 μM

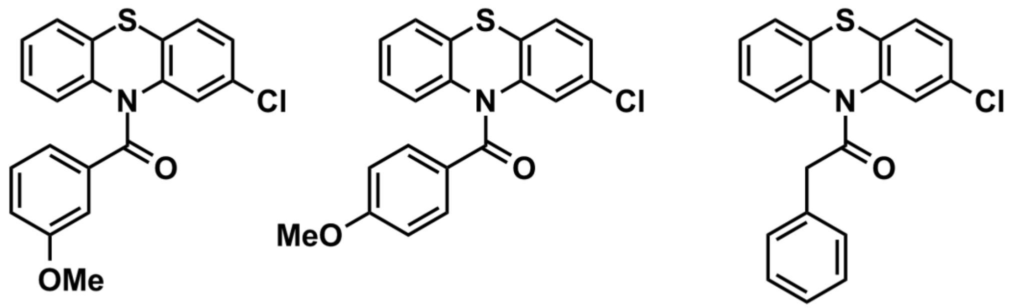

(2-chloro-10*H*-phenothiazin-10-yl)(3-methoxyphenyl)methanone

(2-chloro-10*H*-phenothiazin-10-yl)(4-methoxyphenyl)methanone

1-(2-chloro-10*H*-phenothiazin-10-yl)-2-phenylethanone

Figure 4.4: Top candidates from the PTZ series from cholinesterase inhibition

(15d) - AChEI
AChE IC_{50} = 4.63 μM
BuChE IC_{50} = 11.14 μM

(15j) - Dual ChEI
AChE IC_{50} = 5.79 μM
BuChE IC_{50} = 4.91 μM

(13) - BuChEI
AChE IC_{50} = 5.63 μM
BuChE IC_{50} = 3.00 μM

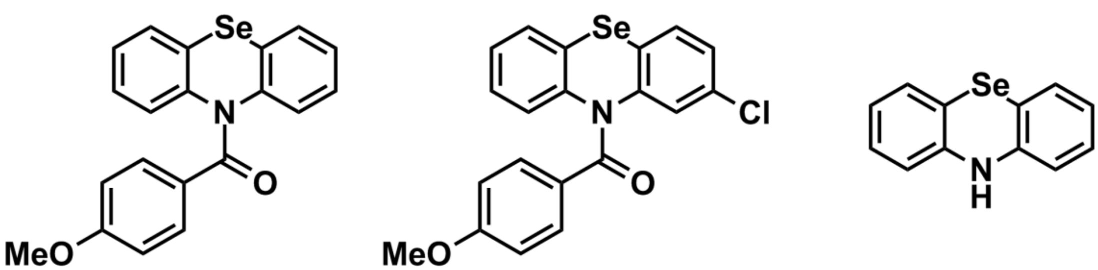

(4-methoxyphenyl)(10*H*-phenoselenazin-10-yl)methanone

(2-chloro-10*H*-phenoselenazin-10-yl)(4-methoxyphenyl)methanone

10*H*-phenoselenazine

Figure 4.5: Top candidates from the PSZ series from cholinesterase inhibition

4.5 Amyloid Aggregation Inhibition Studies

4.5.1 Assay Principle

The Aβ aggregation assay is based on the biophysical properties that amyloid (Aβ) peptides exhibit. Thioflavin T (ThT), a fluorescent dye was used. Its fluorescence is monitored, and the change in fluorescence is detected when ThT is bound within the cross β-sheet formation (**Figure 4.6**). Normally ThT exhibits fluorescence at 446 nm but when bound to the rigid structures of Aβ there is a characteristic red shift, at 490 nm. From the compound screening, the relative fluorescence units (RFU) are monitored over a 16 hour period.[124] The compounds with anti-amyloid aggregation properties promote more free unbound ThT, and this is indicated by the lower RFU values at 490 nm ThT emission wavelength.

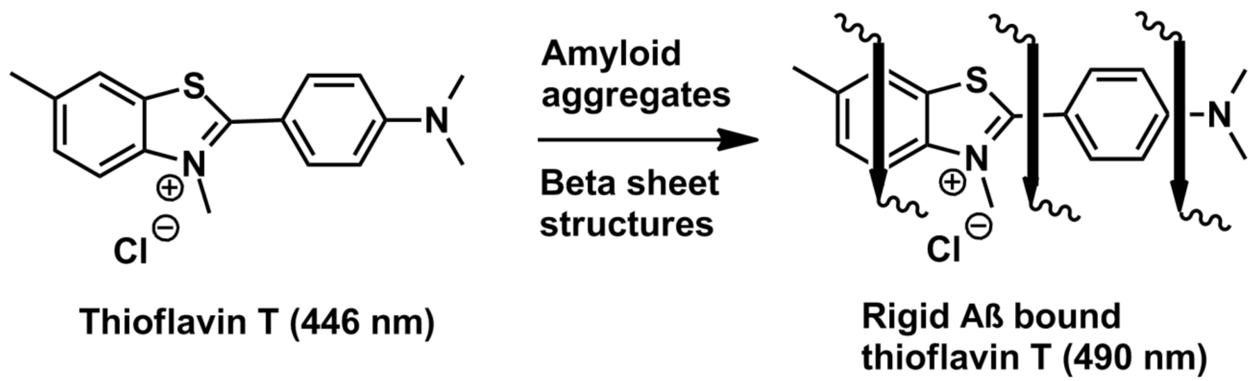

Figure 4.6: Anti-amyloid aggregation assay principle

4.6 Results and Discussion

4.6.1 PTZ Derivatives SAR

The unsubstituted PTZ's (**5** and **6**) and their 3,4-dimethoxybenzoyl derivative (**7f**) was evaluated for their ability to inhibit self-induced $A\beta_{1-42}$ aggregation at four different concentrations (1, 5, 10 and 25 µM). Their activity was compared to known aggregation inhibitor, orange G (**Table 4.3**). The unsubstituted PTZ (**5**) exhibited superior anti-aggregation activity compared to reference orange G at all concentrations. **7f** was also screened, but showed weak anti-aggregation potency (< 4% aggregation inhibition at all concentrations). Similarly, the 2-chloro analogs **6**, and **7l** were also screened and the unsubstitued 2-chloroPTZ (**6**) showed a lower degree of anti-aggregation property at 1, 5, and 10 µM compared to **5**. At 25 µM both **5** and **6** exhibited similar anti-aggregation properties. (61.9 and 60.8% aggregation inhibition respectively). Compound **6** exhibited comparable anti-aggregation activity to control orange G, showing similar percent inhibition across each concentration. The chlorinated 3,4-dimethoxybenzoyl compound (**7l**) again showed poor inhibition values at each concentration of 1, 5, 10 and 25 µM (6.2, 4.5, 6.5, 5.9% aggregation inhibition respectively) indicating that the activity was independent of concentration. It appears that for PTZ derivaties, N-acylation was detrimental to anti-aggregation activity with both the unsubstituted compounds **5** and **6** exhibiting superior anti-aggregation properties. Figure 4.7 shows the aggregation kinetics of compound **5**. In the absence of compound **5**, a typical Aβ aggregation curve is seen (100% control) with an initial lag phase that corresponds to nucleation dependent aggregation, followed by a rapid growth phase and a saturation phase corresponding to Aβ fibril formation. Increasing the concentration of compound **5** was clearly able to reduce the formation of Aβ fibrils by affecting the growth and saturation phase.

Table 4.3: Self-induced amyloid ($A\beta_{1-42}$) inhibition data for PTZ derivatives

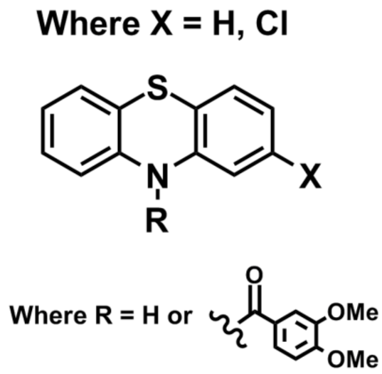

5, 6, 7f, 7l

Compd	**R**	**X**	**% Inhibition at:**[a]			
			1 µM	**5 µM**	**10 µM**	**25 µM**
5	H	H	18.3	37.2	59.1	61.9
7f	3,4-Dimethoxybenzoyl	H	NA	NA	NA	NA
6	H	Cl	10.3	22.0	33.7	60.8
7l	3,4-Dimethoxybenzoyl	Cl	6.2	4.5	6.5	5.9
Orange G	-	-	8.6	20.4	31.0	57.2

[a]Percent aggregation inhibition values are average ± s.d < 10% (n = 3) for two independent experiments. NA = not active, % inhibition < 4%

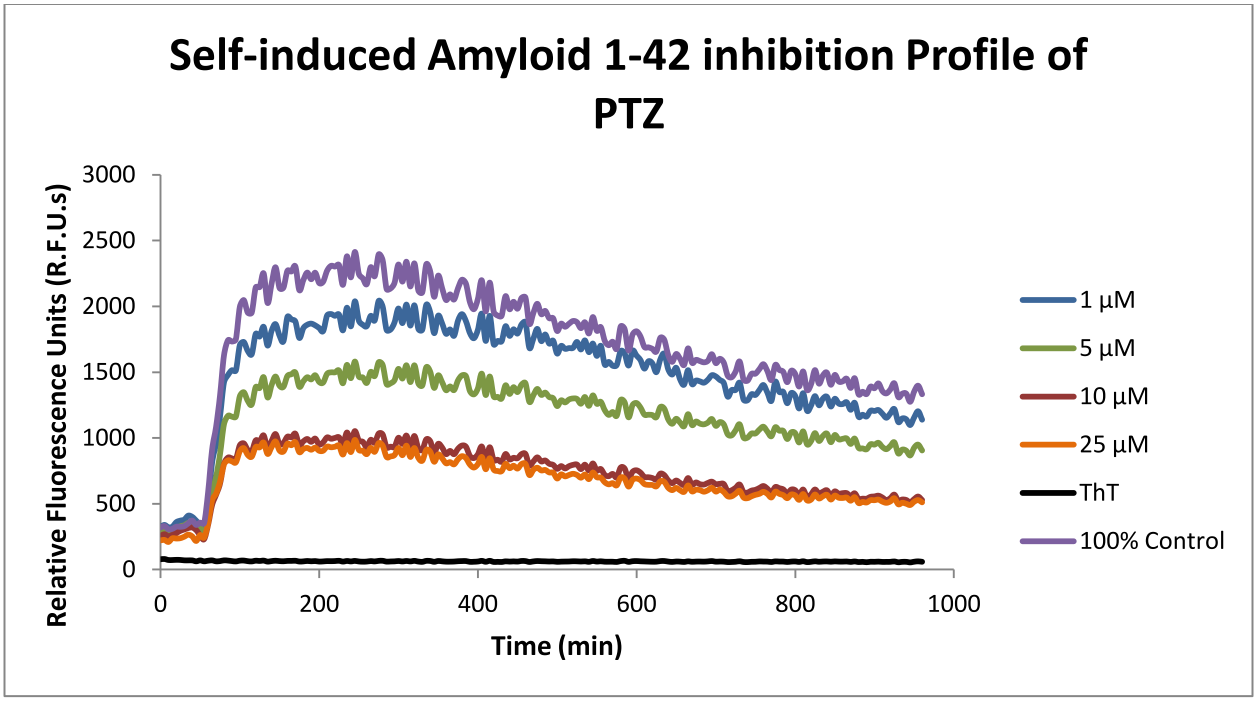

Figure 4.7: Aβ_{1-42} aggregation kinetic data for compounds **5** at 37 °C, 16 hr incubation in sodium phosphate buffer at pH 8.5

4.6.2 PSZ Derivatives SAR

The unsubstituted PSZ's (**13** and **14**) and its 3,4-dimethoxybenzoyl derivative (**15f**) was evaluated for their ability to inhibit self-induced Aβ_{1-42} aggregation at four different concentrations (1, 5, 10 and 25 µM). Their activity was compared to known aggregation inhibitor, orange G (**Table 4.4**). At the lower concentrations of 1 and 5 µM, the unsubstituted PSZ (**13**) (16.3 and 24.1% aggregation inhibition respectively) exhibited superior anti-aggregation activity compared to reference orange G (8.6 and 20.4% aggregation inhibition respectively). However, it was less potent at 25 µM (45.55%, **13** vs 57.24%, orange G). **15f** was also screened and showed a 3-4 fold decrease in anti-aggregation potency compared to **13** at each concentration. Similarly, the 2-chloro analogs **14**, and **15l** were also screened. The unsubstitued 2-chloroPSZ (**14**) showed similar anti-aggregation activity relative to **13** at all concentrations (Table 4.4). At 1 µM **14**

(14.50% aggregation inhibition) exhibited greater anti-aggregation activity compared to orange G (8.63% aggregation inhibition), but showed decreased activity at higher concentrations. The chlorinated 3,4-dimethoxybenzoyl compound (**15l**) version showed poor inhibition values at each concentration of 1, 5, 10 and 25 µM (8.4, 7.9, 9.1, 5.9% aggregation inhibition respectively). The most potent anti-aggregation compound was the unsubstituted PSZ (**13**), showing that N-acylation was detrimental to anti-aggregation activity. The aggregation kinetic profile for **13** (Figure 4.8) shows that it was able to decrease Aβ fibril formation with increasing concentration. It affected both the growth and saturation phase of Aβ fibril formation similar to the PTZ bioisostere **5**.

Table 4.4: Self-induced amyloid ($A\beta_{1\text{-}42}$) inhibition data for PSZ derivatives

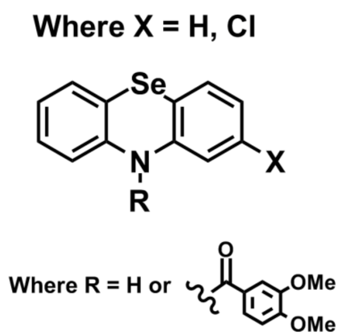

13, 14, 15f, 15l

Compd	**R**	**X**	**% Inhibition at:[a]**			
			1 µM	**5 µM**	**10 µM**	**25 µM**
13	H	H	16.3	24.1	30.7	45.6
15f	3,4-Dimethoxybenzoyl	H	6.3	5.7	8.7	11.1
14	H	Cl	14.5	18.5	25.1	45.0

15l	3,4-Dimethoxybenzoyl	Cl	8.4	7.9	9.1	5.9
Orange G	-	-	8.6	20.4	31.0	57.2

[a]Percent aggregation inhibition Values are average ± s.d < 10% (n = 3) for two independent experiments.

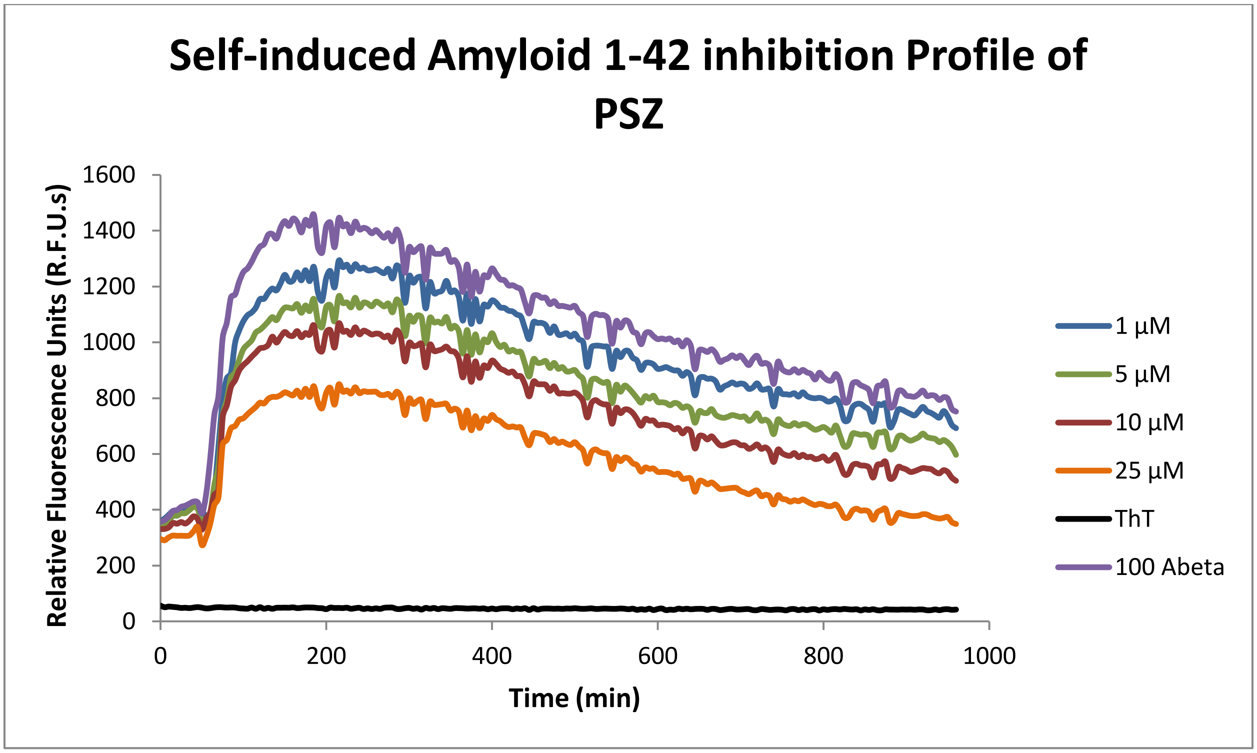

Figure 4.8: $A\beta_{1-42}$ aggregation kinetic data for compounds **13** and at 37 °C, 16 hr incubation sodium phosphate buffer at pH 8.5

4.7 Conclusion

The non-acylated PTZ (**5**) and PSZ (**13**) compounds exhibited good anti-aggregation properties compared to N-acylated derivatives. The addition of the 3,4-dimethoxybenzoyl substituent to both un-chlorinated and chlorinated derivatives led to poor anti-aggregation properties. The unsubstituted PTZ (**5**) showed superior inhibition compared to other compounds screened including the reference agent, orange G.

(5) - PTZ
% inhibition at 25 μM = 61.9%

(13) - PSZ
% inhibition at 25 μM = 45.6%

10*H*-phenothiazine

10*H*-phenoselenazine

Figure 4.9: Chemical structures of top compounds with anti-A$\beta_{1\text{-}42}$ aggregation activity

4.8 Antioxidant Assay

4.8.1 Assay Principle

The anti-oxidant assay measures the compounds ability to scavenge free radicals. The 2,2-diphenyl-1-picrylhydrazyl radical (•DPPH) is a well-known standard used to measure antioxidant properties. It acts as a stable free radical due to the electron delocalization around the molecule, which exhibits a deep purple solution and strong absorption at 517 nm. When it gets neutralized with an anti-oxidant source, the solution becomes a pale yellow (**Figure 4.10**). The monitoring of the change in absorbance at 517 nm allows for measurement of antioxidant activity.[125]

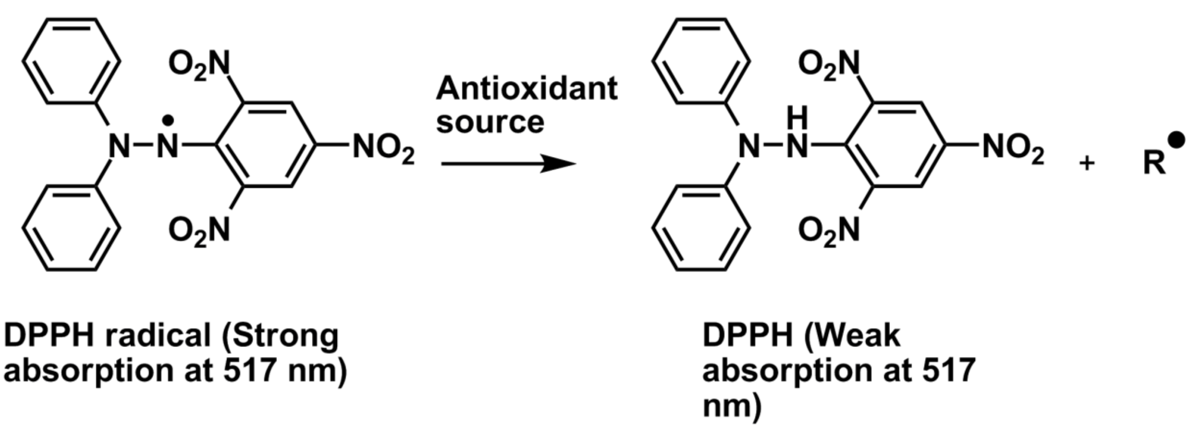

Figure 4.10: DPPH radical scavenging assay principle

4.9 Results and Discussion

4.9.1 PTZ Derivatives SAR

The antioxidant properties of some representative compounds from the PTZ library was evaluated using DPPH assay and the results were compared with reference agent ebselen and trolox (**Table 4.5**). The basic PTZ template (**5**) exhibited potent antioxidant activity at 50 µM (92% inhibition) and its antioxidant activity was similar to trolox (96% inhibition). The addition of a C-2 chloro substituent in **6** reduced the antioxidant property (76% inhibition). Interestingly, acylation of the PTZ *N*-10 led to a dramatic decline in their ability to scavenge DPPH radical. For example both compounds **7f** and **7l** with 3,4-dimethoxybenzoyl *N*-acyl substituents exhibited 44 and 46% inhibition at 50 µM (**Table 4.6**) and were less potent compared to the non-acylated compounds **5** and **6**. These results indicate that the presence of a free NH group plays an important role in DPPH scavenging ability. Nevertheless *N*-acylation did not abolish antioxidant properties altogether and compounds **7f** and **7l** did retain antioxidant properties which indicates that *N*-acylated PTZ derivatives can be considered as suitable systems to design multifunctional agents to target the oxidative stress hypothesis of AD pathophysiology.

Table 4.5: DPPH radical scavenging by PTZ derivatives

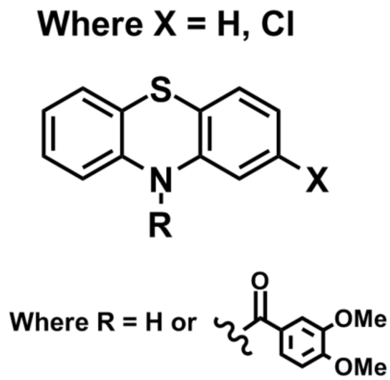

5, 6, 7f, 7l

Compd	**R**	**X**	**% Inhibition at 50 µM[a]**
5	H	H	92.1
7f	3,4-Dimethoxybenzoyl	H	44.3
6	H	Cl	76.4
7l	3,4-Dimethoxybenzoyl	Cl	46.5
Trolox	-	-	99.2

[a]Percent inhibition values are average of two independent experiments (n = 3) with deviation <10% of mean value.

4.9.2 PSZ Derivatives SAR

The ability of PSZs to scavenge DPPH radical was evaluated. Unsubstituted PSZ (**13**), 2-Cl-PSZ (**14**) and *N*-acyl PSZ derivatives (**15f** and **15l**) were evaluated (**Table 4.6**). The trend obtained was similar to PTZ series. PSZs with a free NH group exhibited potent antioxidant activity (compound **13**, 84% inhibition and compound **14**, 73% inhibition at 50 µM). Both compounds were much more potent compared to the selenium containing reference agent ebselen (33% inhibition) although were less potent compared to trolox (96% inhibition). The presence of an electron withdrawing C-2 chlorine group in compound **14**, reduced its ability to scavenge DPPH radical compared to the non-chlorinated PSZ compound **13**. The *N*-acylated PSZ derivatives with a 3,4-dimethoxybenzoyl substituents (compound **15f** and **15l**) exhibited reduced activity (39 and 38% inhibition respectively) with almost 2.2-fold reduction in their ability to scavenge DPPH radical relative to the non-acylated compound **13** (84% inhibition). These studies indicate that *N*-acyl PSZ derivatives exhibit antioxidant properties and represent a useful template in the design of multi-targeting agents with antioxidant properties to treat AD.

Table 4.6: DPPH radical scavenging by PSZ derivatives

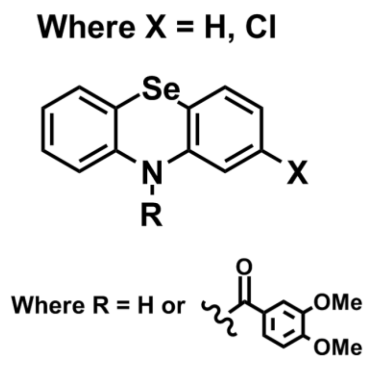

13, 14, 15f, 15l

Compd	**R**	**X**	**% Inhibition at 50 µM[a]**
13	H	H	84.4
15f	3,4-Dimethoxybenzoyl	H	39.0

14	H	Cl	73.2
15l	3,4-Dimethoxybenzoyl	Cl	38.3
Trolox	-	-	99.2
Ebselen	-	-	34.7

[a]Percent inhibition values are average of two independent experiments (n = 3) with deviation <10% of mean value.

4.10 Conclusion

The DPPH based antioxidant screen for PTZ and PSZ compounds demonstrates that both class of tricyclics exhibit antioxidant properties. The study also shows that the presence of a free amine (*N*-10) provides excellent antioxidant properties whereas *N*-acyl substitution can lead to a reduction in their DPPH scavenging ability. This could be due to the fact that non-acylated PTZ and PSZ's with a free NH group could be more efficient scavengers of DPPH radicals due to the formation of a resonance stabilized radical (**Figure 4.11**) whereas *N*-acylation might compromise this stability leading to a reduction in the antioxidant properties. It should be noted that selenium metal itself is known to exhibit antioxidant properties suggesting that in vivo metabolites of PSZ derivatives have the potential to exhibit antioxidant properties.[112, 113] These studies show that both PTZ and PSZ derivatives exhibit antioxidant properties and could serve as bioisosteres in the design of novel tricyclics as potential disease modifying agents to treat AD. The two best antioxidant compounds are highlighted in **Figure 4.12**.

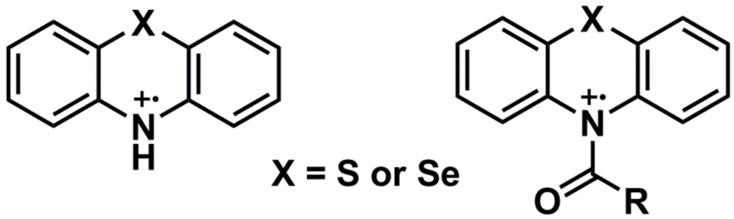

Figure 4.11 Mechanism of PTZ and PSZ based antioxidants

(5) - PTZ
% inhibition at 50 μM = 92.1%

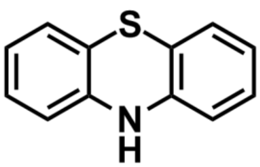

10*H*-phenothiazine

(13) - PSZ
% inhibition at 50 μM = 84.4%

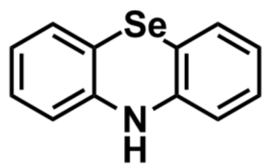

10*H*-phenoselenazine

Figure 4.12: Chemical structures of top PTZ and PSZs with antioxidant properties

4.11 Evaluation of Cell Viability

4.11.1 Assay Principle

The cell viability assay for some PTZ and PSZ derivatives were carried out to evaluate their toxicity. By using 3-(4,5-dimethylthiazol-2-yl)-2,5-diphenyltetrazolium bromide (MTT) and the activity of the mitochondrial reductase in metabolically active cells, the cytotoxic effects of test compounds can be quantified.[126] MTT is a yellow tetrazole that is reduced to a purple formazan in living cells (**Figure 4.13**). The monitoring of the absorbance of the formazan at 570 nm allows for the measurement of cell viability. Compounds with reduced cytotoxicity do not affect formazan reduction by living cells.

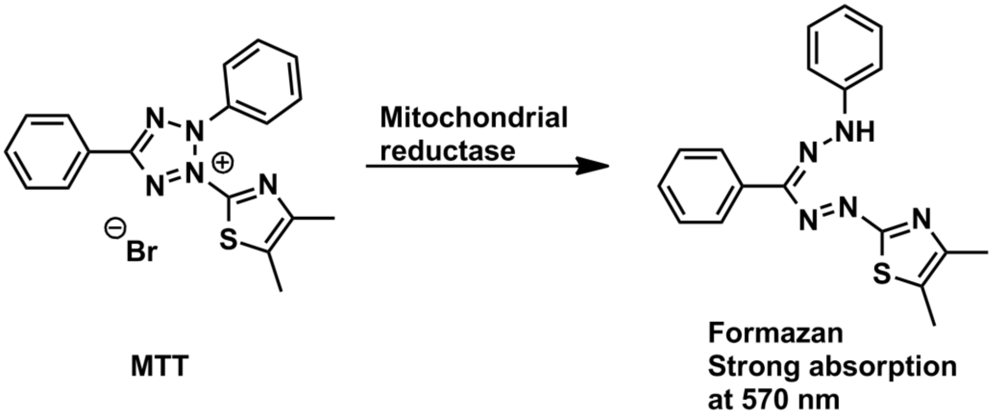

Figure 4.13: MTT based cell viability assay principle

4.12 Results and Discussion

4.12.1 PTZ Derivatives

The unsubstituted PTZ's (**5** and **6**) and its 3,4-dimethoxy derivatives (**7f** and **15f**) were evaluated for their viability towards the SH-SY5Y neuroblastoma cell line at 50 µM (**Table 4.7**). The unsubstituted PTZ (**5**) (63.72% cell viability) exhibited moderate to good tolerance by the neuroblastoma cells. The **7f** derivative was also screened and showed similar tolerance. (64.4% cell viability) Similarly, the 2-chloro analogs **6**, and **7l** were also screened. The unsubstitued 2-chloroPTZ (**6**) (64.0% cell viability) showed comparable values to both **5** and **7l**. Interestingly, the 3,4-dimethoxybenzoyl group in the chlorinated (**7l**) version was identified as a PTZ derivative with good cell viabilty (71.6% cell viability).

Table 4.7: Percent viability of SH-SY5Y cell line after treatment with PTZs

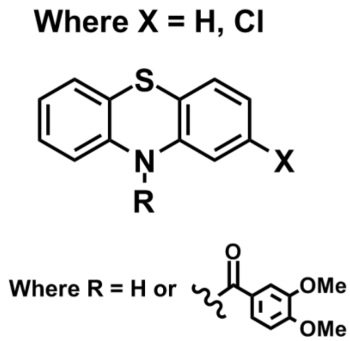

5, 6, 7f, 7l

Compd	**R**	**X**	**% Cell viability at 50 µM[a]**
5	H	H	63.7
7f	3,4-Dimethoxybenzoyl	H	64.4
6	H	Cl	64.0
7l	3,4-Dimethoxybenzoyl	Cl	71.6

[a]Percent inhibition values are average of two independent experiments (n = 3) with deviation <10% of mean value.

4.12.2 PSZ Derivatives

The unsubstituted PSZ (**13** and **14**) and its 3,4-dimethoxy derivatives (**15f** and **15l**) was evaluated for their viability towards the SH-SY5Y neuroblastoma cell line at 50 µM. Their activity was compared to known organoselenium compound, ebselen. (**Table 4.8**) The unsubstituted PSZ (**13**) (76% cell viability) exhibited better tolerance compared to ebselen (59.3% cell viability). The

15f derivative was also screened and showed an even higher tolerance. (93.69% cell viability) The 2-chloro analogs **14**, and **15l** were also screened. The unsubstitued 2-chloroPSZ (**14**) (43.0% cell viability) showed a decrease in cell viability. Interestingly, the chlorinated 3,4-dimethoxybenzoyl compound (**15l**) exhibited the best tolerance (100% cell viability).

Table 4.8: Percent viability of SH-SY5Y cell line after treatment with PSZs

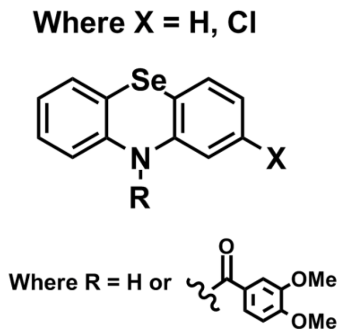

13, 14, 15f, 15l

Compd	**R**	**X**	**% Cell viability at 50 μM[a]**
13	H	H	76.0
15f	3,4-Dimethoxybenzoyl	H	93.7
14	H	Cl	43.0
15l	3,4-Dimethoxybenzoyl	Cl	100
Ebselen	-	-	59.3

[a]Percent inhibition values are average of two independent experiments (n = 3) with deviation <10% of mean value.

4.13 Conclusion

The MTT cell viability assay performed on the PTZ and PSZ series demonstrated moderate to good cell viability at 50 µM in SH-SY5Y neuroblastoma cell line. The PTZ series showed moderate cell viability (63.7-71.6% cell viability). In the PSZ series, the unsubstituted derivates showed similar results to the PTZ derivates (43.0-76.0% cell viability). Interestingly, the addition of the 3,4-dimethoxybenzoyl group demonstrated an increase the compounds' viability (93.7-100% cell viability), and demonstrated superior viability to control ebselen as well.

(**7l**) - % cell viability at 50 µM = 76.1%

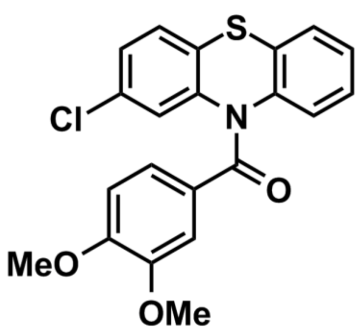

(2-chloro-10*H*-phenothiazin-10-yl)(3,4-dimethoxyphenyl)methanone

(**15l**) - % cell viability at 50 µM = 100%

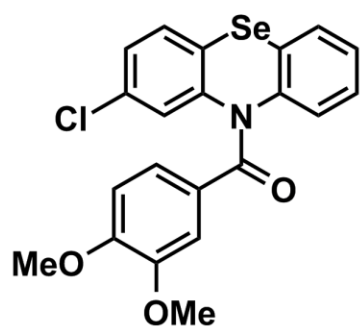

(2-chloro-10*H*-phenoselenazin-10-yl)(3,4-dimethoxyphenyl)methanone

Figure 4.14: Chemical structures of top PTZ and PSZ with good cell viability

Chapter 5: Molecular Docking Studies

5.1 Introduction

This chapter describes the investigation of the binding interactions of promising PTZ and PSZ derivatives with human AChE and BuChE enzymes. The x-ray coordinates of cholinesterase enzymes were obtained from protein data bank (pdb ID: 4EY7 and 1POI, respectively), PTZ and PSZ ligands were built using computational software and docked enzyme-ligand complex were ranked using in-built scoring function to identify key interactions responsible for cholinesterase inhibition. In addition, the ability of some PTZ and PSZs to prevent amyloid aggregation was investigated by docking studies using an amyloid dimer assembly as a model (pdb ID: 2LMN).

5.2 Principle

Two methods are employed in the molecular modeling studies of the PTZ's and PSZ's; LibDock and CDocker both of which are used for molecular docking The LibDock protocol was developed by Diller and Merz.[127] This method employs the use of protein site features referred to as HotSpots. HotSpots are classified into two types: polar and apolar or nonpolar. The LibDock method matches each specified ligand with the characterized receptor to generate different poses that are ranked based on the type of contact observed (polar/apolar) and ligand-receptor complex energy.

CDocker is a refined docking protocol developed by Wu et al.[128] Unlike Libdock, CDocker employs a grid-based molecular docking method that utilizes CHARMm. While the receptor is held rigid, the ligands docked are allowed to be flexible during the docking process. Through iterative steps the ligand poses are then optimized by grid-based simulated annealing to generate the top hits. The ligand poses obtained are ranked based on polar and nonpolar contacts as well as ligand-receptor complex energy. The LibDock protocol is useful to conduct rapid screening of compound libraries to determine potential binding modes with the target receptor whereas CDocker provides refined models to assist SAR optimization.

Both LibDock and CDocker programs were used to determine the potential binding modes and interactions of select PTZ and PSZs with human AChE, BuChE and Aβ-dimer assembly. Discovery Studio Structure-Based-Design software package from BIOVIA/Accelrys Inc. was used. The results were validated by conducting molecular docking studies of known cholinesterase inhibitor tacrine by comparing with its solved crystal structure. **Figure 5.1** gives a summary chart on the application of molecular docking in conjunction with compound library synthesis and biological evaluation.

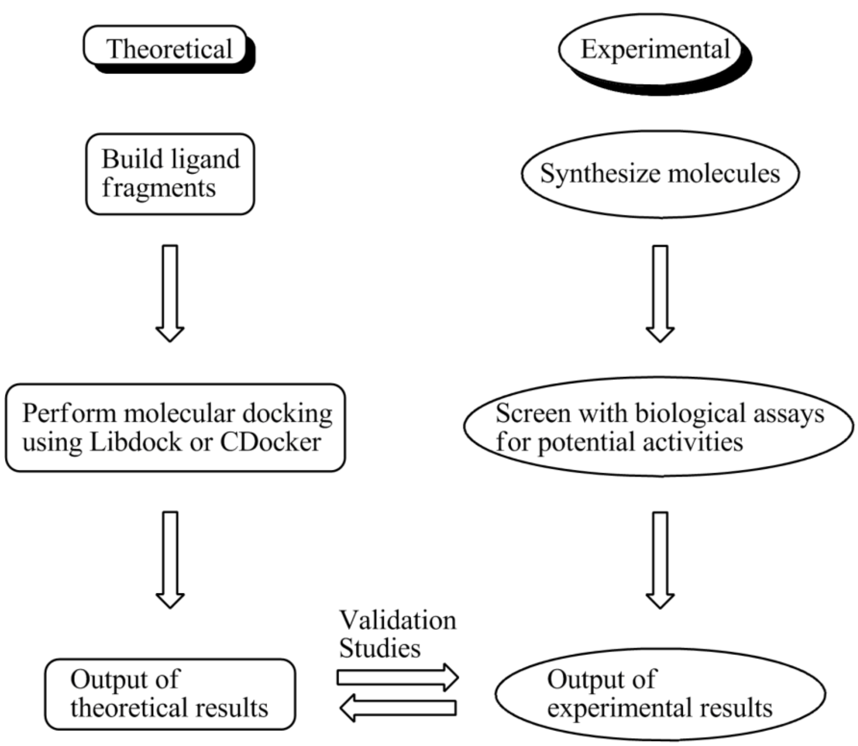

Figure 5.1: Schematics of molecular docking in conjunction with experimental methods

5.3 Results and Discussion

5.3.1 Molecular docking of PTZ derivatives with ChE's

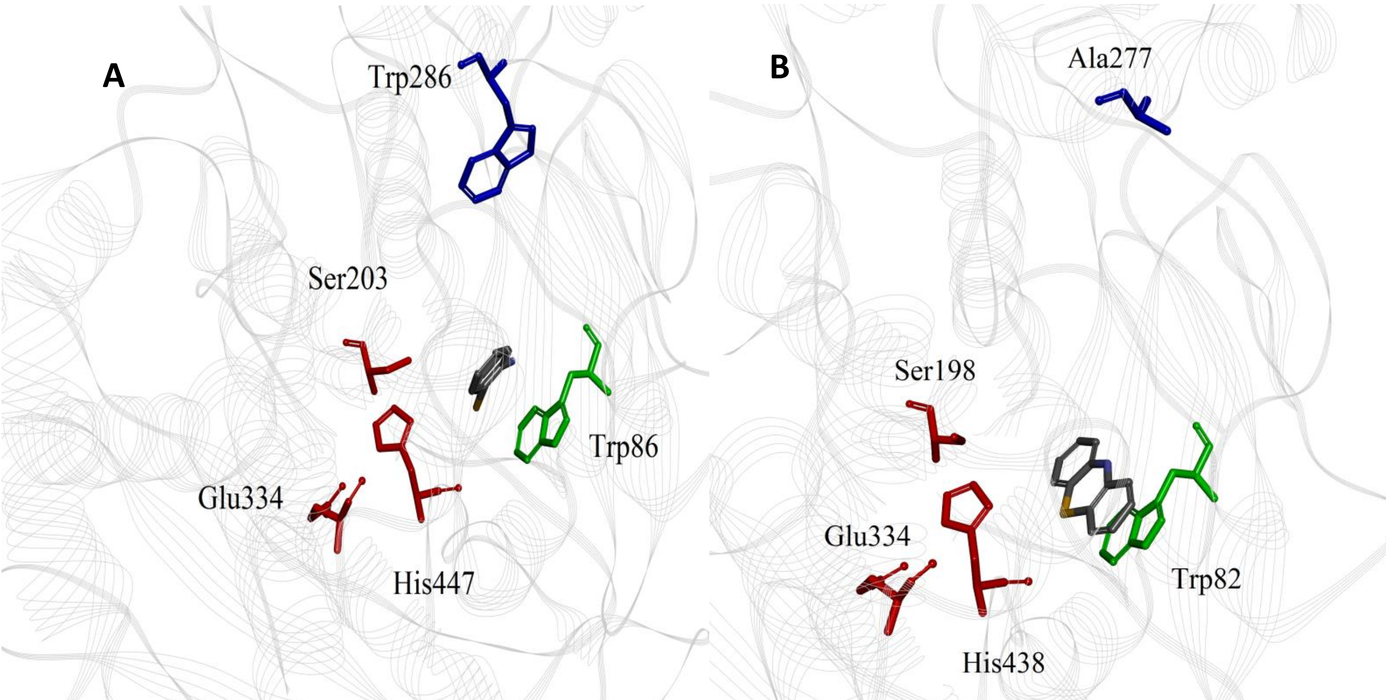

Figure 5.2: Docking of 10-*H*-phenothiazine (**5**) in the active site of *h*AChE (A) and *h*BuChE (B). Hydrogen atoms are not shown for clarity. Red: catalytic triad, Green: cationic site, Blue: PAS.

The binding mode of **5** in *h*AChE (pdb ID: 4EY7) (**Figure 5.2**) demonstrates that its tricyclic core was sandwiched between the catalytic triad and cationic binding site with multiple hydrophobic pi-pi stacked interactions with Trp86 (distances ≈ 4.05 – 4.92 Å). A similar docking study of **5** within the *h*BuChE (pdb ID: 1P0I) active site shows that the tricyclic core was in a planar geometry closer to the cationic site of Trp82, with all three rings participating in multiple pi-pi stacked interactions (distances ≈ 3.60 – 5.39 Å) as shown in **Figure 5.2**. The closer proximity to the cationic site might account for its superior BuChE inhibition (AChE IC_{50} = 7.37 μM, BuChE IC_{50} = 5.80 μM).

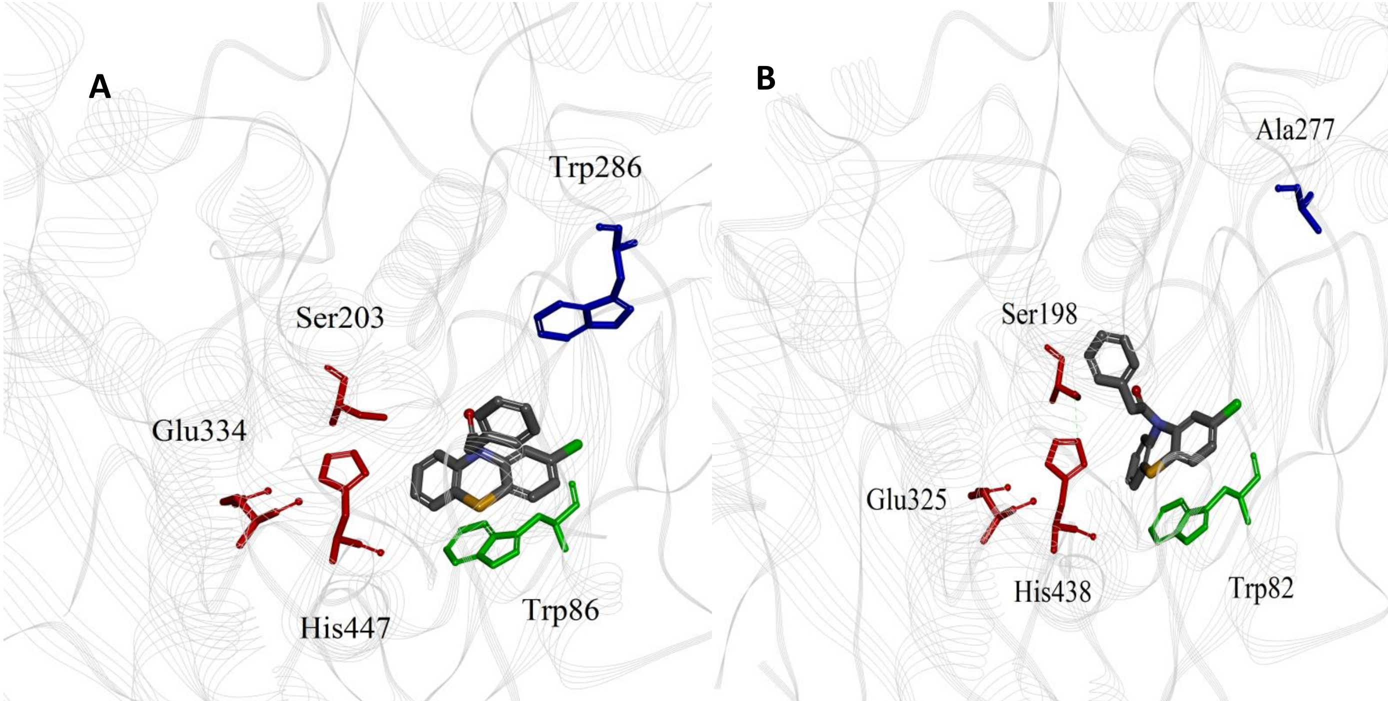

Figure 5.3: Docking of 1-(2-chloro-10*H*-phenothiazin-10-yl)-2-phenylethanone (**7h**) in the active site of *h*AChE (A) and *h*BuChE (B). Hydrogen atoms are not shown for clarity. Red: catalytic triad, Green: cationic site, Blue: PAS.

The binding mode of **7h** in *h*AChE (pdb ID: 4EY7) (**Figure 5.3**) shows that its tricyclic core was oriented across the cationic binding site with multiple hydrophobic pi-pi stacked interactions with Trp86 (distances ≈ 4.54 – 5.01 Å). One of the phenyl rings of the tricyclic core was able to interact with His447 through a pi-pi stacked interaction (distance ≈ 4.94 Å). It was also interesting to note that the N-10 phenylacetyl group was in close proximity to the Trp286 which is part of the PAS (distance ≈ 3.87 Å). Looking at its binding to *h*BuChE (pdb ID: 1P0I), the tricyclic core was closer to the cationic site of Trp82, and was more equidistant between both the cationic site and the catalytic triad. Key pi-pi stacked interactions are seen with Trp82 (distances ≈ 4.08 – 4.67 Å), but its proximity to His447 also allowed for a favorable pi-pi T-shaped interaction (distance ≈ 5.00 Å), hence providing better BuChE inhibition over AChE (AChE IC_{50} = 7.51 µM, BuChE IC_{50} = 3.64 µM).

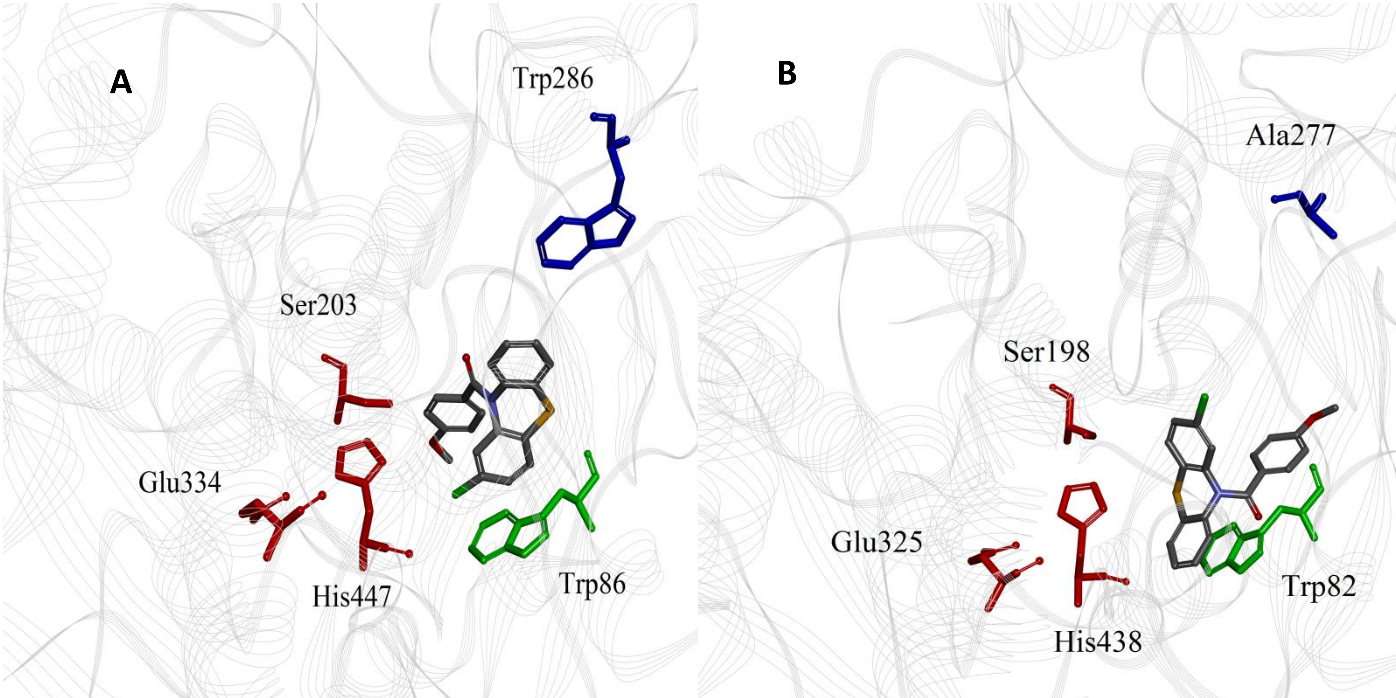

Figure 5.4: Docking of 2-chloro-10*H*-phenothiazin-10-yl (4-methoxyphenyl)methanone (**7j**) in the active site of *h*AChE (A) and *h*BuChE (B). Hydrogen atoms are not shown for clarity. Red: catalytic triad, Green: cationic site, Blue: PAS.

The binding mode of **7j** in *h*AChE (pdb ID: 4EY7) (**Figure 5.4**) demonstrates that its tricyclic core was completely shifted away from cationic binding site at a perpendicular angle where it stretched upwards reaching towards the PAS compared to both **5** and **7h** (**Figures 5.2** and **5.3**). **7j** had its chlorine participating in multiple hydrophobic pi-halogen interactions with Trp86 (distances ≈ 4.54 – 5.01 Å). The bottom portion of the tricyclic core allowed for a pi-pi T-shaped interaction (distance ≈ 5.09 Å) with Trp86, while the upper portion was oriented closer to the Trp286 of PAS (distance ≈ 5.59 Å). The key interaction of **7j** was with its N-10 4-methoxybenzoyl substituent, where the 4-methoxy formed H-bonding with Ser203 (distance ≈ 2.89 Å); the catalytic site which may account for its better AChE inhibition compared to both **5** and **7h** (AChE IC_{50} = 5.89 (**7j**) vs 7.37 and 7.51 µM respectively). Its binding mode towards *h*BuChE (pdb ID: 1P0I) shows that the tricyclic core adopted a planar conformation while interacting with Trp82, and was equidistant from both the cationic site and the catalytic triad (**Figure 5.4**). Key pi-pi stacked interactions were seen with Trp82 (distances ≈ 4.36 – 5.30 Å). An interesting note was that the 4-methoxybenzoyl group was oriented away from the catalytic triad, but was in close proximity to Trp82 with the carbonyl oxygen participating in H-bonding interaction (distance ≈ 2.99 Å), whereas the phenyl ring underwent pi-pi stacked interaction (distance ≈ 5.58 Å). Thus, while the tricyclic core was not in an ideal position towards the cationic sites of both AChE and BuChE, the N-10 4-methoxybenzoyl groups made up for lost interactions by providing key contacts between the catalytic and cationic sites to afford a dual ChE inhibition profile (AChE IC_{50} = 5.89 µM, BuChE IC_{50} = 5.35 µM).

5.3.2 Molecular docking of PSZ derivatives with ChE's

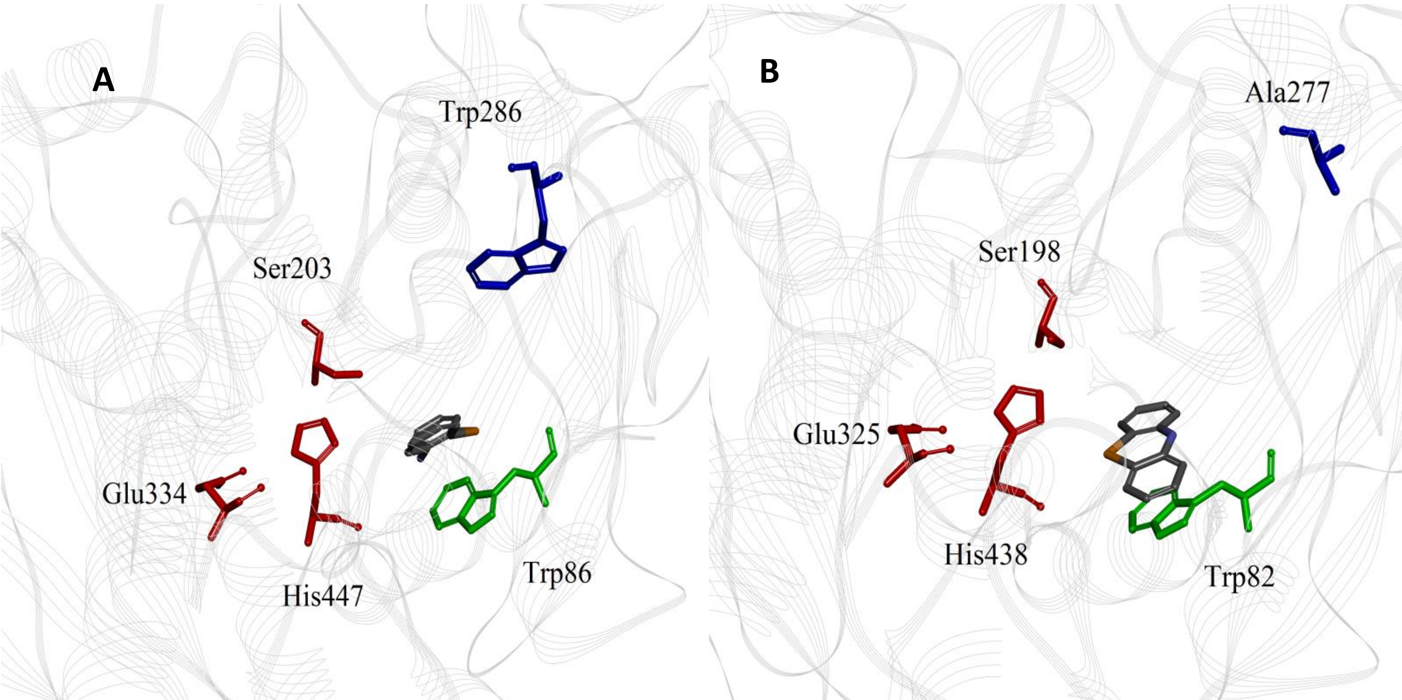

Figure 5.5: Docking of 10-*H*-phenoselenazine (**13**) in the active site of *h*AChE (A) and *h*BuChE (B). Hydrogen atoms are not shown for clarity. Red: catalytic triad, Green: cationic site, Blue: PAS.

The binding mode of **13** in *h*AChE (pdb ID: 4EY7) (**Figure 5.5**) demonstrates that its tricyclic core was closer to the cationic binding site than the catalytic triad and underwent hydrophobic pi-pi stacked interactions with Trp86 (distances ≈ 4.09 – 4.50 Å). Interestingly, the PSZ template exhibited a flipped conformation unlike **5** and the selenium moiety was away from His447. Its binding mode to *h*BuChE (pdb ID: 1P0I), showed that the tricyclic core was flipped back with the selenium moiety facing His447. The tricyclic core able to participate in multiple pi-pi stacked interactions with Trp82 (distances ≈ 4.00 – 5.55 Å). that accounts for its better BuChE inhibition (AChE IC_{50} = 5.63 μM, BuChE IC_{50} = 2.96 μM).

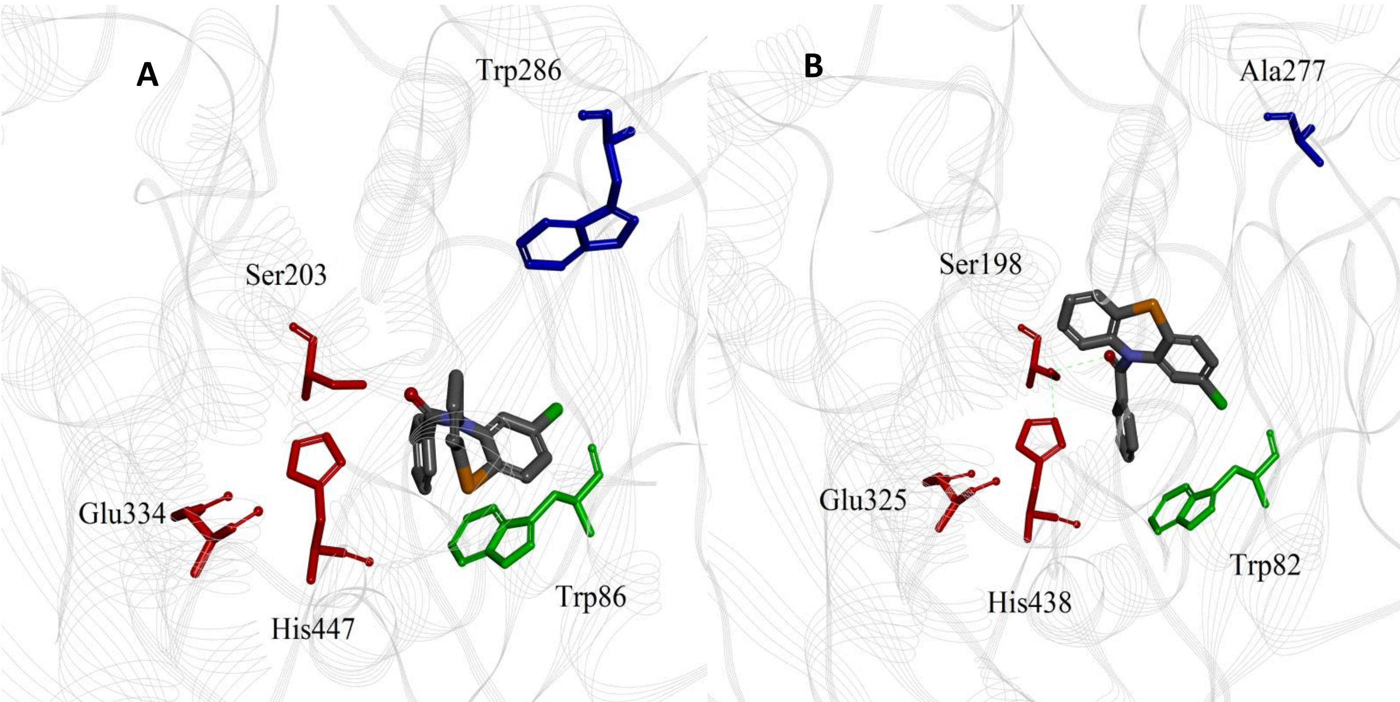

Figure 5.6: Docking of 2-chloro-10*H*-phenoselenazin-10-yl(phenyl)methanone (**15g**) in the active site of *h*AChE (A) and *h*BuChE (B). Hydrogen atoms are not shown for clarity. Red: catalytic triad, Green: cationic site, Blue: PAS.

The binding mode of **15g** in *h*AChE (pdb ID: 4EY7) (**Figure 5.6**) demonstrates that its tricyclic core was oriented away from both the catalytic triad and the cationic site. It is interesting to note that the N-10 benzoyl group was interacting with His447 through a pi-pi T-shaped hydrophobic interaction (distance ≈ 4.83 Å). Its binding to *h*BuChE (pdb ID: 1P0I), shows that the N-10 benzoyl group underwent a pi-pi T-shaped interaction with His447 (distance ≈ 4.35 Å). The carbonyl oxygen of the N-10 benzoyl group also formed a H-bond with Ser198 (distance ≈ 3.10 Å). This showed that AChE and BuChE activity is not only dictated by the cationic site of Trp86 or Trp82 respectively, but that the catalytic triad plays a key role as well (AChE IC_{50} = 6.04 µM, BuChE IC_{50} = 3.88 µM).

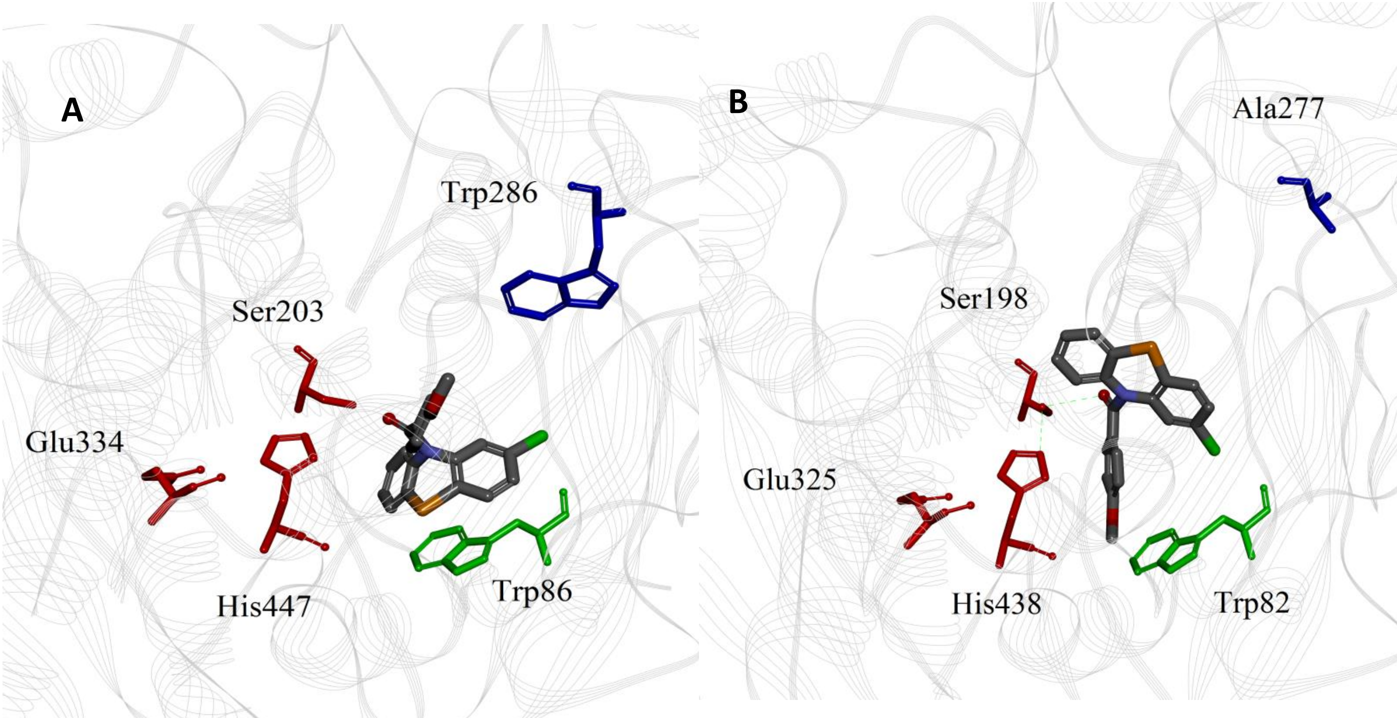

Figure 5.7: Docking of 2-chloro-10*H*-phenoselenazin-10-yl(4-methoxyphenyl)methanone (**15j**) in the active site of *h*AChE (A) and *h*BuChE (B). Hydrogen atoms are not shown for clarity. Red: catalytic triad, Green: cationic site, Blue: PAS.

The binding mode of **15j** in *h*AChE (pdb ID: 4EY7) (**Figure 5.7**) demonstrates that its tricyclic core was closer to the cationic binding site than the catalytic triad and underwent hydrophobic pi-pi stacked interactions with Trp86 (distances ≈ 4.17 – 5.02 Å). The tricyclic ring with the selenium moiety of **15j**, exhibited a similar conformation as **13,** whereas the N-10 4-methoxybenzoyl group was oriented away from the catalytic site. With *h*BuChE (pdb ID: 1P0I), **15j** exhibited an almost identical orientation like **15g**, with its tricyclic core oriented away from both the catalytic site and the catalytic triad (**Figure 5.7**). The N-10 4-methoxybenzoyl group underwent a pi-pi T-shaped interaction with His438 (distance ≈ 4.31 Å). Furthermore, the addition of the 4-methoxy group underwent hydrophobic contacts with Trp82 (distance ≈ 3.74 Å). The carbonyl oxygen of the 4-methoxybenzoyl group formed H-bonding with Ser198 (distance ≈

3.11 Å). These observations account for its dual ChE inhibition (AChE IC_{50} = 5.79 µM, BuChE IC_{50} = 4.91 µM).

5.3.3 ChE Comparisons

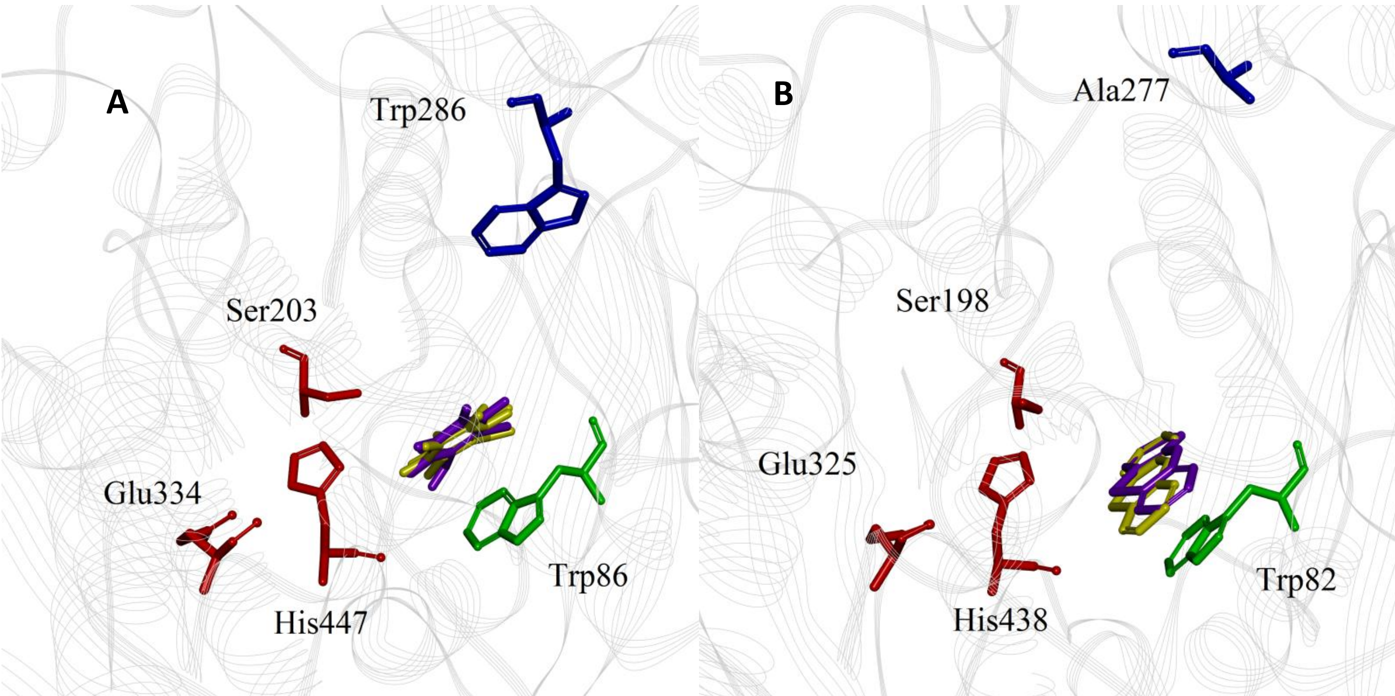

Figure 5.8: Comparison of binding modes 10-*H*-phenothiazine (**5**, yellow) and 10-*H*-phenoselenazine (**13**, purple) in the active site of *h*AChE (A) and *h*BuChE (B). Hydrogen atoms are not shown for clarity. Red: catalytic triad, Green: cationic site, Blue: PAS.

The binding modes of both **5** and **13** in *h*AChE (pdb ID: 4EY7) showed quite similar overlap in their distances both from the cationic site and the catalytic triad (**Figure 5.8**), although the PSZ **13** exhibited better AChE inhibition (AChE IC_{50} = 7.37 and 5.63 µM respectively). Similarly, in the *h*BuChE (pdb ID: 1P0I) active site, both compounds showed better angle of contact with the cationic site of Trp82, hence their increased potency (BuChE IC_{50} = 5.35 and 2.96 µM respectively).

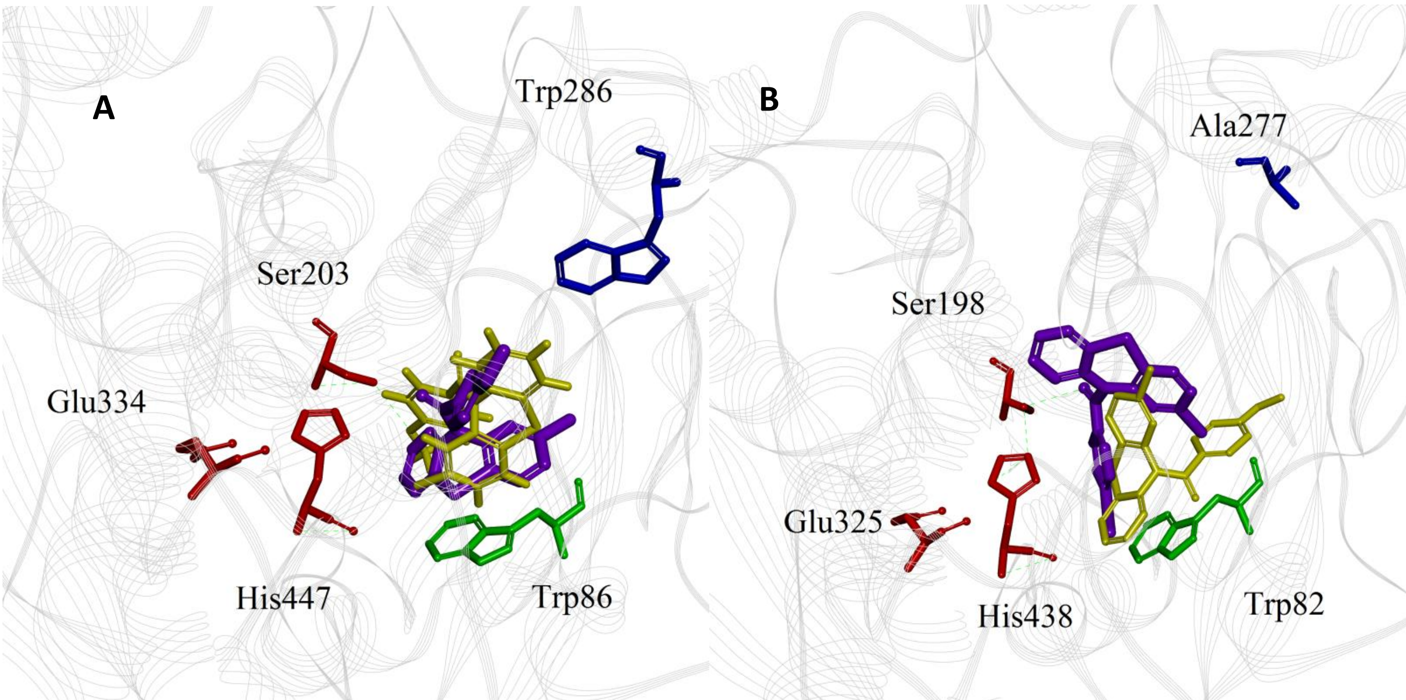

Figure 5.9: Comparison of binding modes of 2-chloro-10*H*-phenothiazin-10-yl (4-methoxyphenyl)methanone (**7j**, yellow) and 2-chloro-10*H*-phenoselenazin-10-yl (4-methoxyphenyl)methanone (**15j**, purple) in the active site of *h*AChE (A) and *h*BuChE (B). Hydrogen atoms are not shown for clarity. Red: catalytic triad, Green: cationic site, Blue: PAS

The binding modes of both **7j** and **15j** in *h*AChE (pdb ID: 4EY7) showed different poses in their orientations (**Figure 5.9**). Despite of this, their inhibition values are similar (AChE IC_{50} = 5.89 and 5.79 µM respectively). In **7j** the 4-methoxybenzoyl group interacted with both Trp86 and Ser203, while in **15j** the tricyclic ring was closer to Trp86 and His447. Similarly, looking at the *h*BuChE (pdb ID: 1P0I) active site, both compounds again showed drastic differences in their poses but similar inhibition values (BuChE IC_{50} = 5.80 and 4.91 µM respectively). While **7j** utilized a combination of both the tricyclic core and the 4-methoxybenzoyl group to block the cationic Trp82, **15j** relied almost exclusively on the 4-methoxybenzoyl group to interact with the catalytic triad's Ser298 and His438. These results suggest that multiple interactions with both the catalytic triad and cationic site play a significant role in ChE inhibition.

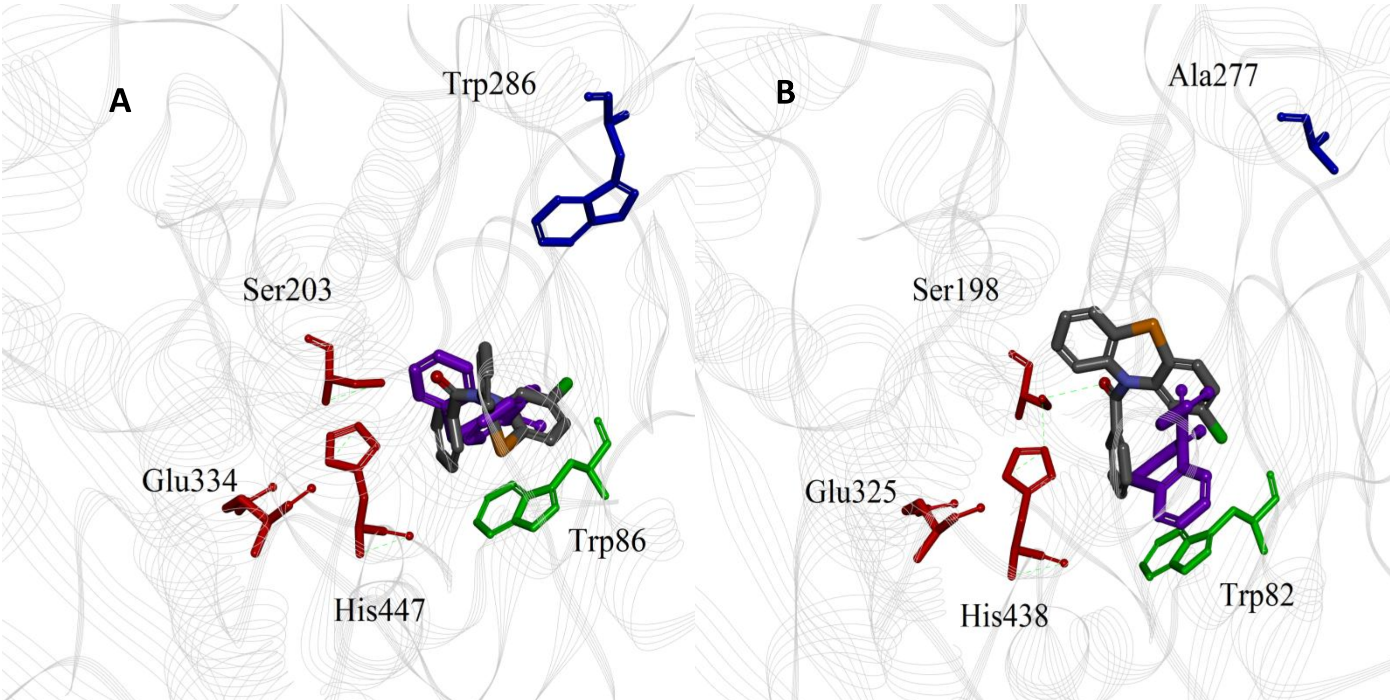

Figure 5.10: Comparison of binding modes of 10*H*-phenoselenazin-10-yl (phenyl)methanone (**15a**, purple) and 2-chloro-10*H*-phenoselenazin-10-yl (phenyl)methanone (**15g**) in the active site of *h*AChE (A) and *h*BuChE (B). Hydrogen atoms are not shown for clarity. Red: catalytic triad, Green: cationic site, Blue: PAS

The binding modes of both **15a** and **15g** in *h*AChE (pdb ID: 4EY7) show different orientations, but similar distances from both the cationic site and the catalytic triad (**Figure 5.10**). Accordingly, their AChE inhibition values were also similar (AChE IC_{50} = 5.43 and 6.04 µM respectively). In the *h*BuChE (pdb ID: 1P0I) active site, **15a** had its tricyclic core oriented away from the cationic site, and had its benzoyl group sticking away from the cationic site giving it poor BuChE inhibition (BuChE IC_{50} = 22.75 µM). In compound **15g,** its tricyclic core was also oriented away, but its benzoyl group was oriented between both the catalytic triad and the cationic site and underwent two key interactions with the Ser198 and His438, giving it superior BuChE potency over its unchlorinated analog (BuChE IC_{50} = 3.88 μM).

5.3.4 Molecular docking of PTZ derivatives with amyloid dimer

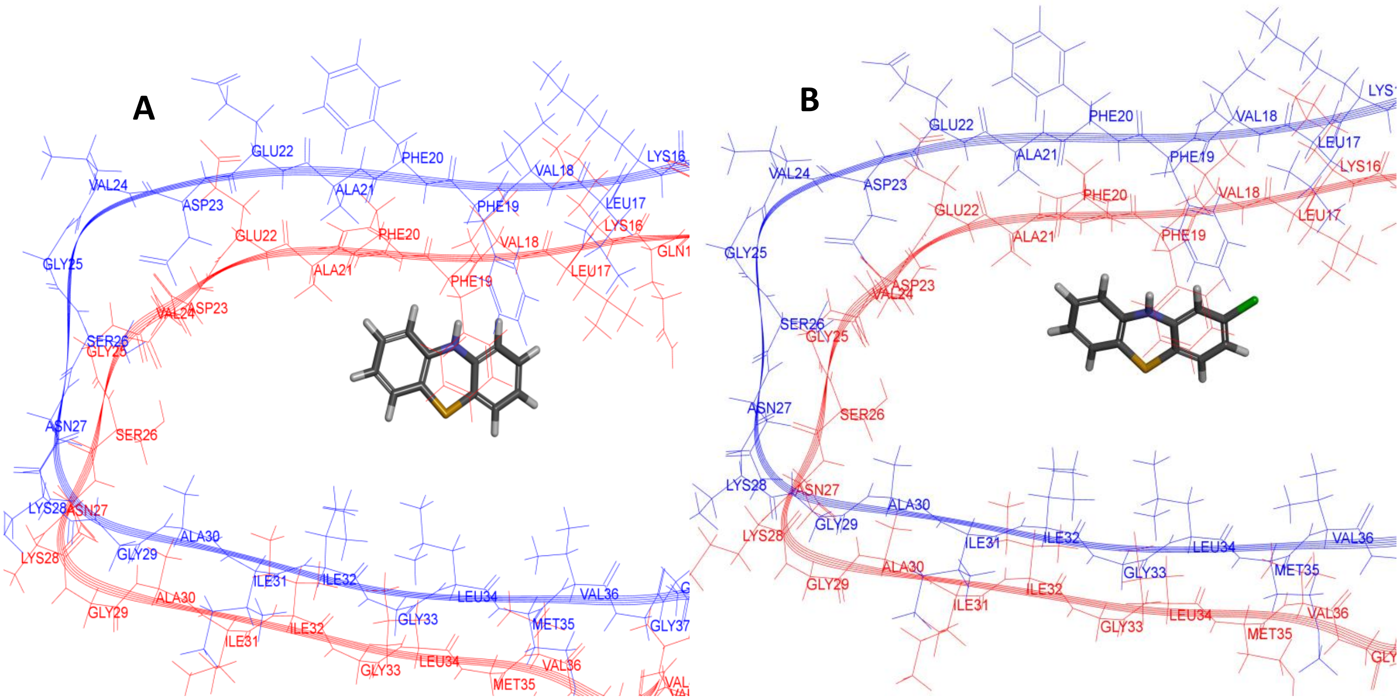

Figure 5.11: Docking of 10-*H*-phenothiazine (**5**, A) and 2-chloro-10-*H*-phenothiazine (**6**, B) in the amyloid beta dimer model. Hydrogen atoms are not shown for clarity. Red: Chain A, Blue: Chain B

The binding mode of **5** and **6** was investigated in the Aβ dimer model (pdb ID: 2LMN). The binding mode of **5** showed that its tricyclic core was in a perfect position to provide hydrophobic pi-pi stacked interactions with Phe19 of chain A (distances ≈ 3.65 – 4.65 Å) as shown in **Figure 5.11**. One of the phenyl rings of the tricyclic core was also able to network with Phe20 of chain A through pi-pi T-shaped interaction (distance ≈ 5.69 Å). The nitrogen was H-bonded to the Val18 backbone oxygen (distance ≈ 1.91 Å). The binding mode of **6** showed similar features in its interaction with the amyloid dimer. The tricyclic core was slightly further away compared to **5**, but was still able to interact with Phe19 and Phe20 of chain A through pi-pi stacking (distances ≈ 4.75 – 5.22 Å). The nitrogen was too far for H-bonding, but instead the added chlorine provided pi-halogen interactions with Phe19 (distance ≈ 4.95 Å) and Leu17 (distance ≈ 4.56 Å) respectively. Both **5** and **6** docked in similar positions to the amyloid dimer in the hydrophobic KLVFFA region which known to be the nucleation site of Aβ-aggregation (Figure 5.11). Specifically, strong interactions with both Phe19 and Phe20 of chain A were seen. The added proximity and pi-pi T-shaped interaction of compound **5** might contribute to its better anti-aggregation activity compared to the C-2 chloro compound **6**.

5.3.5 Molecular docking of PSZ derivatives with amyloid dimer

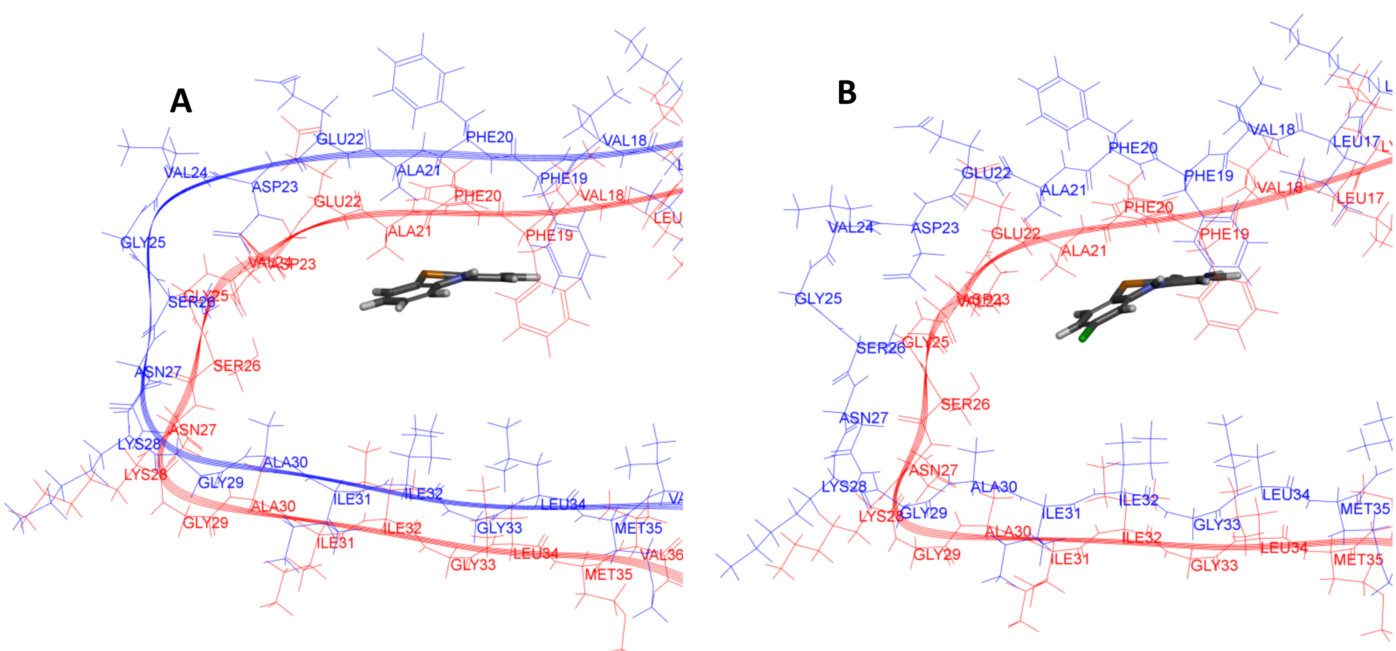

Figure 5.12: Docking of 10-*H*-phenoselenazine (**13**, A) and 2-chloro-10-*H*-phenoselenazine (**14,** B) in the amyloid beta dimer model. Hydrogen atoms are not shown for clarity. Red: Chain A, Blue: Chain B

The binding mode of **13** and **14** was investigated in the Aβ dimer model (pdb ID: 2LMN). The binding mode of **13** showed (**Figure 5.12**) that its tricyclic core was oriented in a perpendicular fashion relative to Phe19 of chain A, leading to a pi-pi T-shaped interaction (distance ≈ 5.62 Å). The tricyclic core was also able to network with Phe20 of chain A through pi-pi stacked interaction (distance ≈ 4.58 Å). It was also interacting with amino acids that form the turn region of the Aβ dimer, allowing a pi-alkyl interaction with Ala21 of chain A (distance ≈ 4.18 Å). The binding mode of **14** showed very similar features as compound **13**. The tricyclic core underwent pi-pi T-shaped and pi-pi stacked interactions (distances ≈ 5.71 and 4.44 Å respectively) with Phe19 and Phe20. The added C-2 chlorine provided an additional pi-alkyl interaction with Ala21 (distance ≈ 3.80 and 4.37 Å). Both **13** and **14** docked in very similar positions to the Aβ dimer in the hydrophobic KLVFFA region where aggregation is known to take place. Specifically, strong interactions with both Phe19, Phe20 and Ala21 of chain A were seen. As a result, both **13** and **14** exhibited almost identical anti-aggregation inhibition.

5.3.6 Amyloid Comparisons

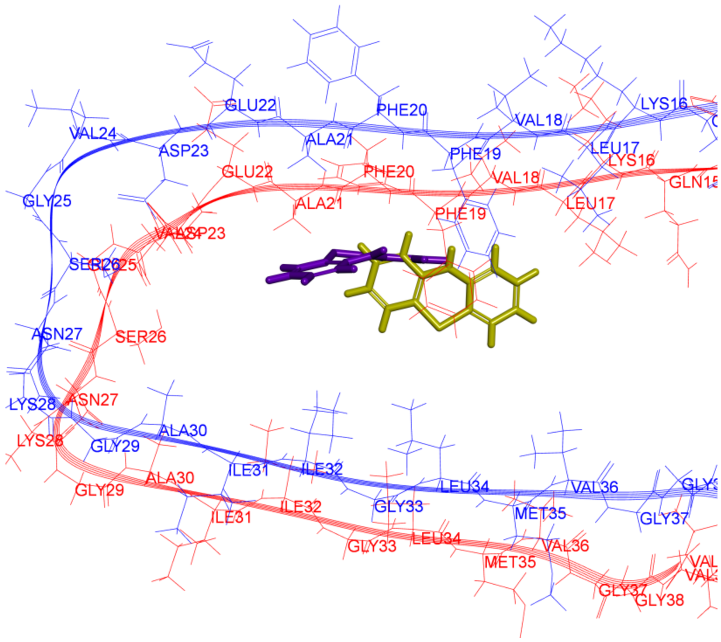

Figure 5.13: Comparison of binding modes of 10-*H*-phenothiazine (**5**, yellow) and 10-*H*-phenoselenazine (**13**, purple) in the Aβ dimer model. Hydrogen atoms are not shown for clarity. Red: Chain A, Blue: Chain B

Both **5** and **13** exhibited different binding modes to the Aβ dimer model (pdb ID: 2LMN) (**Figure 5.13**). However, both showed good anti-aggregation activity towards the self-induced $A\beta_{1-42}$ with comparable potency relative to the reference agent orange G. Both bound in the hydrophobic KLVFFA region of the Aβ dimer, which highlights the importance of the proximity to that region.

5.4 Conclusions

Both PTZ's and PSZ's exhibit different binding modes within the active sites of both AChE and BuChE enzymes. The AChE docking results gave similar poses across all compounds, evident in the relatively low range of inhibitory values across all compounds (AChE IC_{50} = 4.63 – 9.97 μM). Significant differences occurred in their ability to inhibit BuChE enzymes. For example, compound **7h** was most BuChE inhibitor in the PTZ series (BuChE IC_{50} = 3.64 μM). Among the PSZ's compound **13** showed the importance of proximity towards the cationic binding site as well which led to potent BuChE inhibition (IC_{50} = 2.96 μM). These studies indicate that the cholinesterase inhibition relies on the proximity of either PTZ and PSZ compounds towards the cationic site of Trp (86 or 82) and or the catalytic triad (Ser, His, Glu).

In the Aβ dimer model, nonacylated PTZ and PSZs exhibited good anti-aggregation properties suggesting that a either a sulfur or selenium based fused tricyclics are a useful template to design anti-amyliid agents. It also shows that compounds that interact with the hydrophobic KLVFFA region exhibit good anti-aggregation properties. Interestingly, the PTZ and PSZ compounds evaluated interacted with chain A exclusively in the modeling. Key interactions were seen with both the phenylalanine residues at 19 and 20 of chain A, indicating the importance of nonpolar interactions and anti-aggregation properties.

The molecular docking studies showed that the tricyclic ring templates PTZ and PSZ's have the ability to bind to both AChE and BuChE. Their inhibitory potency can be modulated by steric and electronic factors. Furthermore, nonacylated PTZ and PSZ's exhibit good anti-aggregation properties suggesting that these small molecules can exhibit dual ChE and anti-amyloid properties and their potential development as anti-AD agents.

Chapter 6: Conclusion and Future Directions

6.1 Conclusion

Over the course of this research project a compound library of 26 PTZ and PSZ derivatives were designed, chemically synthesized, and biologically evaluated for their AChE, BuChE, anti-amyloid aggregation, antioxidant and cell viability activity.

PTZ and PSZ design were developed through a combination of reviewing of past literature to encompass the most optimal functional groups to help create a multi-target compound library, and utilizing preliminary computational modeling studies to further assess compound potential. The compound library synthesized through organic chemistry utilized different methods and approaches to give yields ranging from 25 – 95%. Biological evaluations were accomplished through previously developed protocols optimized for the purpose of this project. After biological profiles were established for the ChE and anti-amyloid aggregation assays, computational modeling was re-examined as a tool to view specific binding patterns to validate SAR data found. A summary of the drug properties for PTZ (**5**, **6**, **7a-l**) and PSZ (**13**, **14**, **15a-l**) are outlined below:

Molecular Weights (MW): 199.27 – 444.77 Da

Partition Coefficient (ClogP): 3.56 – 6.96

AChE Inhibition (IC_{50}): 4.63 – 9.97 µM

BuChE Inhibition (IC_{50}): 3.00 – 110.52 µM

Anti-Amyloid Aggregation (% inhibition at 25 µM): 5.9 – 61.9%

Antioxidant Capacity (% Inhibition at 50 µM): 38.3 – 92.1%

Neuroblastoma Cell Viability (at 50 µM): 43.0 – 100%

The ChE profiles of the 26 synthesized novel tricyclics showed moderate inhibition. (Table 4.1 and 4.2) In general, the derivates exhibited better AChE inhibition compared to BuChE. The introduction of N-acyl groups increased AChE potency but not to a great extent. The most potent AChE inhibitor was **15d (**(4-methoxyphenyl)-10*H*-phenoselenazin-10-ylmethanone; AChE IC_{50} = 4.63 µM). The most potent BuChE inhibitor was **13** (10*H*-phenoselenazine; BuChE IC_{50} = 3.00 µM), which had better BuChE inhibition compared to donepezil and galantamine, but not as potent as tacrine (BuChE IC_{50} = 0.04 µM). The 2-chloro derivates greatly improved BuChE potency compared to their unchlorinated analogs, making them suitable dual cholinesterase templates. Overall the best dual cholinesterase derivative was seen for **15j** (2-chloro-10*H*-phenoselenazin-10-yl(4-methoxyphenyl)methanone; AChE IC_{50} = 5.79 µM, BuChE IC_{50} = 4.91 µM).

Select derivatives were screened for their amyloid aggregation inhibition towards self-induced $A\beta_{1-42}$ (Table 4.3 and 4.4). The unsubstituted derivatives showed that they were able to decrease $A\beta_{1-42}$ fibril formation, affecting both the growth and saturation phases (% inhibition at 25 µM: 45.0 – 61.9%). The N-acylation was detrimental to aggregation activity as there was up to 10-fold decrease seen in their anti-aggregation activity (% inhibition at 25 µM: 5.9 – 11.1%). The most potent anti-amyloid aggregation inhibitor was **5** (10*H*-phenothiazine; % inhibition at 25 µM = 61.9%) which showed greater potency than orange G.

The same derivatives were also screened for their antioxidant properties towards radical scavenging (Table 4.5 and 4.6). The derivatives showed moderate to good antioxidant capacities (% inhibition at 50 µM: 38.3 – 92.1%). Showing a similar trend as the amyloid aggregation assay, the unsubstituted derivatives showed that they were potent antioxidant radical scavengers (% inhibition at 50 µM: 73.2 – 92.1%) as they exhibited comparable potency to trolox (% inhibition at 50 µM: 99.2%). The N-acylation again affected their activity and there was approximately 2-fold decrease in their antioxidant activity.

SHSY-5Y neuroblastoma cell viability was also assessed in the presence of select test compounds. Generally they showed moderate to good values (% cell viability at 50 µM: 43.0 – 100%). The addition of N-acyl substituents to these compounds increased their cell viability. This effect was more pronounced in the PSZ series, with compound **15l** (2-chloro-10*H*-phenothiazin-10-yl(3,4-methoxyphenyl)methanone; % cell viability at 50 µM: 100%) showing the best viability.

The combined SAR data for the novel tricyclics synthesized show that they serve as suitable templates as dual cholinesterase inhibitors with mutli-target abilities.

6.2 Future directions

Based on the current SAR and biological profiles of PTZ and PSZ derivatives, future studies pertaining to this research include the expansion of this novel class of tricyclics to enhance ChE profiles, anti-amyloid aggregation and antioxidant properties. As seen in the ChE SAR, the addition of the chlorine at the C-2 position provides increased BuChE potency, thus the inclusion of other suitable electron withdrawing groups at the C-2 or C-3 position may lead to enhanced ChE SAR. Another interesting idea is to incorporate a heterocyclic into the either the PTZ or PSZ core, rather than have substituents at the C-2 or C-3 position. Starting from 3 or 4-aminopyridine's, following the synthetic protocols of Schemes 3.5 – 3.8 to afford a completely new library of novel tricyclics (**Figure 6.1**).

Replacing the benzoyl group with heterocyclics such as pyridines or smaller cyclic groups such as furans may help in the anchoring to the PAS of AChE.

For both the anti-amyloid aggregation and antioxidant assays the N-acyl derivatives proved to be detrimental, thus the exploration of different C-2 and C-3 derivatives may provide enhanced results.

The next step in biological evaluations would also be the inclusion of the AChE-induced amyloid aggregation assay. As mentioned, the PAS of AChE is known to act as a nucleation site for aggregation to occur. Through the use of computational modeling, N-acylated compounds can be screened for their relative proximity to the PAS, where the best compounds can be chosen and synthesized. This inclusion of the AChE-induced aggregation assay may help in identifying novel PTZ and PSZ derivatives.

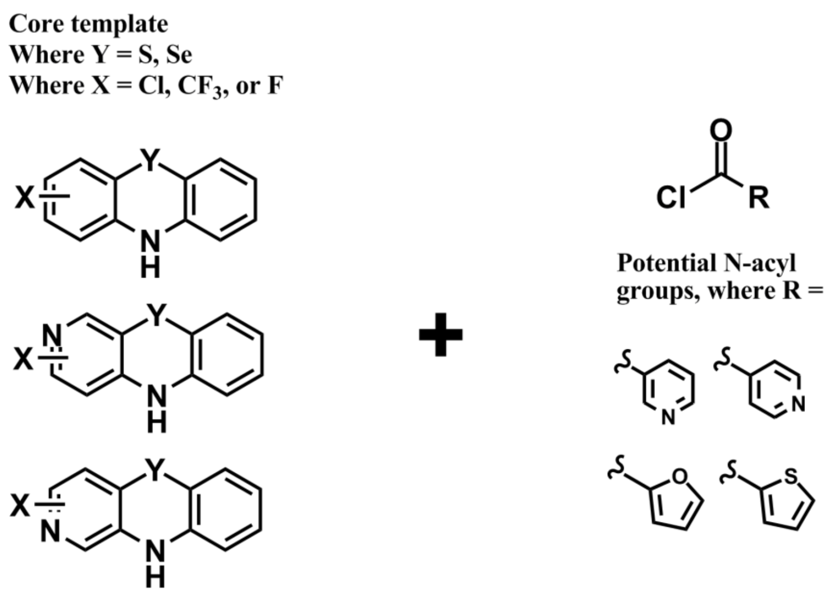

Figure 6.1: Future development of novel PTZ and PSZ derivatives

Chapter 7: Experimental

7.1 Chemistry

All solvents and reagents used were purchased from various industrial vendors (Acros Organics®, Sigma Aldrich®, and Alfa Aesar®) with minimum purity of 95% and used without further purification. Melting points were determined using a Fisher-Johns apparatus and are uncorrected. ^{1}H-NMR and ^{13}C-NMR spectra were performed on a Bruker Avance (300 and 75 MHz respectively) series spectrometer using $CDCl_3$ or DMSO-d_6 as the solvent. Coupling constants (*J*-values) were recorded in hertz (Hz) and the following abbreviations were used to represent the multiplicity of NMR signals: s = singlet, d = doublet, t = triplet, m = multiplet, br = broad. Carbon multiplicities (C, CH, CH_2, CH_3) were assigned by DEPT 90/135 experiments. High-resolution mass spectrometry analysis was done through positive ion electrospray ionization (ESI) using a Thermo Scientific Q-Exactive mass spectrometer. The mass spectrometry data for PSZ and PSZ derivatives are reported based on the most stable selenium isotope (^{80}Se). Crude product purification was done using flash chromatography with Merck 230-400 mesh silica gel 60. Combustion analysis was carried out by Midwest Microlab, LLC (Indianapolis, IN) on select compounds with the % C, H, N within ± 0.4% of theoretical values. All compounds were tested for purity by both HPLC analysis on an Agilent HPLC system and through thin-layer chromatography (TLC) showing up as a single spot, performed on Merck 60F254 silica gel plates (0.2 mm) using three different solvent systems (5:1 EtOAc:MeOH, DCM, 5:1 hexane:EtOAc) to confirm > 95% purity.

7.1.1 General method for the preparation of PTZ derivatives (7a-l)

To a mixture of phenothiazine (**5**) or 2-chlorophenothiazine (**6**) (0.40 g, 2.01 mmol) in 7 mL of anhydrous toluene at rt, the desired acyl chloride (R = phenyl, benzyl, ethylphenyl, 3-methoxyphenyl, 4-methoxyphenyl or 3,4-dimethoxyphenyl) was added (1.5 equiv). The reaction mixture was refluxed overnight at 110 °C and was monitored by TLC. Upon completion, the excess toluene was evaporated in vacuo. The crude product was purified via flash chromatography using DCM as the solvent. Final compound yields ranged from 70 - 95%.

10*H*-Phenothiazine (5): Yellow solid. ^{1}H NMR (DMSO-d_6, 300 MHz) δ 8.57 (s, 1H), 6.98 (t, *J* = 7.5 Hz, 2H), 6.91 (d, *J* = 7.2 Hz, 2H), 6.74 (t, *J* = 7.5 Hz, 2H), 6.68 (d, *J* = 7.8 Hz, 2H). ^{13}C NMR (DMSO-d_6, 75 MHz) δ 114.5 (CH), 116.2 (C), 121.7 (CH), 126.2 (CH), 127.5 (CH), 142.0 (C).

2-Chloro-10*H*-phenothiazine (6): Yellow powder. ^{1}H NMR (DMSO-d_6, 300 MHz) δ 8.70 (s, 1H), 6.97 (t, *J* = 7.1 Hz, 1H), 6.88 (d, *J* = 8.1 Hz, 2H), 6.72 - 6.77 (m, 2H), 6.61 - 6.66 (m, 2H).

10*H*-Phenothiazin-10-yl (phenyl)methanone (7a): White solid (80%). mp: 175-177°C. ^{1}H NMR (DMSO-d_6, 300 MHz) δ 7.55 - 7.63 (m, 2H), 7.41 - 7.49 (m, 2H), 7.32 - 7.41 (m, 1H), 7.19 - 7.32 (m, 8H).

1-(10*H*-Phenothiazin-10-yl)-2-phenylethanone (7b): Yellow solid (94%). mp = 153-155°C. ^{1}H NMR ($CDCl_3$, 300 MHz) δ 7.54 (d, *J* = 7.7 Hz, 2H), 7.31 - 7.41 (m, 5H), 7.18 - 7.24 (m, 4H), 7.06 - 7.11(m, 2H), 3.83 (s, 2H).

1-(10*H*-Phenothiazin-10-yl)-3-phenylpropan-1-one (7c): Yellow solid (77%). mp = 98-100°C.^{1}H NMR (DMSO-d_6, 300 MHz) δ 7.57 (d, *J* = 7.8 Hz, 2H), 7.52 (dd, *J* = 7.7 Hz, 1.3, 2H), 7.35 (td, *J* = 7.7, 1.5 Hz, 2H), 7.23 - 7.31 (m, 2H), 7.00 - 7.23 (m, 5H), 2.63 - 2.85 (br s, 4H).

(4-Methoxyphenyl)-10*H*-phenothiazin-10-ylmethanone (7d): White crystalline solid (71%). mp = 170-173°C. ^{1}H NMR (DMSO-d_6, 300 MHz) δ 7.50 - 7.58 (m, 2H), 7.39 - 7.46 (m, 2H), 7.18 - 7.25 (m, 6H), 6.78 (d, *J* = 8.9 Hz, 2H), 3.69 (s, 3H); HRMS (ESI) m/z calcd for $C_{20}H_{16}NO_2S$ ($[M + H]^+$); 334.0902. Found 334.0895.

(3-Methoxyphenyl)-10*H*-phenothiazin-10-ylmethanone (7e): White crystalline solid (83%). mp = 155-157°C. ^{1}H NMR (DMSO-d_6, 300 MHz) δ 7.51 - 7.58 (m, 2H), 7.38 - 7.46 (m, 2H), 7.18 - 7.26 (m, 4H), 7.14 (t, *J* = 7.8 Hz, 1H), 6.88 (dd, *J* = 8.0, 2.2 Hz, 1H), 6.77 - 6.84 (m, 2H), 3.60 (s, 3H); HRMS (ESI) m/z calcd for $C_{20}H_{16}NO_2S$ ($[M + H]^+$); 334.0902. Found 334.0895.

(3,4-Dimethoxyphenyl)-10*H*-phenothiazin-10-ylmethanone (7f): Pale yellow solid (70%). mp = 176-178°C. ^{1}H NMR (DMSO-d_6, 300 MHz) δ 7.51 - 7.58 (m, 2H), 7.39 - 7.46 (m, 2H), 7.19 - 7.26 (m, 4H), 6.86 - 6.91 (m, 1H), 6.76 - 6.84 (m, 2H), 3.69 (s, 3H), 3.50 (s, 3H); ^{13}C NMR (DMSO-d_6, 75 MHz) δ 55.1 (CH_3), 55.5 (CH_3), 110.7 (CH), 112.0 (CH), 121.2 (CH), 126.6 (CH), 126.8 (CH), 127.2 (CH), 127.7 (CH), 131.3 (C), 139.4 (C), 147.7 (C), 150.5 (C), 167.4 (C). HRMS (ESI) m/z calcd for $C_{21}H_{18}NO_3S$ ($[M + H]^+$); 364.1007. Found 364.1003.

2-Chloro-10*H*-phenothiazin-10-yl(phenyl)methanone (7g): Green solid mp: 157-160°C ^{1}H NMR (DMSO-d_6, 300 MHz) δ 7.64 (d, *J* = 7.2 Hz, 2H), 7.48 (d, *J* = 7.7 Hz, 2H), 7.38 (td, *J* = 7.6 Hz, 3, 2H), 7.23 - 7.31 (m, 2H), 7.13 - 7.18 (m, 2H), 6.90 - 6.97 (m, 2H).

1-(2-Chloro-10*H*-phenothiazin-10-yl)-2-phenylethanone (7h): Yellow solid (94%). mp = 90-92°C. ^{1}H NMR (DMSO-d_6, 300 MHz) δ 7.74 (s, 1H), 7.65 (d, *J* = 7.81, 2H), 7.45 - 7.52 (m, 2H), 7.22 - 7.45 (m, 3H), 7.12 - 7.21 (m, 3H), 6.90 - 6.98 (m, 2H), 3.82 (s, 2H); HRMS (ESI) m/z calcd for $C_{20}H_{15}ClNOS$ ($[M + H]^+$); 352.0563. Found 352.0558.

1-(2-Chloro-10*H*-phenothiazin-10-yl)-3-phenylpropan-1-one (7i): Yellow oil (95%). ^{1}H NMR (DMSO-d_6, 300 MHz) δ 7.67 (s, 1H), 7.49 - 7.61 (m, 3H), 7.33 - 7.41 (m, 2H), 7.25 - 7.33 (m, 1H), 7.14 – 7.22 (m, 2H), 7.11 (d, *J* = 7.0 Hz, 1H), 7.00 - 7.08 (m, 2H), 2.65 - 2.83 (br s, 4H); HRMS (ESI) m/z calcd for $C_{21}H_{17}ClNOS$ ($[M + H]^+$); 366.0719. Found 366.0717.

2-Chloro-10*H*-phenothiazin-10-yl(4-methoxyphenyl)methanone (7j): Yellow solid (94%). mp = 153-155°C. ^{1}H NMR (DMSO-d_6, 300 MHz) δ 7.68 (s, 1H), 7.51 - 7.60 (m, 2H), 7.30 - 7.36 (m, 1H), 7.14 - 7.30 (m, 5H), 6.81 (d, *J* = 8.7 Hz, 2H), 3.70 (s, 3H); HRMS (ESI) m/z calcd for $C_{20}H_{15}ClNO_2S$ ($[M + H]^+$); 368.0512. Found 368.0510.

2-Chloro-10*H*-phenothiazin-10-yl(3-methoxyphenyl)methanone (7k): White solid (92%). mp = 140-142°C. ^{1}H NMR (DMSO-d_6, 300 MHz) δ 7.64 (s, 1H), 7.56 (t, *J* = 8.6 Hz, 2H), 7.26 - 7.37 (m, 2H), 7.13 - 7.26 (m, 3H), 6.91 (d, *J* = 8.3 Hz, 1H), 6.77 - 6.86 (m, 2H), 3.62 (s, 3H); HRMS (ESI) m/z calcd for $C_{20}H_{15}ClNO_2S$ ($[M + H]^+$); 368.0512. Found 368.0509.

2-Chloro-10*H*-phenothiazin-10-yl(3,4-methoxyphenyl)methanone (7l): Yellow solid (73%). mp = 155-158°C. ^{1}H NMR (DMSO-d_6, 300 MHz) δ 7.69 (s, 1H), 7.52 - 7.60 (m, 2H), 7.31 - 7.37 (m, 1H), 7.15 - 7.29 (m, 3H), 6.77 - 6.92 (m, 3H), 3.70 (s, 3H), 3.51 (s, 3H); HRMS (ESI) m/z calcd for $C_{21}H_{17}ClNO_3S$ ($[M + H]^+$); 398.0618. Found 398.0613.

7.1.2 General method for the preparation of diphenylamines (11 and 12)

The diphenylamine derivatives were prepared by four methods highlighted by Schemes 3.2 – 3.6. Copper (II) acetate was used as a catalyst in **Schemes 3.2 – 3.4**, which provided yields of up to 30%. **Schemes 3.5** and **3.6** highlight a two-step metal-free approach that gave superior yields of up to 50%.

Method 1: To a mixture of phenylboronic acid (0.61g, 5.00 mmol) in 10 mL of H_2O, aniline (**8**) or 3-chloroaniline (**9**) was added (3 equiv) with the copper(II)-β-cyclodextrin complex (0.05 equiv). The reaction mixture was allowed to stir overnight at rt. Upon completion, the reaction mixture was diluted with 50 mL of water and extracted with 20 mL of DCM three times. The organic layer was combined and evaporated in vacuo and the crude product was purified via flash chromatography using DCM as a solvent. Final compound yields were in the range of 6 – 10% (**Scheme 3.2**).

Method 2: To a mixture of aniline (**8**) or 3-chloroaniline (**9**) (5.48 mmol) in 20 mL of EtOAC, phenylboronic acid (2 equiv), copper acetate (0.2 equiv), sodium bicarbonate (1 equiv) and benzoic acid (0.5 equiv) was added. The reaction mixture was allowed to stir overnight at rt. Upon completion, the excess EtOAC was evaporated and the crude residue was re-diluted with DCM. The organic layer washed with brine, separated and evaporated in vacuo. The crude product was purified via flash chromatography using DCM as a solvent. Final compound yields were in the range of 18 – 25% (**Scheme 3.3**).

Method 3: To a mixture of aniline (**8**) or 3-chloroaniline (**9**) (5.48 mmol) in 20 mL of toluene, phenylboronic acid (2 equiv), copper acetate (0.1 equiv), 2,6-lutidine (1 equiv) and myrisstic acid (0.2 equiv) was added. The reaction mixture was allowed to stir overnight at 80°C. Upon completion, the excess toluene was evaporated and the crude residue was re-diluted with 2M HCl and the aqueous layer was extracted with DCM. The organic layer was separated and evaporated in vacuo. The crude product was purified via flash chromatography using DCM as a solvent. Final compound yields were in the range of 32 – 38% (**Scheme 3.4**).

Method 4: To a mixture of cyclohex-2-enone (1 mL, 10.33 mmol) in 50 mL of 1:1 THF:H_2O, iodine (1.5 equiv), DMAP (1 equiv) and potassium carbonate (1.2 equiv) was added. The reaction mixture was allowed to stir at rt for 30 mins. Upon completion, the reaction mixture was diluted with EtOAc. The organic layer was washed with saturated sodium thiosulfate and 10% HCl. The organic layer was separated and evaporated in vacuo and the crude product was purified via flash chromatography using DCM as the solvent. Final compound yields were I nthe range of 40 - 70% (**Scheme 3.5**).

Method 5: To a mixture of aniline (**8**) or 3-chloroaniline (**9**) (4.8 mmol) in 10 mL EtOH, α-iodonated 2-cyclohex-2-enone (**10,** 1.2 equiv) and p-TsOH (0.2 equiv) was added. The reaction mixture was refluxed overnight at 75 °C. Upon completion, the reaction mixture was diluted with EtOAc. The organic layer was washed with 20% sodium bicarbonate and saturated brine solution. The organic layer was separated and evaporated in vacuo. The crude product was purified via flash chromatography using DCM as the solvent. Final compound yields were in the range of 40 – 50% (**Scheme 3.6**).

2-Iodocyclohex-2-enone (10): Yellow solid (40-70%). mp = 49-50°C. ^{1}H NMR (DMSO-d_6, 300 MHz) δ 7.78 (t, *J* = 4.4 Hz, 1H), 2.51 - 2.63 (m, 2H), 2.34 - 2.43 (m, 2H), 1.93 (quin, *J* = 6.3 Hz, 2H).

Diphenylamine (11): Yellow solid (40-50%). mp = 50-52°C. ^{1}H NMR (DMSO-d_6, 300 MHz) δ 8.08 (s, 1H), 7.18 (t, *J* = 7.8 Hz, 4H), 7.02 (d, *J* = 8.1 Hz, 4H), 6.77 (t, *J* = 7.2 Hz, 2H) ^{13}C NMR (DMSO-d_6, 75 MHz) δ 116.7 (CH), 119.6 (CH), 129.1 (CH), 143.4 (C).

3-Chloro-*N*-phenylaniline (12): Brown oil (40-50%). ^{1}H NMR (DMSO-d_6, 300 MHz) δ 8.36 (s, 1H), 7.22 - 7.30 (m, 2H), 7.19 (t, *J* = 8.2 Hz, 1H), 7.07 (d, *J* = 8.1 Hz, 2H), 6.93 - 7.01 (m, 2H), 6.88 (t, *J* = 7.3 Hz, 1H), 6.78 (d, *J* = 8.1 Hz, 1H).

7.1.3 General method for the preparation of PSZ's (13 and 14)

The unsubstituted PSZ (**13** and **14**) were prepared by two different methods highlighted by **Schemes 3.7** and **3.8**. **Scheme 3.7** utilized selenium monochloride as the selenium source and gave poor yields in the range of 5 – 10%. **Scheme 3.8** shows an alternative approach that used a combination of selenium and selenium dioxide to help regenerate the selenium available *in-situ*, giving a slight improvement of yields up to 25%.

Method 1: To a mixture of diphenylamine (**11**) or 4-chloro-*N*-phenylaniline (**12**) (6.00 mmol) in 10 mL of DCM, selenium monochloride was added dropwise (1.5 equiv) at rt. Upon complete addition, the reaction mixture was refluxed for 5 hr. Upon completion, the reaction mixture was filtered through a DCM plug of celite. The excess organic layer was evaporated in vacuo and the crude product was purified via flash chromatography using 5:1 hexanes:EtOAc as the solvent. Final compounds yields were in the range of 5 – 10% (**Scheme 3.7**).

Method 2: To a mixture of selenium (1.00 g, 12.79 mmol) in 5 mL of sulpholane, the appropriate diphenylamine (**11** or **12**) (2 equiv), selenium dioxide (1.20 equiv), and iodine (0.1 equiv) was added. The reaction mixture was sealed in a pressure vial and placed in at oil bath at 150 °C for 5 hours. Upon completion, the RM was filtered through a DCM plug of celite. The crude product was evaporated in vacuo and purified by recrystallization using EtOH and then subsequently by flash chromatography using 5:1 hexanes:EtOAc as the solvent. Final compound yields were in the range of 20 – 25% (**Scheme 3.8**).

10*H*-Phenoselenazine (13): yellow solid (20%). mp: 195-197°C. ^{1}H NMR (DMSO-d_6, 300 MHz) δ 8.56 (s, 1H), 6.95 - 7.10 (m, 4H), 6.68 – 6.78 (m, 4H); ^{13}C NMR (DMSO-d_6, 75 MHz) δ 111.5 (C), 115.1 (CH), 122.1 (CH), 127.8 (CH), 128.8 (CH), 142.1 (CH). HRMS (ESI) m/z calcd for $C_{12}H_{10}N^{80}Se$ ($[M + H]^+$); 247.9978. Found 246.9895.

2-Chloro-10*H*-phenoselenazine (14): Yellow solid (26%) mp = 199-200°C. δ 8.74 (s, 1H), 6.97 - 7.14 (m, 3H), 6.66 – 6.83 (m, 4H); HRMS (ESI) m/z calcd for $C_{12}H_9ClN^{80}Se$ ($[M + H]^+$); 281.9589. Found 280.9500.

7.1.4 General method for the preparation of PSZ derivatives (15a-l)

To a mixture of phenoselenazine or 2-chlorophenoselenazine (0.356 mmol) in 7 mL of anhydrous toluene, the desired acyl chloride (R = benzoyl, phenyl acetyl, hydrocinnamoyl, 3-methoxy, 4-methoxy or 3,4-dimethoxy) was added (1.5 equiv). The reaction mixture was refluxed overnight at 110 °C. Upon completion, the excess toluene was evaporated in vacuo. The crude product was purified via flash chromatography using DCM as the solvent. Final compound yields ranged from 20 - 80%.

10*H*-Phenoselenazin-10-yl(phenyl)methanone (15a): Yellow solid (87%). mp = 157-159°C. ^{1}H NMR (DMSO-d_6, 300 MHz) δ 7.65 - 7.73 (m, 2H), 7.39 - 7.45 (m, 2H), 7.13 - 7.26 (m, 9H); HRMS (ESI) m/z calcd for $C_{19}H_{14}NO^{80}Se$ ($[M + H]^+$); 352.0241. Found 352.0235.

1-(10*H*-Phenoselenazin-10-yl)-2-phenylethanone (15b): Yellow solid (91%). mp = 111-113°C. ^{1}H NMR (DMSO-d_6, 300 MHz) δ 7.66 (d, *J* = 7.6 Hz, 4H), 7.40 (t, *J* = 7.6 Hz, 2H), 7.22 - 7.30 (m, 2H), 7.13 - 7.21 (m, 3H), 6.90 - 6.99 (m, 2H), 3.72 (s, 2H); HRMS (ESI) m/z calcd for $C_{20}H_{16}NO^{80}Se$ ($[M + H]^+$); 366.0397. Found 366.0393.

1-(10*H*-Phenoselenazin-10-yl)-3-phenylpropan-1-one (15c): Yellow solid (87%). mp = 106-109°C. ^{1}H NMR (DMSO-d$_6$, 300 MHz) δ 7.68 (d, *J* = 7.6 Hz, 2H), 7.57 (d, *J* = 7.8 Hz, 2H), 7.36 (t, *J* = 7.5 Hz, 2H), 7.06 - 7.28 (m, 5H), 7.02 (d, *J* = 7.2 Hz, 2H), 2.73 (s, 2H), 2.61 (br s, 2H); HRMS (ESI) m/z calcd for $C_{21}H_{18}NO^{80}Se$ ([M + H]$^+$); 380.0554. Found 380.0546.

(4-Methoxyphenyl)-10*H*-phenoselenazin-10-ylmethanone (15d): White solid (79%). mp = 184-186°C. ^{1}H NMR (DMSO-d$_6$, 300 MHz) δ 7.66 - 7.72 (m, 2H), 7.39 - 7.47 (d, *J* = 7.3 Hz, 2H), 7.13 - 7.27 (m, 6H), 6.76 (d, *J* = 8.7 Hz, 2H), 3.68 (s, 3H); HRMS (ESI) m/z calcd for $C_{20}H_{16}NO_2{}^{80}Se$ ([M + H]$^+$); 382.0346. Found 382.0339.

(3-Methoxyphenyl)-10*H*-phenoselenazin-10-ylmethanone (15e): White solid (84%). mp = 157-159°C. ^{1}H NMR (DMSO-d$_6$, 300 MHz) δ 7.71 (dd, *J* = 7.1, 1.7 Hz, 2H), 7.44 (d, *J* = 7.5 Hz, 2H), 7.09 - 7.29 (m, 5H), 6.77 - 6.92 (m, 3H), 3.60 (s, 3H); HRMS (ESI) m/z calcd for $C_{20}H_{16}NO_2{}^{80}Se$ ([M + H]$^+$); 382.0346. Found 382.0338.

(3,4-Dimethoxyphenyl)-10*H*-phenoselenazin-10-ylmethanone (15f): Yellow solid (73%). mp = 185-187°C. ^{1}H NMR (DMSO-d$_6$, 300 MHz) δ 7.71 (d of d, *J* = 7.3, 1.7 Hz, 2H), 7.44 (d of d, *J* = 7.7 Hz, 1.4, 2H), 7.14 - 7.29 (m, 4H), 6.87 - 6.93 (m, 1H), 6.73 - 6.84 (m, 2H), 3.69 (s, 3H), 3.49 (s, 3H); ^{13}C NMR (DMSO-d$_6$, 75 MHz) δ 55.2 (CH_3), 55.4 (CH_3), 110.7 (CH), 112.0 (CH), 122.1 (CH), 126.7 (CH), 126.8 (C), 127.4 (CH), 127.8 (CH), 129.2 (C), 130.3 (CH), 139.6 (C), 147.6 (C), 150.4 (C), 167.3 (C). HRMS (ESI) m/z calcd for $C_{21}H_{18}NO_3{}^{80}Se$ ([M + H]$^+$); 412.0452. Found 412.0445.

2-Chloro-10*H*-phenoselenazin-10-yl(phenyl)methanone (15g): Yellow solid (79%). mp = 155-158°C. ^{1}H NMR (DMSO-d$_6$, 300 MHz) δ 7.68 - 7.78 (m, 3H), 7.13 - 7.37 (m, 9H); HRMS (ESI) m/z calcd for $C_{19}H_{13}ClNO^{80}Se$ ([M + H]$^+$); 385.9851. Found 385.9841.

1-(2-Chloro-10*H*-phenoselenazin-10-yl)-2-phenylethanone (15h): Yellow semi-solid oil (73%). ^{1}H NMR (DMSO-d$_6$, 300 MHz) δ 7.75 (br s, 1H), 7.67 (d, *J* = 8.3 Hz, 3H), 7.42 (t, *J* = 7.9 Hz, 2H), 7.23 - 7.37 (m, 2H), 7.12 - 7.23 (m, 4H), 6.95 (m, 2H), 3.74 (s, 2H); HRMS (ESI) m/z calcd for $C_{20}H_{15}ClNO^{80}Se$ ([M + H]$^+$); 400.0007. Found 399.9998.

1-(2-Chloro-10*H*-phenoselenazin-10-yl)-3-phenylpropan-1-one (15i): Yellow solid (84%). mp = 90-92°C. ^{1}H NMR (DMSO-d$_6$, 300 MHz) δ 7.74 (d, *J* = 8.5 Hz, 3H), 7.10 – 7.45 (m, 9H), 2.69 - 2.87 (br s, 4H); HRMS (ESI) m/z calcd for $C_{21}H_{17}ClNO^{80}Se$ ([M + H]$^+$); 414.0164. Found 414.0155.

2-Chloro-10*H*-phenoselenazin-10-yl(4-methoxyphenyl)methanone (15j): White solid (47%). mp = 155-156°C. ^{1}H NMR (DMSO-d$_6$, 300 MHz) δ 7.64 - 7.78 (m, 3H), 7.31 (d, *J* = 8.2 Hz, 2H), 7.16 - 7.26 (m, 4H), 6.80 (d, *J* = 8.4 Hz, 2H), 3.70 (s, 3H); HRMS (ESI) m/z calcd for $C_{20}H_{15}ClNO_2{}^{80}Se$ ([M + H]$^+$); 415.9957. Found 415.9947.

2-Chloro-10*H*-phenoselenazin-10-yl(3-methoxyphenyl)methanone (15k): Yellow solid (52%). mp = 135-137°C. ^{1}H NMR (DMSO-d$_6$, 300 MHz) δ 7.36 - 7.80 (m, 3H), 7.26 - 7.38 (m, 2H), 7.11 - 7.25 (m, 3H), 6.90 (d, *J* = 8.2 Hz, 1H), 6.78 - 6.86 (m, 2H), 3.61 (s, 3H); HRMS (ESI) m/z calcd for $C_{20}H_{15}ClNO_2{}^{80}Se$ ([M + H]$^+$); 415.9957. Found 415.9947.

2-Chloro-10*H*-phenothiazin-10-yl(3,4-methoxyphenyl)methanone (15l): Yellow solid (28%). mp = 138-140°C. ^{1}H NMR (DMSO-d$_6$, 300 MHz) δ 7.65 - 7.78 (m, 3H), 7.26 - 7.35 (m, 2H), 7.15 - 7.24 (m, 2H), 6.73 - 6.96 (m, 3H), 3.69 (s, 3H), 3.50 (s, 3H); HRMS (ESI) m/z calcd for $C_{21}H_{17}ClNO_3{}^{80}Se$ ([M + H]$^+$); 446.0062. Found 446.0054.

7.2 Biochemistry

7.2.1 Cholinesterase Assay

The compounds were evaluated in a 96-well plate with reference compounds tacrine, donepezil and galantamine. Various concentrations of test compounds (1, 5, 10, 25, 50 μM) were used to analyze ChE inhibition. Each well contained a total of 250 μL; 160 μL of DTNB, 50 μL of enzyme (AChE or BuChE), 10 μL of test compound and 30 μL of acetyl or butyryl thiocholine iodide. Acetyl or butylrylthiocholine iodide solutions were prepared in ultra pure water (UPW, 15 mM) and were added after a 5 minute incubation. Blank solutions contained 10 μL of DMSO and controls contained 8 μL of buffer A and 2 μL of DMSO. To ensure no interference from external light sources, the 96-well plate was kept away from light during the incubation period. Absorbance values were taken every minute for 5 minutes at 412 nm. To determine the 50% inhibitory concentration (IC_{50}), the average absorbance values taken at the six different time intervals were subtracted from the average control absorbance. This value was then divided by the average control absorbance to give percent inhibition of a given test compound. Finally, by plotting the percent inhibition against the test compound concentration logarithmically, the IC_{50} was determined. The results were expressed as mean ± standard deviation (SD) of two separate experiments (n = 3).

$$\frac{\text{100\%-activity absorbance-test compound absorbance}}{\text{100\%-activity absorbance}} \times 100\%$$

Preparation of cholinesterase assay solutions:

Buffer A was prepared by dissolving 3.029 g of Trizma base (Sigma), 2.922 g of NaCl and 2.033 g of $MgCl_2$•$6H_2O$ in 450 mL of UPW. The 1M HCl was added to the solution until pH 8.0, and finally the solution was filled up to 500 mL with UPW.

Buffer B was prepared by dissolving 3.029 g of Trizma base (Sigma) in UPW followed by 0.50 g of BSA and 20 mL of UPW. Finally, add 0.086 mL of 1M HCl was added until pH was 8.0 then the volume was adjusted to 50 mL with UPW.

Human acetylcholinesterase solution (0.22 units/mL) was prepared by dissolving the supplied amount of *h*AChE (425.95 units/mg) in 9.4 mL of buffer B. 0.5 mL of the aforementioned solution was added to an additional 0.5 mL of buffer B; 0.011 mL of this solution was added to 5.31 mL of buffer B yielding a final concentration of 0.22 units/mL.

Human butyrylcholinesterase solution (0.12 units/mL) was prepared by dissolving the supplied amount of *h*BuChE (221 units/mg) in 9.0 mL of buffer B. 0.5 mL of the aforementioned solution was added to an additional 0.5 mL of buffer B; 0.010 mL of this solution was added to 9.198 mL of buffer B yielding a final concentration of 0.12 units/mL.

7.2.2 Anti-Amyloid Aggregation Assay

The compounds were evaluated in a 384-well plate for their ability to inhibit the formation of $A\beta_{1\text{-}42}$ aggregates (self-induced). Each well contained: 55 μL of ThT, 10 μL of test compound solution, 10 μL of $A\beta_{1\text{-}42}$ and 25 μL of phosphate buffer. Background control solutions contained 55 μL of ThT and 44 μL of phosphate buffer and 1 μL of DMSO. Compound background solutions contain 55 μL of ThT, 35 μL of phosphate buffer and 10 μL of test compound. The

Aβ_{1-42} control solutions contain 55 μL of ThT, 34 μL of phosphate buffer, 1 μL of DMSO and 10 μL of Aβ_{1-42}. The solutions were then incubated for 16 hr. 55 μL of ThT was then added to all wells and measurements are taken at 5 minute intervals for 16 hours at 446 nm (excitation) and 490 nm (emission). The direct measure of a test sample's ability to block Aβ fibril aggregation was determined by comparing fluorescence intensities in the presence and absence of inhibitors. The percentage inhibition was calculated using the equation 100% control value (i.e. no inhibitor) - [(IF_i - IF_o)] where IF_i and IF_o are the fluorescence intensities in the presence of ThT and absence of ThT before 16 h incubation, respectively. The results were expressed as mean ± standard deviation (SD) of two separate experiments (n = 3). Reference compound orange G was used as the reference agent for comparison.

Preparation of anti-amyloid aggregation assay solutions:

ThT solution was prepared by dissolving 0.94 g of glycine and 1.20 mg of ThT in 150 mL UPW. Using a 50 mM aqueous solution of NaOH, the pH of the buffer solution was adjusted to pH 8.5 and the volume was made up to 250 mL with UPW.

Sodium phosphate dibasic heptahydrate buffer was prepared by dissolving 28.81 g of $Na_2HPO_4 \cdot 7H_2O$ in 300 mL of UPW. The pH of the buffer solution was adjusted to pH 8.0 and the volume was made up to 500 mL with UPW.

Aβ_{1-42} peptide solution was made by dissolving 1 mg of peptide hexafluoro-2-propanol (HFIP) in 1 mL of 1% ammonium hydroxide.

7.2.3 DPPH Antioxidant Assay

The compounds were evaluated in a 96-well plate with reference compounds trolox. The test compounds were prepared in methanol (50 μM). Each well contained: 50 μL of test compound and 200 μL of DPPH solution. Blank solutions contained 50 μL of test compound and 200 μL of MeOH. Negative control solutions contained 50 μL of MeOH and 200 μL of DPPH. The 96-well plate was allowed to incubate at room temperature with shaking in the absence of light for 60 minutes and absorbance was measured at 517 nm. To determine the percent inhibition, the absorbance of the negative control was subtracted by the difference of the test compounds and blank. This value was divided by the absorbance of the negative control to obtain percent inhibition. The results were expressed as mean ± standard deviation (SD) of two separate experiments (n = 3).

$$\frac{\text{Negative control absorbance-(test compound absorbance-blank absorbance)}}{\text{Negative control absorbance}} \times 100\%$$

Preparation of DPPH solution:

DPPH stock solution was freshly prepared by adding 1.97 mg of DPPH to a 50 mL volumetric flask. The solution was made up to 40 mL with anhydrous methanol. 10 mL of this solution was dluted with an additional 10 mL of anhydrous methanol.

7.2.4 MTT Cell Viability Assay

The cell viability assay was was conducted by Nyasha Gondora from Dr. Beazely's lab. The SH-SY5Y neuroblastoma cells were plated at a density of 4 $x10^5$ per mL in 96 well plates with complete growth media consisting of DMEM and Ham's F12 in a 1:1 ratio, supplemented with 2.5 nM glutamate and 10% fetal bovine serum at 37 °C in 5% CO_2. The cells were incubated overnight and treated with the test sames at various concentrations (1, 10 and 50 μM) for 24 hrs at 37 °C in triplicates (n = 3). The MTT was added in 10% of the culture medium volume to each well and the cells were cultured for an additional 3 hrs at 37 °C in 5% CO_2. After incubation, the resulting formazan crystals were solubilized with MTT reagent solution in each well and the absorbance was taken at 570 nm. All results were expressed as a relative percent of MTT to untreated controls.

7.3 Computational Chemistry

Docking experiments were performed using Discovery Studio Client provided by Structure-Based-Design from BIOVIA/Accelrys Inc. The X-ray crystal structures for *h*AChE, *h*BuChE and Amyloid fibril model were obtained from the RCSB Protein Data Bank (PDB ID: 4EY7, 1POI and 2LMN). The amyloid peptide consisting of chains A and B was extracted from the PDB file for the $A\beta_{1-40}$ dimer model. The N-terminal octapeptide region (1-8) was not considered for modeling since those residues are not involved in amyloid aggregation. The ligand molecules or interest were constructed using the "Build Fragment" tool built-in to the Discovery Studio Client. All compounds were minimized reaching a convergence of 0.01 kcal/mol Å. Docking experiments were carried out by both LibDock (rigid) and CDocker (flexible) commands in the receptor-ligand interactions protocol within the Discovery Studio library with a 10 – 15 Å sphere radius centered around each active site of each receptor. The Chemistry at HARvard Macromolecular Mechanics (CHARMm) force field was applied to all docking protocols.

7.4 Appendix A: UV scan of compounds 13 and 15f at 50 μM in methanol

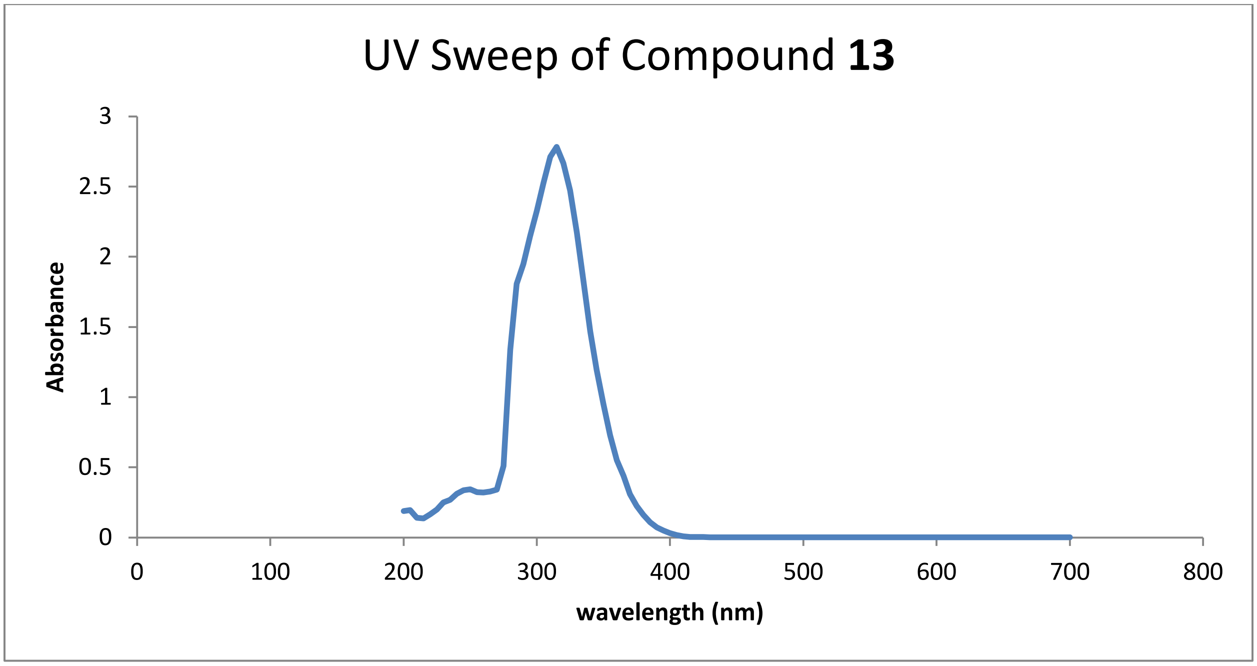

Figure A.1: UV scan of compound **13** at 50 μM in methanol

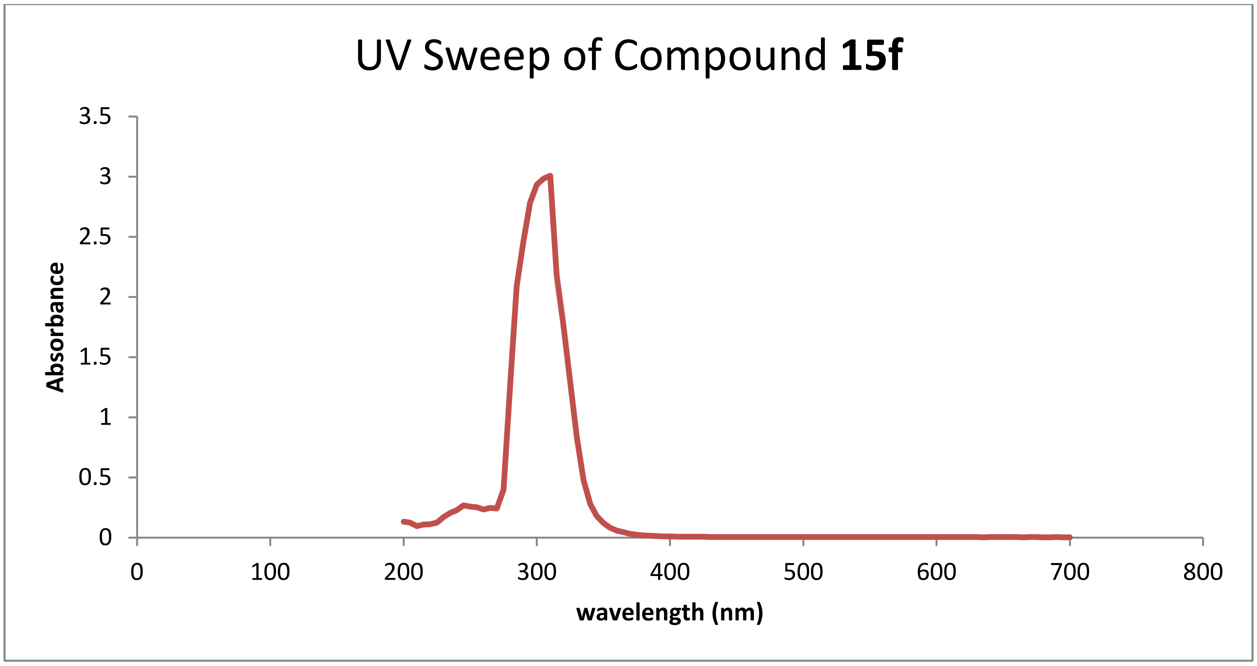

Figure A.2: UV scan of compound **15f** at 50 μM in methanol

References

1. Association, A. 2014 Alzheimer's disease facts and figures. *Alzheimers Dement:.* **2014,** *10*, 1 – 80.
2. Berchtold N. C.; Cotman C. W.; Evolution in the conceptualization of dementia and Alzheimer's disease: Greco-Roman period to the 1960s. *Neurobiol. Aging*. **1998**, *19*, 173–189.
3. Alzheimer's Disease International. The global impact of dementia 2013 – 2050. **2013**. 1 – 8.
4. Minati, L.; Edginton, T.; Bruzzone, M. G.; Giaccone, G. Reviews: Current concepts in Alzheimer's disease: A multidisciplinary review. *Am. J. Alzheimers Dis. Other Demen*. **2009,** *24*, 95-121.
5. Alzheimer's Disease International. World Alzheimer's report 2013. **2013**. 1 – 92.
6. Selkoe, D.; Resolving controversies on the path to Alzheimer's therapeutics. *Nat. Med.* **2012,** 17, 1060 – 1065.
7. Mullard, A. Sting of Alzheimer's failures offset by upcoming prevention trials. *Nat. Rev. Drug. Discov.* **2012,** 11, 657 – 660.
8. Roberson, E,; Mucke, L. 100 years and counting: prospects for defeating Alzheimer's disease. *Science.* **2006,** 314, 781 – 784.
9. Ballard, C.; Gauthier, S.; Corbett, A.; Brayne, C.; Aarsland, D.; Jones, E. Alzheimer's disease. *Lancet*. **2011,** *377*, 1019–1031.
10. Mattson, M. P. Pathways towards and away from Alzheimer's disease. *Nature*. **2004,** *430*, 631-639.

11. Francis, P.; Palmer, A.; Snape, M.; Wilcock, G.; The cholinergic hypothesis of Alzheimer's disease: a review of progress. *J. Neurol. Neurosurg. Psychiatry*. **1999,** 66, 137 – 147.
12. Bartus, R.T. On neurodegenerative diseases, models, and treatment strategies: lessons learned and lessons forgotten a generation following the cholinergic hypothesis. *Exp.Neurol.* **2000,** *163,* 495–529.
13. Pakaski, M.; Kalman, J. Interactions between the amyloid and cholinergic mechanisms in Alzheimer's disease. *Neurochem. Inter.* **2008,** *53,* 103-111.
14. Soreq, H.; Seidman, S. Acetylcholinesterase new roles for an old actor. *Nat. Rev. Neurosci.* **2001,** *2,* 294–302.
15. Giacobini, E. Cholinesterases: New roles in brain function and in Alzheimer's disease. *Neurochem. Res.* **2003,** *28,* 525-522.
16. Tiraboschi, P.; Hansen, L.A.; Alford, M.; Masliah, E.; Thal, L.J.; Corey-Bloom, J. The decline in synapses and cholinergic activity is asynchronous in Alzheimer's disease. *Neurology.* **2000**, *55*, 1278–1283.
17. Xu, Y.; Colletier, J.P.; Weik, M.; Jiang, H.; Moult, J.; Silman, I.; Sussman, J.L. Flexibility of aromatic residues in the active-site gorge of acetylcholinesterase: x-ray versus molecular dynamics. *Biophys.J.* **2008.** *95*, 2500–2511.
18. Inestrosa, N.C.; Alvarez, A.; Perez, C.A.; Moreno, R.D.; Vicente, M. ; Linker, C.; Casanueva, O. I.; Soto, C.; Garrido, J.; Acetylcholinesterase accelerates assembly of amyloid-peptides into Alzheimer's fibrils: possible role of the peripheral site of the enzyme. *Neuron.* **1996,** *16,* 881-891.

19. Lane R.M.; Potkin S.G.; Enz A. Targeting acetylcholinesterase and butyrylcholinesterase in dementia. *Int. J. Neuropsychopharmacol*. **2006**, *9*, 101-124.

20. Vellom, D. C.; Radic, Z.; Li, Y.; Pickering, N. A.; Camp, S.; Taylor, P. Amino acid residues controlling acetylcholinesterase and butyrylcholinesterase specificity. *Biochemistry*, **1993,** *32*, 12-17.

21. Taylor, P.; Radic, Z. The cholinesterases: From genes to proteins. *Annu. Rev. Pharmacol. Toxicol.* **1994,** *34*, 281-320.

22. Saxena, A.; Redman, A. M. G.; Jiang, X.; Lockridge, O.; Doctor, B. P. Differences in active-site gorge dimensions of cholinesterases revealed by binding of inhibitors to human butyrylcholinesterase. *Chem. Biol. Interact.* **1999,** *119–120*, 61–69.

23. Craig, L.; Hong, N.; Mcdonald, R.; Revisiting the cholinergic hypothesis in the development of Alzheimer's disease. *Neurosci. Biobehav. R.* **2011,** 35, 1397 – 1409.

24. Martorana, A.; Esposito, Z.; Koch, G.; Beyond the cholinergic hypothesis: do current drugs work in Alzheimer's disease? *CNS Neurosci. Ther*. **2010,** 16, 235 – 245.

25. Illife, S.; The National Institute for Health and Clinical Excellence (NICE) and drug treatment for Alzheimer's disease. *CNS Drugs.* **2007,** 21, 177 – 184.

26. Shah, R.S.; Lee, H.G.; Zhu, X.W.; Perry, G.; Smith, M.A.; Castellani, R.J. Current approaches in the treatment of Alzheimer's disease. *Biomed. Pharmacother.* **2008,** *62*, 199-207.

27. Terry, A.V. Jr.; Callahan, P. M.; Hall, B.; Webster, S. J. Alzheimer's disease and age-related memory decline (preclinical) *Pharmacol. Biochem. Behav.* **2011,** *99*, 190.

28. Matharu, B.; Gibson, G.; Parsons, R.; Huckerby, T.; Moore, S.; Cooper, L.; Millichamp, R.; Allsop, D.; Austen, B.; Galantamine inhibits β-amyloid aggregation and cytotoxicity. *J. Neurol. Sci.* **2009,** 280, 49 – 58.

29. Hartmann, T.; Bieger, S.C.; Brühl, B.; Tienari, P.J.; Ida, N.; Allsop, D.; Roberts, G.W.; Masters, C.L.; Dotti, C.G.; Unsicker, K.; Beyreuther, K. Distinct sites of intracellular production for Alzheimer's disease A beta40/42 amyloid peptides. *Nat. Med.* **1997.** *3*, 1016–1020.

30. Ghiso, J.; Frangione, B. Amyloidosis and Alzheimer's disease. *Adv. Drug Deliv. Rev.* **2002,** *54*, 1539–1551.

31. Hardy, J.; Selkoe, D.; The amyloid hypothesis of Alzheimer’s disease: progress and problems on the road to therapeutics. *Science.* **2002,** 297, 353 – 356.

32. Haass, C.; Selkoe, D.; Soluble protein oligomers in neurodegeneration: Lessons from Alzheimer’s amyloid β-peptide. *Nat. Rev. Mol. Cell. Biol.* **2007,** 8, 101 – 112.

33. Tanzi, E.; Bertram, L.; Twenty years of the Alzheimer’s disease amyloid hypothesis: a genetic perspective. *Cell.* **2005,** 120, 545 – 555.

34. Karran, E.; Merken, M.; De Strooper, B.; The amyloid cascade hypothesis for Alzheimer’s disease: an appraisal for the development of therapeutics. *Nat. Rev. Drug. Discov.* **2011,** 10, 698 – 712.

35. Glabe, G.; Common mechanisms of amyloid oligomer pathogenesis in degenerative disease. *Neurobiol. Aging.* **2006,** 27, 570 – 575.

36. Naslund, J. Correlation between elevated levels of amyloid β-peptide in the brain and cognitive decline. *JAMA.* **2000,** 283, 1571 – 1577.

37. Citron, M. Strategies for disease modification in Alzheimer's disease. *Nat. Rev. Neurosci.* **2004,** *5,* 677–685.

38. Hardy, J.; Allsop, D. Amyloid deposition as the central event in the aetiology of Alzheimer's disease. *Trends Pharm. Sci.* **1991,** *12,* 383-388

39. Zhou, S.; Zhou, H.; Walian, P. J.; Jap, B. K. Regulation of γ-secretase activity in Alzheimer's disease. *Biochemistry.* **2007,** *46,* 2553-2563.

40. Lashuel, H.A.; Hartley, D.M.; Balakhaneh, D.; Aggarwal, A.; Teichberg, S. Callaway, D.J. New class of inhibitors of amyloid-beta fibril formation. Implications for the mechanism of pathogenesis in Alzheimer's disease. *J. Biol. Chem.* **2002,** *277,* 42881–90.

41. Wolfe, M.; γ-secretase inhibition and modulation for Alzheimer's disease. *Curr. Alzheimer. Res.* **2008,** 5, 158 – 164.

42. He, G.; Luo, W.; Li, P.; Remmers, C.; Netzer, W.J.; Hendrick, J.; Bettayeb, K.; Flajolet, M.; Gorelick, F.; Wennogle, L.P.; Greengard, P. Gamma-secretase activating protein, a therapeutic target for Alzheimer's disease" *Nature.* **2010,** *467,* 95–98.

43. Cappai, R.; Barnham, KJ.; Delineating the mechanism of Alzheimer's disease A beta peptide neurotoxicity. *Neurochem. Res.* **2008,** 33, 562 – 532

44. Pimplikar, S.; Reassessing the amyloid cascade hypothesis of Alzheimer's disease. *Int. J. Biochem. Cell. Biol.* **2009,** 41: 1261– 1268.

45. Lesne, S.; A specific amyloid-β protein assembly in the brain impairs memory. *Nature.* **2006,** 440, 352–357.

46. Selkoe, D.; The molecular pathology of Alzheimer's disease. *Neuron.* **1991,** 6, 487–498.

47. Abramov, A. Y.; Canevari, L.; Duchen, M.; β-amyloid peptides induce mitochondrial dysfunction and oxidative stress in astrocytes and death of neurons through activation of NADPH oxidase. *J. Neurosci.* **2004,** *24,* 565-575.

48. Dinamarca, M. C.; Sagal, J. P.; Quintanilla, R. A.; Godoy, J. A.; Arrazola, M. S.; Inestrosa, N. C. Amyloid-β-acetylcholinestase complexes potentiate neurodegenerative changes induced by the Aβ peptide. Implications for the pathogenesis of Alzheimer's disease. *Mol. Neurodegener*. **2010,** *5,* 1-15.

49. Carvajal, F. J.; Inestrosa, N. C.; Interactions of AChE with Aβ aggregates in Alzheimer's brain: therapeutic relevance of IDN 5706. *Front. Mol. Neurosci.* **2011,** *4*, 1-10.

50. Alvarez, A.; Opazo, C.; Alarcon, R.; Garrido, J.; Inestrosa, N.C. Acetylcholinesterase promotes the aggregation of amyloid peptide fragments by forming a complex with the growing fibrils. *J. Mol. Biol.* **1997,** *272,* 348-361.

51. Shankar, G.; Amyloid-β protein dimers isolated directly from Alzheimer's brains impair synaptic plasticity and memory. *Nat. Med.* **2008,** 14, 837–842.

52. Inestrosa, N. C.; Dinamarca, M. C.; Alvarez, A. Amyloid cholinesterase interactions. Implications for Alzheimer's disease. *FEBS J.* **2008,** *275,* 625–632.

53. Bartolini, M.; Bertucci, C.; Cavrini, V.; Andrisano, V. β-Amyloid aggregation induced by human acetylcholinesterase: inhibition studies. *Biochem. Pharmacol.* **2003,** *65,* 407-416.

54. Barnham, K.; Bush, A.; Metals in Alzheimer's and Parkinson's disease. *Curr. Opin. Chem. Biol.* **2008,** 12, 222 – 228.

55. Faller, P.; Copper and zinc binding to amyloid-β: coordination, dynamics, aggregation, reactivity and meta-ion transfer. *Chem. Bio. Chem.* **2009,** 10, 2837 – 2845.

56. Chang W.; Downs D.; Huang X.; Da H.; Fung K.; Tang J.; Amyloid-beta reduction by memapsin 2 (beta-secretase) immunization. *FASEB. J*. **2007,** 21 3184 – 3196.
57. Mangialasche, F.; Solomon, A.; Winblad, B.; Mecocci, P.; Kivipelto, M.; Alzheimer's disease: clinical trials and drug development. *Lancet. Neurol.* **2010,** 9, 702 – 716.
58. Citron, M.; β-secretase inhibition for the treatment of Alzheimer's disease – promise and challenge. *Trends. Pharmacol. Sci.* **2004,** 25, 92 – 97.
59. Schor, N.; What the halted phase III γ-secretase inhibitor trial may (or may not) be telling us. *Ann. Neurol.* **2011,** 69, 237 – 239.
60. Tomita T.; Secretase inhibitors and modulators for Alzheimer's disease treatment. *Expert. Rev. Neurother.* **2009,** 9: 661 – 679.
61. Green R.; Schneider L.; Amato D.; Effect of tarenflurbil on cognitive decline and activities of daily living in patients with mild Alzheimer disease: a randomized controlled trial. *JAMA*. **2009,** 302, 2557 – 2564.
62. Amijee H.; Scopes D.; The quest for small molecules as amyloid inhibiting therapies for Alzheimer's disease. *J. Alzheimers. Dis.* **2009,** 17, 33 – 47.
63. DaSilva, K.; Shaw, J.; McLaurin, J.; Amyloid-β fibrillogenesis: structural insight and therapeutic intervention. *Exp. Neurol.* **2010,** 223, 311 – 321.
64. Aisen P.; Gauthier S.; Ferris S.; A phase III, placebo-controlled, double-blind, randomized trial of tramiprosate in the clinical management of patients with mild-to-moderate Alzheimer's disease (the Alphase study). 61st American Academy of Neurology annual meeting; Seattle, WA, USA; April 25–May 02, 2009. S32.003.
65. McElhaney J.; Effros R.; Immunosenescence: what does it mean to health outcomes in older adults? *Curr. Opin. Immunol.* **2009,** 21, 418 – 424.

66. Bard, F.; Peripherally administered antibodies against amyloid β-peptide enter the central nervous system and reduce pathology in a mouse model of Alzheimer disease. *Nat. Med.* **2000,** 6, 916 – 919.

67. Salloway S.; Sperling R.; Gilman S.; A phase 2 multiple ascending dose trial of bapineuzumab in mild to moderate Alzheimer disease. *Neurology*. **2009**, 73, 2061– 20 70.

68. Blasko, I.; Grubeck, B.; Role of the immune system in the pathogenesis, prevention and treatment of Alzheimer's disease. *Drug. Aging.* **2003,** 20, 101 – 113.

69. Andersen, J. K. Oxidative stress in neurodegeneration: cause or consequence? *Nat. Rev. Neurosci.* **2004,** *5,* S18-S25.

70. Gella, A.; Durany, N. Oxidative stress in Alzheimer's disease. *Cell Adh. Migr.* **2009,** *3,* 88-93.

71. Markesbery, W.; Oxidative stress hypothesis in Alzhiemer's disease. *Free. Radical. Bio. Med.* **1997,** 23, 134 – 147.

72. Butterfield, D. A.; Reed, T.; Sultana, R. Roles of 3-nitrotyrosine- and 4-hydroxynonenal-modified brain proteins in the progression and pathogenesis of Alzheimer's disease. *Free Radical Res.* **2011,** *45,* 59-72.

73. Feng Y,; Wang X. Antioxidant therapies for Alzheimer's disease. *Ox. Med. Cell. Longev.* **2012**, 1-17.

74. Mecocci, P.; Polidori, M. C. Antioxidant clinical trials in mild cognitive impairment and Alzheimer's disease. *Biochim. Biophys. Acta.* **2012,** *5*, 631-638.

75. Butterfield, A.; Amyloid β-peptide (1-42)-induced oxidative stress and neurotoxicity: implications for neurodegeneration in Alzheimer's disease brain. A review. *Free. Radical. Res.* **2002,** 36, 1307 – 1313.

76. Butterfield, A.; Lauerback, C.; Lipid peroxidation and protein oxidation in Alzheimer's disease brain: potential causes and consequences involving amyloid β-peptide-associated free radical oxidative stress. *Free. Radical. Bio. Med.* **2002,** 32, 1050 – 1060.

77. Adlard P.; Cherny R.; Finkelstein D.; Rapid restoration of cognition in Alzheimer's transgenic mice with 8-hydroxy quinoline analogs is associated with decreased interstitial Abeta. *Neuron.* **2008,** 59, 43 – 55.

78. Mark, R.; Lovell, M.; Markesbery, W.; Uchida, K.; Mattson, M.; A role for 4-hydroxynonenal, an aldehydic product of lipid peroxidation, in disruption of ion homeostasis and neuronal death induced by amyloid β-peptide. *J. Neuro. Chem.* **1997,** 68, 255 – 264.

79. Lovell, M.; Ehmann, W.; Butler, S.; Markesbury, W.; Elevated thiobarbituric acid-reactive substances and antioxidant enzyme activity in the brain in Alzheimer's disease. *Neurology.* **1995,** 45, 1594 – 1601.

80. Subbaro, K.; Richardson, J.; Ang, L.; Autopsy samples of Alzheimer's cortex show increased peroxidation in vitro. *J. Neurochem.* **1990,** 55, 342 – 345.

81. Nitsch, R.; Blusztjan, J.; Pittas, A.; Slack, B.; Growdon, J.; Wurtman, R.; Evidence for a membrane defect in Alzheimer's disease brain. *Proc. Natl. Acad. Sci. USA.* **1992,** 89, 1671 – 1675.

82. Lovell, M.; Ehmann, W.; Markesbury, W.; Elevated 4-hydroxyalkenals in ventricular fluid in Alzheimer's disease. *Neurobiol. Aging.* **1997,** 18, 457 – 461.

83. Bruce-Keller, A.; Li, Y.; Lovell, M.; Kraemer, P.; Gary, D.; Brown,R.; Markesbery, W.; Mattson, M.; 4-Hydroxynonenal, a product of lipid peroxidation, damages cholinergic

neurons and impairs visuospatial memory in rats. *J. Neuropathol. Exp. Neurol.* **1998,** 57, 257 – 267.

84. Butterfield, D.; Stadtman, E.; Protein oxidation processes in aging brain. *Adv. Cell. Aging. Gerontol.* **1997,** 2, 161 – 191.

85. Varadarajan, S.; Yatin, S.; Aksenova, M.; Butterfield, D.; Review: Alzheimer's amyloid β-peptide-associated free radical oxidative stress and neurotoxicity. *J. Struct. Biol.* **2000,** 130, 184 – 208.

86. Aksenov, M.; Aksenov, M.; Aksenova, M.; Butterfield, D.; Geddes, J.; Markesbery, W.; Protein oxidation in the brain in Alzheimer's disease. *Neuroscience.* **2001,** 103, 373 – 383.

87. Yatin, S.; Aksenov, M.; Butterfield, D.; The antioxidant vitamin E modulates amyloid β-peptide-induced creatine kinase inhibition and increased protein oxidation: implications for the free radical hypothesis of Alzheimer's disease. *Neurochem. Res.* **1999,** 24, 427 – 435.

88. Bruce-Keller, A.; Begley, J.; Fu, W.; Butterfield, D.; Bredesen, D.; Hutchins, J.; Hensley, K.; Mattson,M.; Bcl-2 protects isolated plasma and mitochondrial membranes against lipid peroxidation induced by hydrogen peroxide and amyloid beta-peptide. *J. Neurochem.* **1998,** 70, 31 – 39.

89. Mudher, A.; Lovestone, S.; Alzheimer's disease-do tauists and baptists finally shake hands? *Trends. Neurosci.* **2002,** 25, 22 – 26.

90. Wischik, C.; Staff, R.; Challenges in the conduct of disease-modifying trials in Alzheimer's disease: practical experience from a phase 2 trial of TAU-aggregation inhibitor therapy. *J. Nutr. Health. Aging.* **2009,** 13, 367 – 369.

91. Green, K.; Steffan J.; Martinez-Coria H.; Nicotinamide restores cognition in Alzheimer's disease transgenic mice via a mechanism involving sirtuin inhibition and selective reduction of Thr231-phosphotau. *J. Neurosci.* **2008**, 28, 11500 – 11510.

92. Cutler, N.; Sramek, J.; Review of the next generation of Alzheimer's disease therapeutics: challenges for drug development. *Prog. Neuro-psychoph.* **2001,** 25, 27 – 57.

93. Foley, P.; Gerlach, M.; Youdim, M.; Riederer, P.; MAO-B inhibitors: multiple roles in the therapy of neurodegerative disorders? *Parkinsonism. Relat. D.* **2000,** 6, 25 – 47.

94. Mohamed, T.; Rao, P.P.N. Alzheimer's disease: Emerging trends in small molecule therapies. *Curr. Med. Chem.* **2011,** 18, 4299-4320.

95. Tariot, P.; Farlow, M.; Grossberg, G.; Graham, S.; McDonald, S.; Gergi, I.; Memantine treatment in patients with moderate to severe Alzheimer's disease already receiving donepezil. *JAMA.* **2004,** 291, 317 – 324.

96. Osman, W.; (2013). *Design, synthesis and evaluation of tacrine-based derivatives: potential agents to treat Alzheimer's disease.* Unpublished master's thesis. University of Waterloo, School of Pharmacy. Kitchener, Canada.

97. Papp, L. V.; Lu, J.; Holmgren, A.; Khanna, K. K. From selenium to selenoproteins: Synthesis, identity, and their role in human health. *Antioxid. Redox Sign.* **2007,** *9,* 775-806.

98. Meyer, J.; Koro, C.; The effects of antipsychotic therapy on serum liquids: a comprehensive review. *Schizophr. Res.* **2004,** 70, 1 – 17.

99. Blin, O.; A comparative review of antipsychotics. *Can. J. Psychiatry.* **1999,** 44, 235 – 244.

100. Darvesh, S.; McDonald, R.; Penwell, A.; Conrad, S.; Darvesh, K.; Mataija, D.; Gomez, G.; Caines, A.; Walsh, R.; Martin, E.; Structure-activity relationships for inhibition of human cholinesterases by alkyl amide phenothiazine deratives. *Bioorgan. Med. Chem.* **2005,** 13, 211 – 222.

101. Smith, N.; Synthesis of phenothiazine derivatives for use as antioxidants. *J. Org. Chem.* **1950,** 15, 1125 – 1130.

102. Muller, P.; Buu-Hoi, N. P.; Rips, R. Preparation and some reactions of phenoxazine and phenoselenazine. *J. Org. Chem.* **1959,** *24*, 37-39.

103. Griffiths, J.; Gorman, S.; Bell, A.; Photosensitisers and their uses as anticarcinogenic, antibacterial and aniinfective agent in in vivo photodynamic therapy (PDT); 3,7-Bis-(N,N-dipentylamino)phenoselenazin-5-ylium iodide. **2007,** *US7407948 B2*, Washington, DC: US.

104. Nogueria, C. W.; Rocha, J. B. Toxicology and pharmacology of selenium: emphasis on synthetic organoselenium compounds. *Arch. Toxicol.* **2011,** *85*, 1313-1359.

105. Battin, E. E.; Brumaghim, J. L. Antioxidant activity of sulfur and selenium: A review of reactive oxygen species scavenging, glutathione peroxidise, and metal-binding antioxidant mechanisms. *Cell. Biochem. Biophys.* **2009,** *55*, 1-23.

106. Bellinger, F. P.; Bellinger, M. T.; Seale, L. A.; Takemoto, A. S.; Raman, A. V.; Miki, T.; Manning-Bog, A. B.; Berry, M. J.; White, L. R.; Ross, G. W. Glutathione peroxidise 4 is associated with neuromelanin in Substantia Nigra and dystrophic axons in putamen of Parkinson's brain. *Mol. Neurodegener.* **2011,** *6*, 1-10.

107. Yoo, M. H.; Gu, X. L.; Xu, X. M.; Kim, J. Y.; Carlson, B. A.; Patterson, A. D.; Cai, H. B.; Gladyshev, V. N.; Hatfield, D. L.; Delineating the role of glutathione peroxidise 4 in

protecting cells against lipid hydroperoxide damage and in Alzhimer's disease. *Antioxid. Redox. Sign.* **2010,** *12*, 819-827.

108. Cardoso, B. R.; Ong, T. P.; Jacob-Filho, W.; Jaluul, O.; Freitas, M. I.; Cozzolino, S. M. Nutritional status of selenium in Alzheimer's disease patients. *Brit. J. Nutr.* **2010,** *103*, 803-806.

109. Schewe, T. Molecular actions of ebselen—an anti-inflammatory antioxidant. *Gen. Pharmacol.* **1995,** *26*, 1153-1169.

110. Nakamura, Y.; Feng, Q.; Kumagai, T.; Torikai, K.; Ohigashi, H.; Osawa, T.; Noguchi, N.; Niki, E.; Uchida, K. Ebselen, a glutathione peroxidise mimetic seleno-organic compound, as a multifunctional antioxidant: Implication for inflammation-associated carcinogenesis. *J. Biol.Chem.* **2002,** *277*, 2687-2694.

111. Tiano, L.; Fedeli, D.; Santoni, G.; Davies, I.; Wakabayashi, T.; Falcioni, G. Ebselen prevents mitochondrial ageing due to oxidative stress: in vitro study of fish erythrocytes. *Mitochondrion.* **2003,** *2*, 428-436.

112. Mouithys-Mickalad, A.; Mareque-Faez, J.; Chistiaens, L.; Kohnen, S.; Deby, C.; Hoebeke, M.; Lamy M.; Deby-Dupont, G. *In vitro* evaluation of glutathione peroxidase (GPx)-like activity and antioxidant properties of some ebselen analogues. *Redox. Rep.* **2004,** *9*, 81-87.

113. Sakurai, T.; Kanayama, M.; Shibata, T.; Itoh, K.; Kobayashi, A.; Yamamoto, M.; Uchida, K. Ebselen, a seleno-organic antioxidant, as an electrophile. *Chem. Res. Toxicol.* **2006,** *19*, 1196-1204.

114. Nogueira, C. W.; Rocha, J. B. Toxicology and pharmacology of selenium: emphasis on synthetic organoselenium compounds. *Arch. Toxicol.* **2011,** *85*, 1313-1359.

115. Belei, D.; Dumea, C.; Samson, A.; Farce, A.; Dubois, J.; Bicu, E.; Ghinet, A. New farnesyltransferase inhibitors in the phenothiazine series. *Bioorg. Med. Chem. Lett.* **2012,** *22,* 4517-4522.

116. Kaboudin, B.; Abedi, Y.; Yokomatsu, T.; Cu^{II}-β-cyclodextrin complex as a nanocatalyst for the homo- and cross coupling of arylboronic acids under ligand- and base- free conditions in air: chemoselective cross-coupling of arylboronic acids in water. *Eur. J. Org. Chem.* **2011,** 6656 – 6662.

117. Wang, X.; Jang, H. All-purpose copper catalyst for coupling of ammonium salts and 1° and 2° amines with boronic acid. *Bull. Korean Chem. Soc.* **2012,** *33,* 1785-1787.

118. Antilla, J.; Buchwald, S.; Copper-catalyzed coupling of arylboronic acids and amines. *Org. Lett.* **2001,** 3, 2077 – 2079.

119. Krafft, M.; Cran, J.; A convenient protocol for the α-iodination of α,β-unsaturated carbonyl compounds with I_2 in an aqueous medium. *Syn. Lett.* **2005,** 8, 1264 – 1266.

120. Barros, M.; Dey, S.; Maycock, C.; Metal-free synthesis of secondary arylamines: an aliphatic-to-aromatic transformation. *Eur. J. Org. Chem.* **2013,** 742 – 747.

121. Griffiths, J.; Gorman, S.; Bell, A.; Photosensitisers and their uses. **2007,** *US 2007/0197494 Al,* Washington, DC: US

122. Duchesne, J.; Process for the preparation of diaryl sulphides and diaryl selenides. **1991,** *5,026,846,* Washington, DC: US

123. Ellman, G. L.; Courtney, K. D.; Andres, V.; Featherstone, R. M. A new and rapid colorimetric determination of acetylcholinesterase activity, *Biochem. Pharmacol.* **1961,** *7,* 88-95.

124. Hudson, S. A.; Ecroyd, H.; Kee, T. W.; Carver, J. A. The thioflavin T fluorescence assay for amyloid fibril detection can be biased by the presence of exogenous compounds. *FEBS J*. **2009,** *276,* 5960-5972.

125. Szabo, M. R.; Iditoiu, C.; Chambre, D.; Lupea, A. X. Improved DPPH determination for antioxidant activity spectrophotometric assay. *Chem. Pap.* **2007,** *61,* 214-216.

126. Mosmann T. Rapid colorimetric assay for cellular growth and survival: application to proliferation and cytotoxicity assays. *J. Immunol. Methods.* **1983**, 65, 55-63.

127. Diller, D.; Merz, M.; High throughput docking for library design and library prioritization. *Proteins.* **2001,** 43, 113 – 124.

128. Wu, G.; Robertson, D.; Brooks, C.; Vieth, M.; Detailed analysis of grid-based molecular docking: a case study of CDOCKER – a CHARMm-based MD docking algorithm. *J. Comp. Chem.* **2003,** 23, 1549.